The USGS 2023 Conterminous U.S. Time-Independent Earthquake Rupture Forecast

Edward H. Field*[1], Kevin R. Milner[2], Alexandra E. Hatem[1], Peter M. Powers[1], Fred F. Pollitz[3], Andrea L. Llenos[1], Yuehua Zeng[1], Kaj M. Johnson[4], Bruce E. Shaw[5], Devin McPhillips[6], Jessica Thompson Jobe[1], Allison M. Shumway[1], Andrew J. Michael[3], Zheng-Kang Shen[7], Eileen L. Evans[8], Elizabeth H. Hearn[9], Charles S. Mueller[1], Arthur D. Frankel[10], Mark D. Petersen[1], Christopher DuRoss[1], Richard W. Briggs[1], Morgan T. Page[6], Justin L. Rubinstein[3], and Julie A. Herrick[1]

ABSTRACT

We present the 2023 U.S. Geological Survey time-independent earthquake rupture forecast for the conterminous United States, which gives authoritative estimates of the magnitude, location, and time-averaged frequency of potentially damaging earthquakes throughout the region. In addition to updating virtually all model components, a major focus has been to provide a better representation of epistemic uncertainties. For example, we have improved the representation of multifault ruptures, both in terms of allowing more and less fault connectivity than in the previous models, and in sweeping over a broader range of viable models. An unprecedented level of diagnostic information has been provided for assessing the model, and the development was overseen by a 19-member participatory review panel. Although we believe the new model embodies significant improvements and represents the best available science, we also discuss potential model limitations, including the applicability of logic tree branch weights with respect different types of hazard and risk metrics. Future improvements are also discussed, with deformation model enhancements being particularly worthy of pursuit, as well as better representation of sampling errors in the gridded seismicity components. We also plan to add time-dependent components, and assess implications with a wider range of hazard and risk metrics.

KEY POINTS

- We provide a new earthquake rupture forecast for the conterminous United States.
- Innovations include better representations of multifault ruptures and epistemic uncertainties.
- This model will be used in building codes and other risk mitigation efforts.

MANUSCRIPT ORGANIZATION

Because of manuscript length and model complexity, we begin with an outline of this report to help readers navigate the various sections:

1. U.S. Geological Survey, Denver Federal Center, Denver, Colorado, U.S.A., https://orcid.org/0000-0001-8172-7882 (EHF); https://orcid.org/0000-0001-7584-2235 (AEH); https://orcid.org/0000-0003-2124-6184 (PMP); https://orcid.org/0000-0002-4088-6737 (ALL); https://orcid.org/0000-0003-1161-1264 (YZ); https://orcid.org/0000-0001-5574-4523 (JTJ); https://orcid.org/0000-0003-1142-7141 (AMS); https://orcid.org/0000-0002-1868-9710 (CSM); https://orcid.org/0000-0001-8542-3990 (MDP); https://orcid.org/0000-0002-6963-7451 (CDR); https://orcid.org/0000-0001-8108-0046 (RWB); https://orcid.org/0000-0003-0682-760X (JAH); 2. University of Southern California, Southern California Earthquake Center, Los Angeles, California, U.S.A., https://orcid.org/0000-0002-9118-6378 (KRM); 3. Earthquake Science Center, Moffett Field, California, U.S.A., https://orcid.org/0000-0002-4060-2706 (FFP); https://orcid.org/0000-0002-2403-5019 (AJM); https://orcid.org/0000-0003-1274-6785 (JLR); 4. Department of Geological Sciences, Indiana University, Indiana, U.S.A., https://orcid.org/0000-0003-1511-5241 (KMJ); 5. Lamont–Doherty Earth Observatory, Columbia University, Palisades, New York, U.S.A., https://orcid.org/0000-0002-6431-9745 (BES); 6. U.S. Geological Survey, Pasadena, California, U.S.A., https://orcid.org/0000-0003-1987-9249 (DMP); https://orcid.org/0000-0001-9321-2990 (MTP); 7. Department of Earth, Planetary, and Space Sciences/UCLA, Los Angeles, California, U.S.A., https://orcid.org/0000-0002-4965-174X (Z-KS); 8. California State University, Northridge, Northridge, California, U.S.A., https://orcid.org/0000-0002-7290-5269 (ELE); 9. Capstone Geophysics, Portola Valley, California, U.S.A., https://orcid.org/0000-0002-4559-7918 (EHH); 10. U.S. Geological Survey, Seattle, Washington, U.S.A., https://orcid.org/0000-0001-9119-6106 (ADF)

*Corresponding author: field@usgs.gov

Cite this article as Field, E. H., K. R. Milner, A. E. Hatem, P. M. Powers, F. F. Pollitz, A. L. Llenos, Y. Zeng, K. M. Johnson, B. E. Shaw, D. McPhillips, *et al.* (2023). The USGS 2023 Conterminous U.S. Time-Independent Earthquake Rupture Forecast, *Bull. Seismol. Soc. Am.* **114**, 523–571, doi: 10.1785/0120230120

INTRODUCTION

This report documents the U.S. Geological Survey (USGS) 2023 time-independent earthquake rupture forecast (ERF) for the conterminous United States (CONUS), herein abbreviated as "ERF-CONUS-2023-TI." An ERF gives the probability of all possible damaging earthquakes in a region and over a specified timespan (or a suite of synthetic catalogs for such events), and by "all" we mean at some level of discretization that is deemed adequate for hazard and risk quantification. An ERF is one of the two main model components used in seismic hazard assessment, with the other being a ground motion model (GMM) providing an estimate of the shaking produced by each rupture. Regarding nomenclature, ERFs are also referred to as a "seismic source model" or "seismic source characterization," especially in time-independent analyses. We avoid these names due to ambiguity with studies of individual observed earthquakes (e.g., the "source model" for the Northridge earthquake). Furthermore, "ERF" better captures the forecasting nature of the model, especially for the time-dependent extensions we plan to deploy later. Including "rupture" in the name removes the suggestion that we are talking about ground motion (earthquake is synonymous with earthshake). In short, "ERF" is more precise and less ambiguous, especially for nonexperts.

The work presented here represents an update of the models utilized in the 2018 USGS National Seismic Hazard Model (NSHM; Petersen *et al.*, 2020), which largely utilized unmodified ERF components from the 2014 NSHM (Petersen *et al.*, 2015); we refer to these previous collective efforts as "NSHM14/18" hereafter. Although the general goals and strategies articulated here are applicable to all geographic areas under the USGS earthquake hazard purview, specific 2023 ERF details for Hawaii are given in Petersen *et al.* (2021), and those for Alaska are being developed under the leadership of Peter Powers (written comm., 2023, referred to hereafter as PowersAlaska2023).

Broader goals

The following goals are currently influencing the development of USGS ERFs:

1. **A more comprehensive representation of epistemic uncertainties**: A forecast should now be deemed highly questionable without epistemic uncertainty estimates. The fact that such uncertainties still grow with each new model indicates that they have not yet been fully quantified. We want to get to where these uncertainties are reduced by new scientific studies.
2. **More uniformity in model assumptions and methodologies across regions**.
3. **More operationalization of model component development**, which will improve reproducibility, testability, modifiability (e.g., consultants performing site-specific analyses), and the speed at which we roll out future improvements. "Operationalization" here means a more "push button" environment in which routine processing is moved from

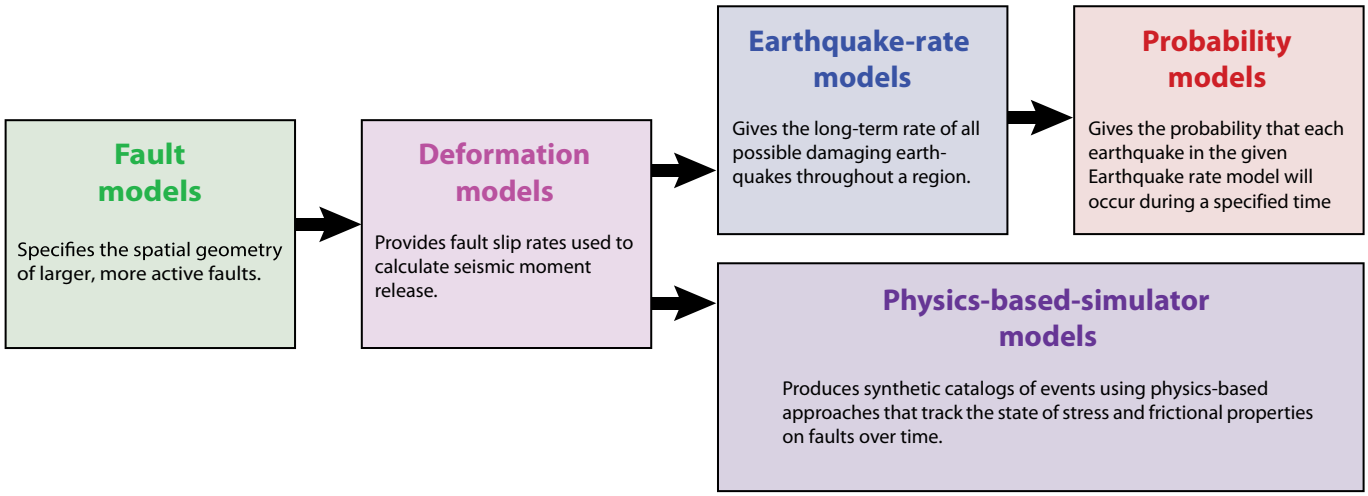

Figure 1. The main model components in our earthquake rupture forecast framework. The color version of this figure is available only in the electronic edition.

scientists to computers (freeing the former to focus on scientific improvements).

4. **Impose simplicity wherever we can**, even if it means abandoning long-cherished assumptions or techniques or logic tree branches that have been maintained for political expediency. The main motives here are understandability with respect to reviewers and practitioners, and getting the next generation of contributors up to speed (plus the psychological fact that people tend to dislike what they cannot understand). The rationalization for simplicity is that a less "realistic" model can actually be more useful (e.g., less computationally demanding); we want to find the right balance, which is a challenge, because this will vary among applications.
5. **Deregionalize model component developments**, that is, have the same group of scientists develop like types of components for all regions simultaneously rather than having separate "working groups" doing things independently. This is more efficient and contributes to uniformity.
6. **Deploy models that are extensible with respect to time dependencies**, including elastic rebound, spatiotemporal clustering, swarms, and induced seismicity.
7. **Provide more complete documentation** (i.e., minimize the need to read previous publications for implementation details).

All the above goals are aimed at increasing the rate at which we can roll out improved and more useful models, all the while doing more with less. These goals are admittedly aspirational, or perhaps even utopian, but we nonetheless believe they are both worthy of pursuit, and that we have at least incrementally manifested them here. Where we have come up short often reflects time constraints, which we intend to address as we evolve into maintaining a living "research model" or "forecasting enterprise," from which versions can be time stamped for specific official uses (e.g., by building code committees or for pricing insurance products).

Scientifically, or in terms of improving model realism, the main improvement here is representing possible multifault ruptures on explicitly modeled faults. This is not only with respect to allowing more such ruptures throughout the western United States (WUS), but alternatively with respect to imposing more segmentation than was applied previously in the Uniform California Earthquake Rupture Forecast, Version 3 (UCERF3; Field *et al.*, 2014); this improvement reflects the lively scientific debate over the prevalence of multifault ruptures (Schwartz, 2018; Page, 2021).

Model elements

Given the system-level nature of ERF development, a modularized construction is critical to keep things manageable and to enable different groups of scientists to focus within their respective areas of expertise. The top-level model components utilized here include (1) fault model(s), (2) deformation model(s), (3) earthquake rate model(s); and (4) probability model(s). These components are depicted and defined further in Figure 1, which also shows how multicycle physics-based simulators can be substituted for the earthquake rate and probability components. The ERFs presented here are essentially equivalent to earthquake rate models due to their time independence (Poisson probabilities, with some possible exceptions as noted subsequently). Adding elastic rebound and spatiotemporal clustering time dependencies are planned for the future work.

The earthquake rate models developed here are composed of one or more of the following types of earthquake sources:

1. fault system solution,
2. classic fault source,
3. fault zone source, or
4. gridded seismicity.

A detailed definition of each of these is given subsequently (just before describing the specific implementations for 2023),

TABLE 1
List of Model Components and Associated Publications

Component	Authorship
Earthquake geology	
WUS geologic constraints	Hatem, Collett, *et al.* (2022)
CEUS geologic constraints	Thompson Jobe, *et al.* (2022)
CA paleorecurrence intervals	McPhillips (2022)
Tectonic geodesy	
GPS data compilation	Zeng (2022a)
Ghost transient corrections	Hearn (2022)
Geodetic creep model	Johnson *et al.* (2022)
Deformation models overview	Pollitz *et al.* (2022)
WUS geologic deformation model	Hatem, Reitman, *et al.* (2022)
WUS Zeng deformation model	Zeng (2022b)
WUS Shen–Bird deformation model	Shen and Bird (2022)
WUS Pollitz deformation model	Pollitz (2022)
WUS Evans deformation model	Evans (2022)
Formal review of WUS deformation models	Johnson *et al.* (2023)
Statistical seismology	
Catalog development	Shumway and Mueller*
Regional M ≥ 5 rates and *b*-values	Michael2023†
Declustering and smoothing	Llenos (2023)†
Earthquake physics	
Scaling relationships	Shaw (2023)
Rupture plausibility filter	Milner *et al.* (2022)
ERF model construction	
Hazard implications of declustering	Field *et al.* (2021)
New inversion methodology	Milner and Field (2023)
Geological evaluation of fault-system solutions	Hatem (2023)†
CEUS fault source models	Shumway (2023)†
Cascadia subduction model	Powers Cascadia (2023)†
Overview of CONUS ERFs	This paper
Formal review of CONUS ERFs	Jordan *et al.* (2023)

CEUS, Central and Eastern United States; CONUS, conterminous United States; ERF, earthquake rupture forecast; GPS, Global Positioning System; and WUS, Western United States.
*Available as a part of the NSHM 2023 data release (Petersen *et al.*, 2023b).
†Written communication as described in the main text here.

but we emphasize here that even the seemingly most complex one (the fault system solution) is conceptually quite simple and generalized to include everything from classic single-fault models (Field, Milner, and Page, 2020) to representing results from multicycle physics-based simulators (e.g., Milner *et al.*, 2021).

These four earthquake source types, as well as the main components depicted in Figure 1, are influenced by several subcomponents and/or analyses. A complete list of these for our 2023 CONUS ERF is given in Table 1, each of which represents a separate publication. These components are categorized by disciplinary group, again reflecting the system-level nature of the problem. We reference each of these components in the detailed explanations subsequently.

Table 1 also lists activities related to ERF construction, with the greatest effort involving the inversion-based fault system solutions (with respect to methodology development, compute time, and analysis of results). Other efforts involve construction and/or updating other source models, including that for the Cascadia subduction zone, and deciding how to handle the influence of creep, aftershocks, and avoiding double counting of earthquakes when sources are combined. The vast majority of ERF components have been revamped for this model, and all were given due consideration.

Epistemic uncertainties

Again, a primary goal is a more thorough and uniform representation of epistemic uncertainties, and to this end we use the standard practice of utilizing logic trees (Fig. 2). A persistent challenge is how to handle correlation, or lack thereof, between branches. When uncertainties are both numerous and uncorrelated, we will quickly run into the computational impossibility of systematically traversing all possible branches. As an example, our 2018 model has three branches for the dip of faults in the WUS (outside California). The simplest approach is to assume perfect correlation across the region (all faults have the same dip deviation on a given branch), leading to three branches. If the dips are uncorrelated, and say we have 100 faults, we end up with 1 million branches for this uncertainty alone. In this case we could switch to Monte Carlo sampling of branches. However, dips are likely somewhat correlated for nearby faults (e.g., adjacent sections of a given fault) but uncorrelated over greater distances. In this case, we would need to determine the correlation structure and Monte Carlo sample accordingly, which is not currently feasible.

We will see that this conundrum potentially applies to multiple uncertainties, including the newly added fault section *b*-value for large earthquakes. Fortunately, this is less of a concern for single site hazard curves (which is what comprises the USGS hazard maps); that is, hazard at a single site is generally dominated by nearby faults, and correlation among nearby faults seems more plausible. The bigger question is how assuming spatial correlation affects spatially distributed hazard and risk metrics (e.g., statewide portfolio risk analyses)—a concern that was previously articulated in the context of adding epistemic uncertainties to GMMs (Field, Milner, and Porter, 2020). At the very least, one might consider modifying the weights assigned to outlier branches in spatially distributed analyses, because perfect correlation is less likely, otherwise one runs the risk of exaggerating the width of inferred epistemic uncertainties.

Review process and consensus building

It has become a practical impossibility for any one individual to fully understand all aspects of a state-of-the-art ERF. This raises a significant risk that an explicit or implicit assumption in one ERF component might be inconsistent with that made in another, which is why a broad, thorough review is critical. Table 1 represents the discrete elements that have been

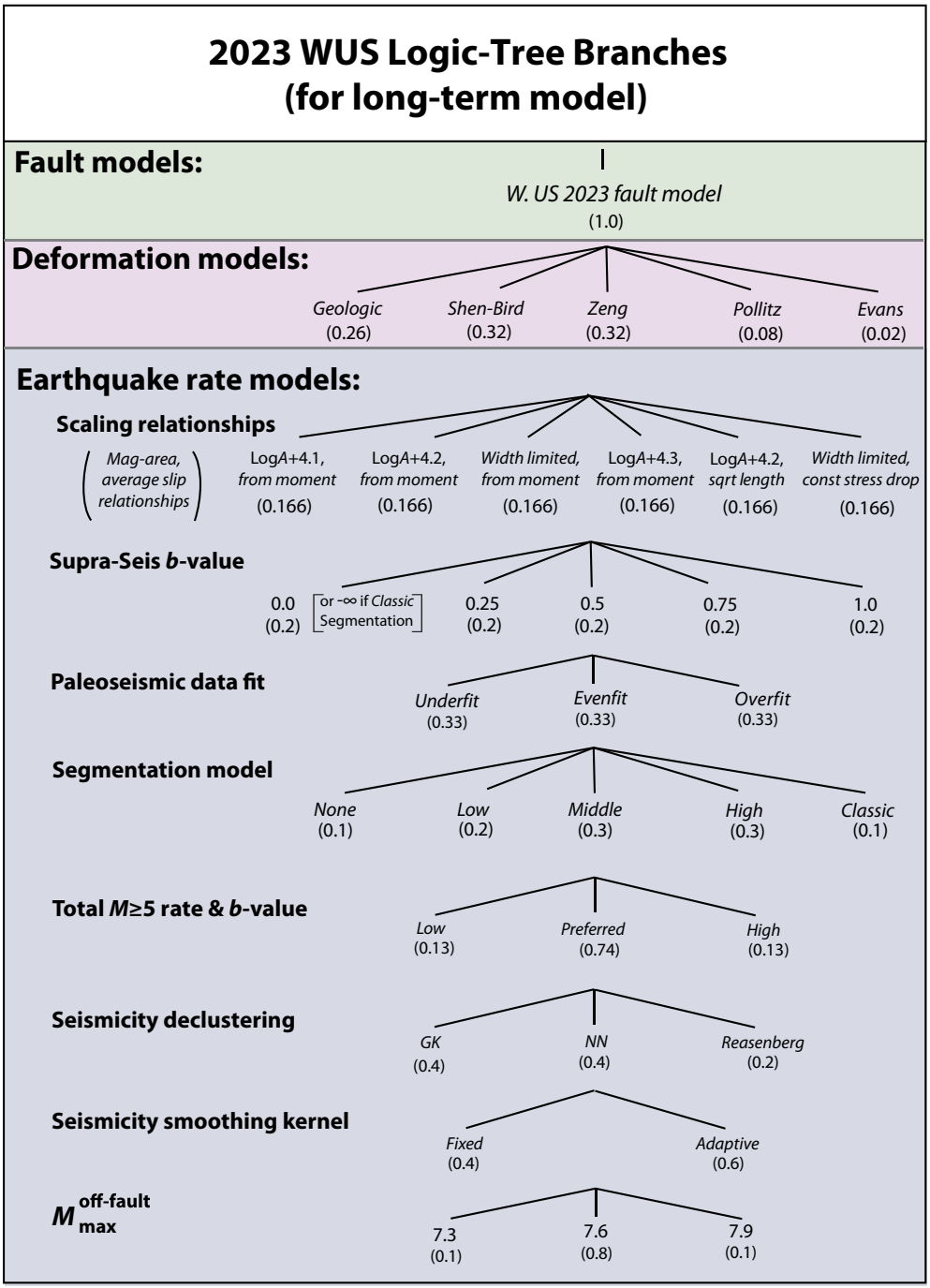

Figure 2. Logic tree branches for the western United States (WUS) branch weights are listed in parentheses. The color version of this figure is available only in the electronic edition.

reviewed, each of which has also been presented and discussed at one or more meetings or workshops (most of which were virtual). In addition, the overall model and development process was overseen by a 19-member participatory review panel, chaired by Thomas Jordan, and they provided a comprehensive report including recommendations for future work (Jordan *et al.*, 2023). But the main charge to this group was to determine whether the new model represents "best-available science," the definition of which they both reviewed and refreshed as representing "relevance, inclusiveness, verification, validation, transparency, timeliness, and peer review" (Jordan *et al.*, 2023). This effort also involved eight different open-participation briefings with more than 50 attendees at each (a link to video recordings is provided in Data and Resources), each of which was also followed by a closed executive session of the review panel.

Model results were also scrutinized by an ad hoc group of USGS geologists, who met virtually several times to examine earthquake connectivity, size, and rate implications on individual faults; this effort was led by Alexandra Hatem (USGS, written comm., 2023, referred to hereafter as Hatem2023), and note that all such documents mentioned in this article were available to, and considered by, our participatory review panel. This level of engagement, which was also made possible by an extensive set of web-based reports, is unique with respect to NSHM model developments. This led to several model improvements as well as future recommendations.

Subregions

For purposes of model component development, analyses, and comparison with the previous models, the greater U.S. region is subdivided into the following subregions (depicted in Fig. 3):

- WUS collection,
- Central and Eastern United States (CEUS) collection,
- CEUS,
- UCERF (Greater California),
- Pacific Northwest, and
- Intermountain West.

The first two "Collection" regions are for seismicity data analyses, and the others are for model analyses. The latter three

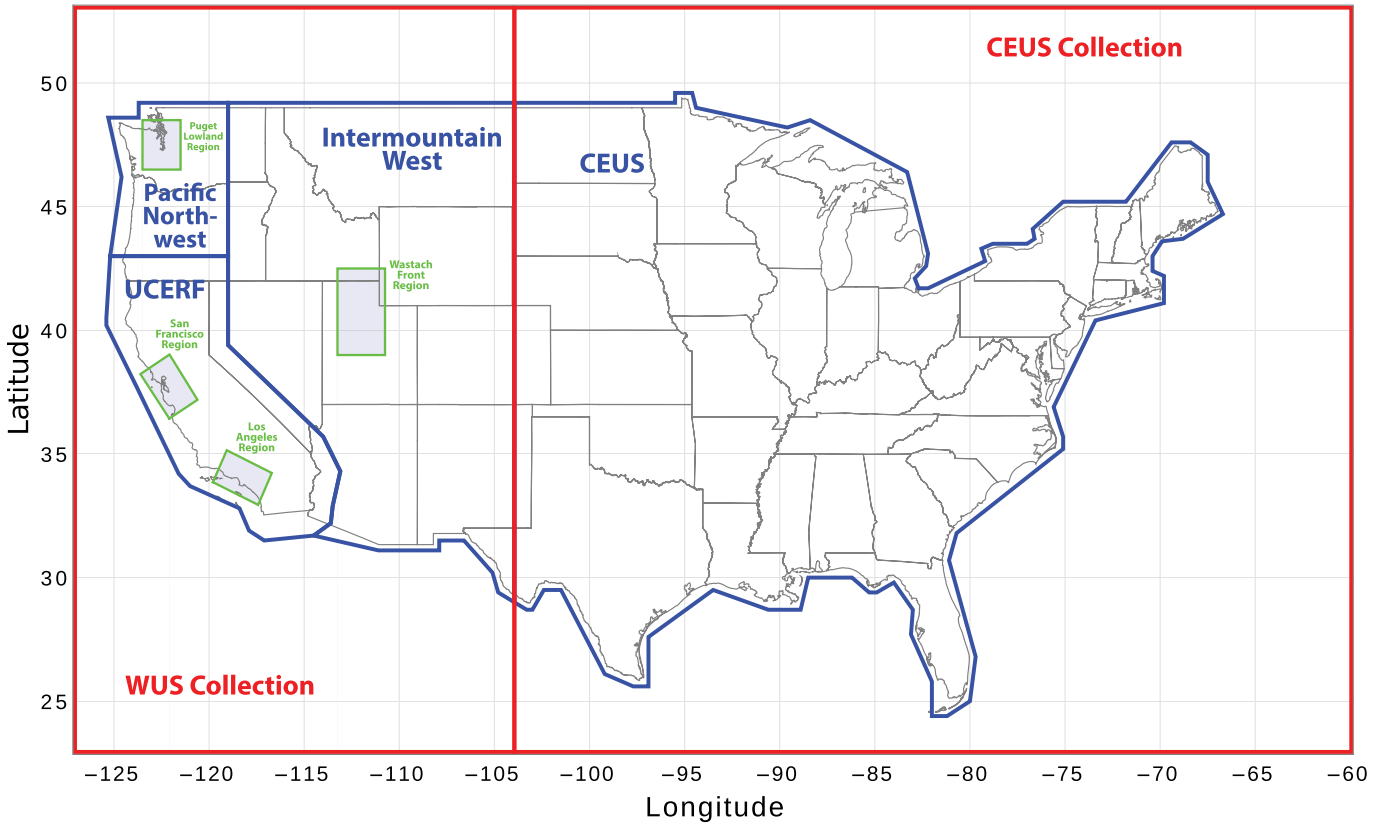

Figure 3. The various geographic regions utilized in this study as labeled. CEUS, Central and Eastern United States; UCERF, Uniform California Earthquake Rupture Forecast; and WUS, western United States. The color version of this figure is available only in the electronic edition.

regions are referred to collectively as WUS, and note that the Intermountain West–CEUS boundary utilized here differs from that applied for GMM selection (Petersen *et al.*, 2023a). Earthquakes deeper than 35 km in the Pacific Northwest and UCERF subregions are treated separately as a "Deep" region. The deregionalization of model component development raises the question of whether the California portion of the model should be called "UCERF4"; however, we do not adopt this acronym here.

Aftershocks

Following UCERF3, aftershocks are now included in the 2023 earthquake rate models, although final ERFs could be "declustered" for hazard computations if so desired, as was done for UCERF3 in NSHM14/18. Although the declustering algorithm used previously (Gardner and Knopoff, 1974) does not seem to influence typical hazard metrics (because it predominantly only removes smaller events), more scientifically defensible declustering algorithms (e.g., based on the ETAS model; Ogata, 1988, 1998) now remove about half of all events, both large and small, which would not be appropriate for seismic hazard assessment. There is now a substantial body of literature asserting that we are better off keeping aftershocks and assuming a Poisson process for 2% or 10% in 50 yr hazard than declustering with antiquated or biasing methodologies (Marzocchi and Taroni, 2014; Field *et al.*, 2021; Wang *et al.*, 2021; Michael and Llenos, 2022). However, at higher probabilities of exceedance (which may be used for applications such as operating standards) this approach may not be a good approximation. For this reason, there is also agreement that the longer-term goal should be to incorporate time dependencies correctly. In the meantime, and given the varying consequences of different viable declustering algorithms, the question of how to handle aftershocks should be addressed in the context of specific uses, so for now we are keeping aftershocks to allow the maximum flexibility (although note that declustering is still required with respect to inferring the long term spatial distribution of seismicity, as discussed in the Gridded seismicity sources section).

FAULT MODELS (AND GEOLOGIC CONSTRAINTS)

A fault model gives the 3D geometry of explicitly modeled faults. More specifically, a fault model is simply a list of fault sections, for which the latter are defined by a fault trace, dip, upper and lower seismogenic depth, and a geologically inferred rake. Fault sections vary widely in length, and some can be quite long if associated attributes do not vary significantly along strike (e.g., Maacama and Bartlett Springs are ~170 km long). Where faulting is dispersed, meaning that a clear dominant surface is lacking, a fault zone (geographic polygon) is defined instead, although a "proxy" fault surface may also be provided (and we have discontinued the UCERF3 practice of assigning a

polygon to all faults). This section describes the new fault models as well as other geologic constraints that are currently available and utilized.

WUS

A new WUS fault model was recently compiled and published by Hatem, Collett, *et al.* (2022), which is shown in Figure 4a. About 350 new faults have been added (mostly outside California as can be seen as orange lines in the figure), which were previously excluded because they lack an explicit geologic slip-rate constraint. UCERF3 had two fault models (alternative logic tree branches), but we reduced this to one "preferred" model here, because the differences were consistently nonconsequential among various hazard and risk metrics (e.g., figs. 12, 16, and 17 of Field *et al.*, 2015, fig. 4 of Porter *et al.*, 2017, and fig. 6 of Field, Milner, and Porter, 2020). There are 1016 fault sections in this updated fault model.

Hatem, Collett, *et al.* (2022) also provide an updated compilation of geologic slip-rate estimates at points on faults as well as a default-range estimate for faults that lack explicit studies (0 to 0.2, 0.2 to 1.0, and 1 to 5 mm/yr); the locations of all these are shown in Figure 4b. These slip rates are used to constrain the deformation models described in the next section.

The paleoseismic event-rate estimates for California faults have been updated and revised by McPhillips (2022), including the addition of seven new sites. An innovation of this work is consideration of whether the event history has been correctly interpreted (previously assumed), leading to recurrence intervals that are 16% longer, on average, compared with the UCERF3 estimates (Biasi, 2013), plus the confidence bounds are wider. This lengthening of recurrence intervals corrects for possible over interpretations (inferring too many events) in the previous studies. UCERF3 also utilized average slip-per-event data compiled by Madden *et al.* (2013), which was originally included here in the exact same way (converted to proxy event rates by dividing slip rate by this average slip). However, a reexamination of the Madden *et al.* (2013) methodology and results found that these constraints appear to be both biased and assigned unrealistically low uncertainty bounds, making their relatively strong influence highly questionable. We therefore removed these average-slip constraints from consideration until such questions can be resolved. The probability of missed events, an important part of the inversion fault system solutions described subsequently, remains the same as applied in UCERF3.

For the Wasatch fault, we apply the 17 paleoseismic event rate constraints compiled by Valentini *et al.* (2020), based on numerous studies referenced therein, and we apply the probability of missed events model used in that study as well (which differs from those applied in California). We also utilize the segmentation boundaries defined by the Working Group on Utah Earthquake Probabilities (Wong *et al.*, 2016), which are shown in Figure 5.

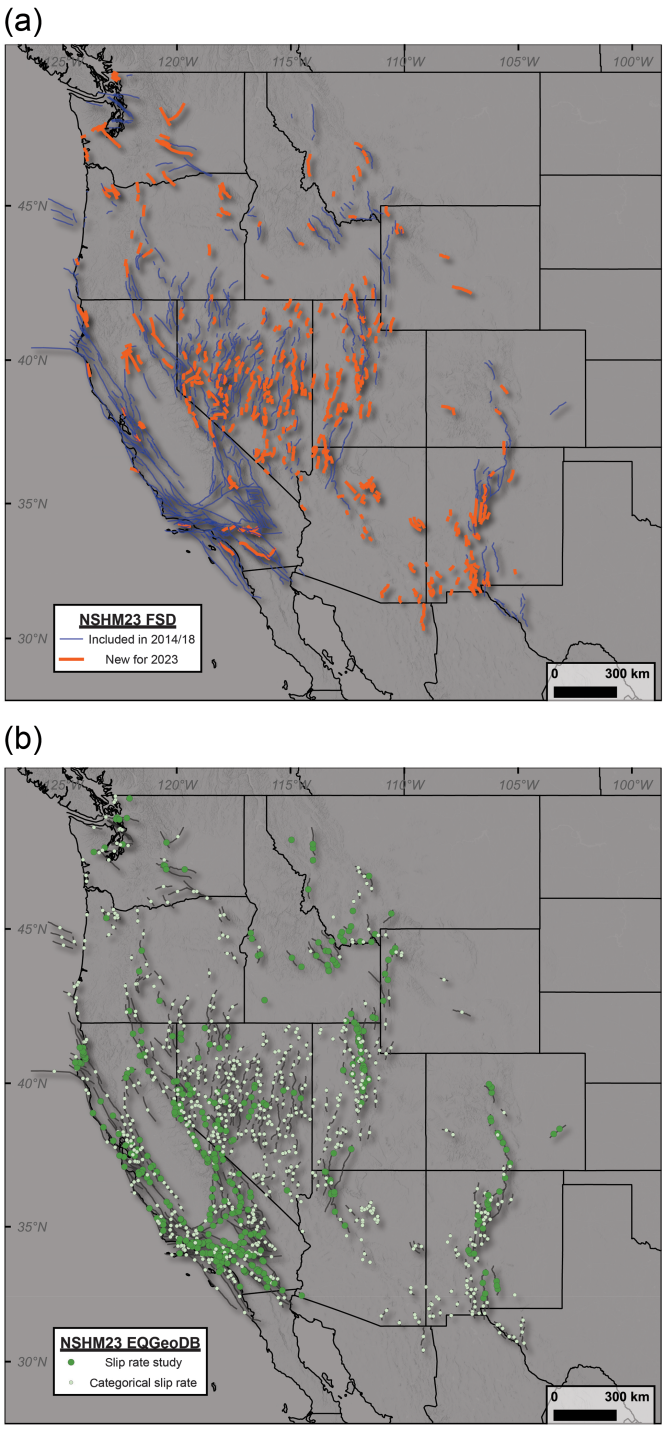

Figure 4. (a) WUS fault model with orange lines indicate newly added faults. (b) Geologic slip-rate constraints, for which green circles are locations with geologic studies and lighter circles are where a generic categorical range of values is assigned (based on the U.S. Geological Survey [USGS] Quaternary Fault and Fold Database [QFFD]). Refer to Hatem, Collett, *et al.* (2022) for details. The color version of this figure is available only in the electronic edition.

CEUS

Updates to the CEUS fault models and associated geologic constraints are provided by Thompson Jobe *et al.* (2022), the results of which are shown in Figure 6. The most consequential

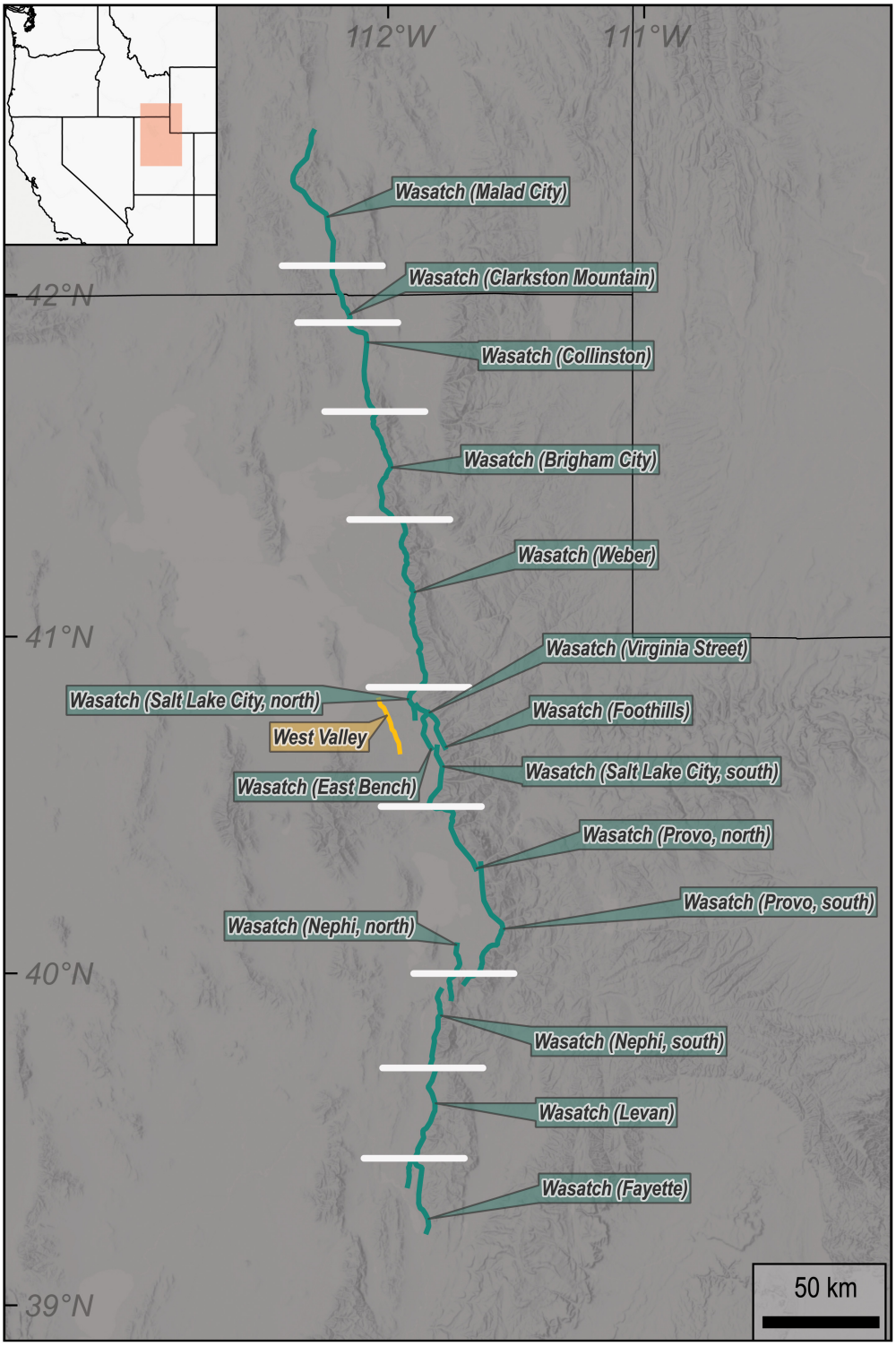

Figure 5. Wasatch fault segment boundaries (white horizontal bars) based on Wong *et al.* (2016). West Valley fault in yellow; Wasatch fault sections (as denoted in fault sections database) in green. Inset shows this region location in relation to WUS states. The color version of this figure is available only in the electronic edition.

changes are the addition of two source zones (Central Virginia and Saline River), plus three other sources that have both an explicit fault and a polygon zone representation (Joyner Ridge, Crowley's Ridge [south] and Crowley's Ridge [west]). Five fault zones were converted to explicit faults (Commerce, Eastern Margin [north], Eastern Margin [south], Crittenden County, and Meeman-Shelby, the latter of which was previously called River Picks). The Meers fault trace was extended to the west, minor adjustments were made to the geometries of four faults (Axial, Bootheel, New Madrid West, and Reelfoot), no adjustments were made to two faults (Charleston Uplift, New Madrid North), and no adjustments were made to four fault zones (Marianna, Wabash Valley, Charlevoix, and Charleston). In total, we have gone from 16 CEUS fault sources in NSHM14/18 to 21 here. Thompson Jobe *et al.* (2022) also summarize the slip rate and/or paleo event-rate constraints on each fault source. How each of these sources is modeled is discussed in the Earthquake rate models section.

DEFORMATION MODELS

Model descriptions

Deformation models provide slip-rate estimates for the explicitly modeled faults, and some also provide "off fault" deformation as well. Two new and three revised deformation models have been developed for the WUS subregion, each of which is published in a special issue of *Seismological Research Letters* with an overview paper by Pollitz *et al.* (2022). These models, which are listed and summarized in Table 2, were also formally examined by a semi-independent review team (Johnson *et al.*, 2023).

All deformation models utilize the Hatem, Collett, *et al.* (2022) fault model and geologic slip-rate constraints described earlier (including the ~350 new faults that were assigned broad, categorical slip rates due to their lacking explicit constraints), plus the substantially enhanced

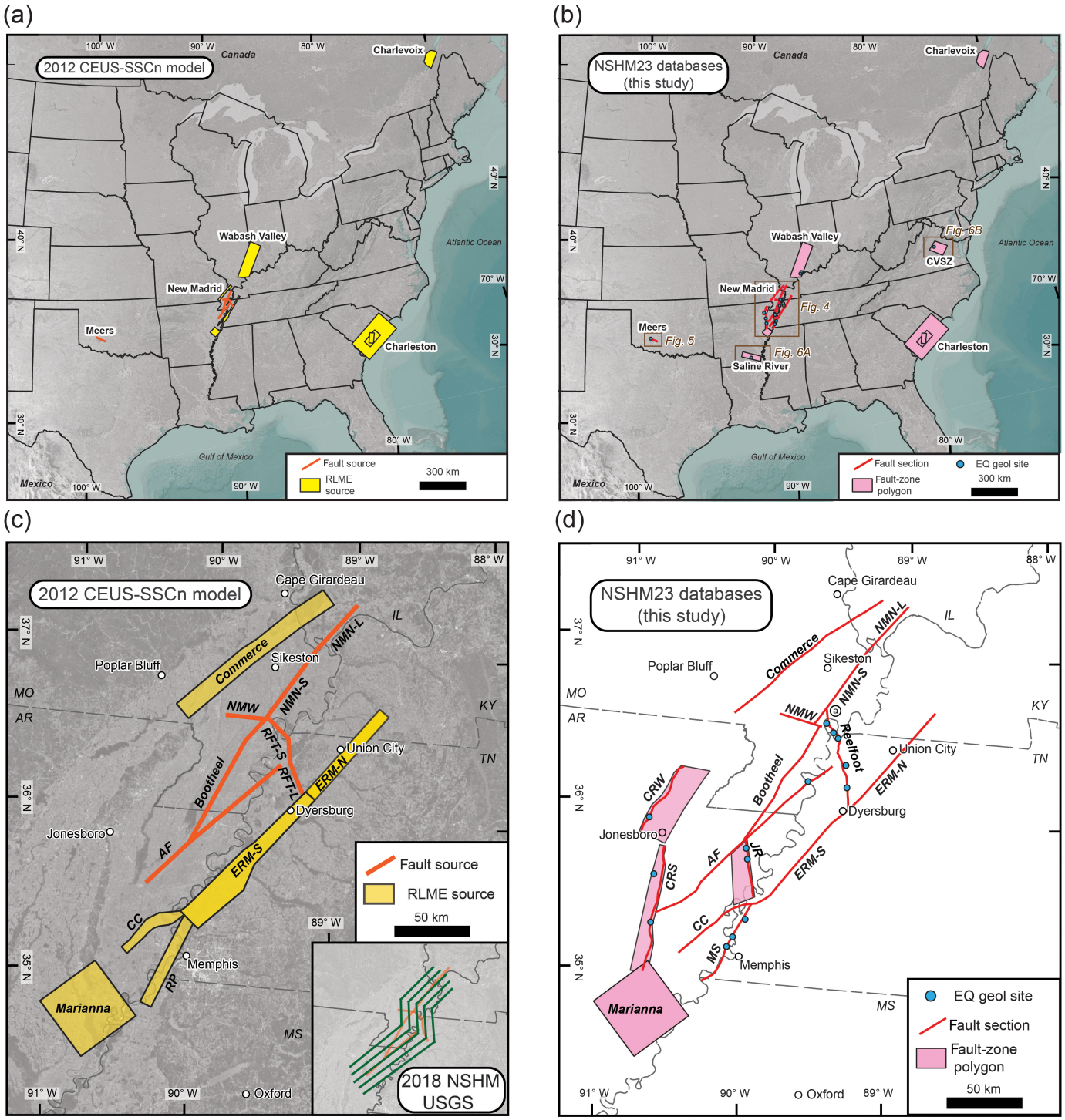

horizontal Global Positioning System (GPS) velocity vectors provided by Zeng (2022a). The four geodetic-based models also include corrections for "ghost transients," meaning time-dependent effects caused by viscoelastic relaxation from large historic events (Hearn, 2022); this correction increases geodetically inferred slip rates along the San Andreas corridor, making them more consistent with geology (refer to Pollitz *et al.*, 2022, their fig. S4).

Models also utilize a more refined inference and correction for creep (Johnson *et al.*, 2022), which is based on a factor of

Figure 6. CEUS faults and fault zones. (a) The previous model ("2012 CEUS-SSCn model" from Coppersmith *et al.*, 2012) versus (b) the new model by Thompson Jobe *et al.* (2022). Zoomed-in view near New Madrid, Missouri, for the previous model (c) and new model (d). Panels (b) and (d) also show the locations of geologic studies (blue circles). Note that the "lightning bolt" model shown in the inset of panel (c) is also used in the new model. AF, Axial fault; CC, Crittenden County; CRS, Crowley's ridge (south); CRW, Crowley's ridge (west); CVSZ, Central Virginia seismic zone; ERF-N, east margin (north); ERM-S, east margin (south); JR, Joyner ridge; MS, Meeman–Shelby; NMN-L, Charleston uplift; NMN-S, New Madrid north; NMW, New Madrid west; RFT-L, Reelfoot; RFT-S, Reelfoot (south); and RP, River Picks. Refer to Thompson Jobe *et al.* (2022) for details. The color version of this figure is available only in the electronic edition.

TABLE 2
Deformation Models

Name (Weights*)	Description
Geologic model (review team wt: 0.2) and (final wt: 0.26)	This model, developed by Hatem, Reitman,*et al.* (2022), assigns the Hatem, Collett, *et al.* (2022) geologic slip-rate estimate for faults that have explicit constraints. For other faults, they did not simply set the preferred slip rate as the midpoint of the default categorical range. Instead, they derived slip-rate estimates (including uncertainties) by comparing regional consistency of the categorical ranges with geodetic strain rates in different tectonic subregions, thereby enabling more subtle adjustments to avoid regional biases.
Shen–Bird (review team wt: 0.25) and (final wt: 0.32)	This model, by Shen and Bird (2022), is an update of the Neokinema model by Bird (2009), which is a kinematic, finite-element code that models neotectonic crustal deformation caused by fault slip, constrained by geological fault-slip rates, tectonic stress orientations, and GPS velocities.
Zeng (review team wt: 0.25) and (final wt: 0.32)	This model, by Zeng (2022b), utilizes the method of Zeng and Shen (2017) to invert for slip-rate and strain-rate parameters based on GPS velocities and geologic slip-rate constraints assuming deep-driven dislocation sources (below a locking depth).
Pollitz (review team wt: 0.2) and (final wt: 0.08)	This model, from Pollitz (2022), assumes that interseismic crustal deformation arises from viscoelastic relaxation of the ductile lower crust and mantle in response to episodic slip events on faults, compounded by the effect of steady creep on portions of some faults.
Evans (review team wt: 0.1) and (final wt: 0.02)	This block model, by Evans (2022), is an inversion-based approach that assumes deformation is a sum of rigid block rotations plus backslip due to fault locking. The primary improvement over the previous block models is block-boundary representation for all fault sections, rather than just a subset, requiring more than 800 blocks that connect the discontinuous faults (generated with an automated algorithm).

*"Review team wt" is the original deformation-model weight suggested by Johnson *et al.* (2023), and "Final wt" is the revised, final value applied here.

~6 increase in surface creep data (mostly inteferometric synthetic aperture radar) and an elastic model inversion that solves for the spatial distribution of interseismic fault creep on California faults. Substantial creep occurs in northern California on the central section of the San Andreas fault, along the Hayward and Calaveras faults through the San Francisco Bay Area, and along the Maacama and Bartlett Springs faults to the north. In southern California, creep is observed on the Coachella segment of the San Andreas fault, the Brawley seismic zone, and along the Imperial and Superstition Hills faults.

Figure 7a shows the average slip rates from the geologic deformation model, and Figure 7b shows how the other models differ (ratios with respect to geologic model slip rates). This comparison reveals considerable variability among models in many places. This is not surprising, given slip rates are certainly underdetermined on many faults due to limited observational constraints, especially in the continental interior where GPS data are sparser. Agreement between models owes largely to how much each adheres to the preferred geologic slip-rate constraints, including the uncertainties, with the Zeng (2022b) and Shen-Bird (Shen and Bird, 2022) models effectively applying the narrowest Gaussian prior, the Evans (2022) model applying a wider Gaussian (that permits slip rates to fall outside the geologic bounds), and Pollitz (2022) applying a uniform prior over the bounds (causing the latter to often produce slip rates at the geologic minimum or maximum). The geodetic models tend to produce systematically higher values on very low slip-rate faults (≤0.1 mm/yr), which appears at least partially required by geodetic data (Pollitz *et al.*, 2022).

Branch weights

The review team (Johnson *et al.*, 2023) recommended the branch weights listed as "review team wt" in Table 2 based on a score-card evaluation of 15 different metrics. In their own words:

> *We assign the Shen-Bird and Zeng models the highest weight [0.25] based on their overall favorable comparison across all metrics. We give the Geologic model a slightly lower weight [0.2] largely because less information is used to construct this model and in also because much of the information that constrains the Geologic model (preferred slip rates, upper and lower slip rates, rake) is also used to constrain the geodetic models. The Pollitz and Evans models provide slip rate estimates that differ most from the other three deformation models. We give the Pollitz model a modestly lower weight [0.2] than the Shen-Bird and Zeng models because of systematic misfits to the geodetic data and high path integral weights in some locations. We recommend the lowest weight be assigned to the Evans model [0.1] because it displays anomalously high gradients in slip rates along faults, a large number of slip rate outliers, and numerous faults show slip sense inconsistent with geology.*

The central question is the extent to which the five slip-rate "samples" available for each fault represent an adequate

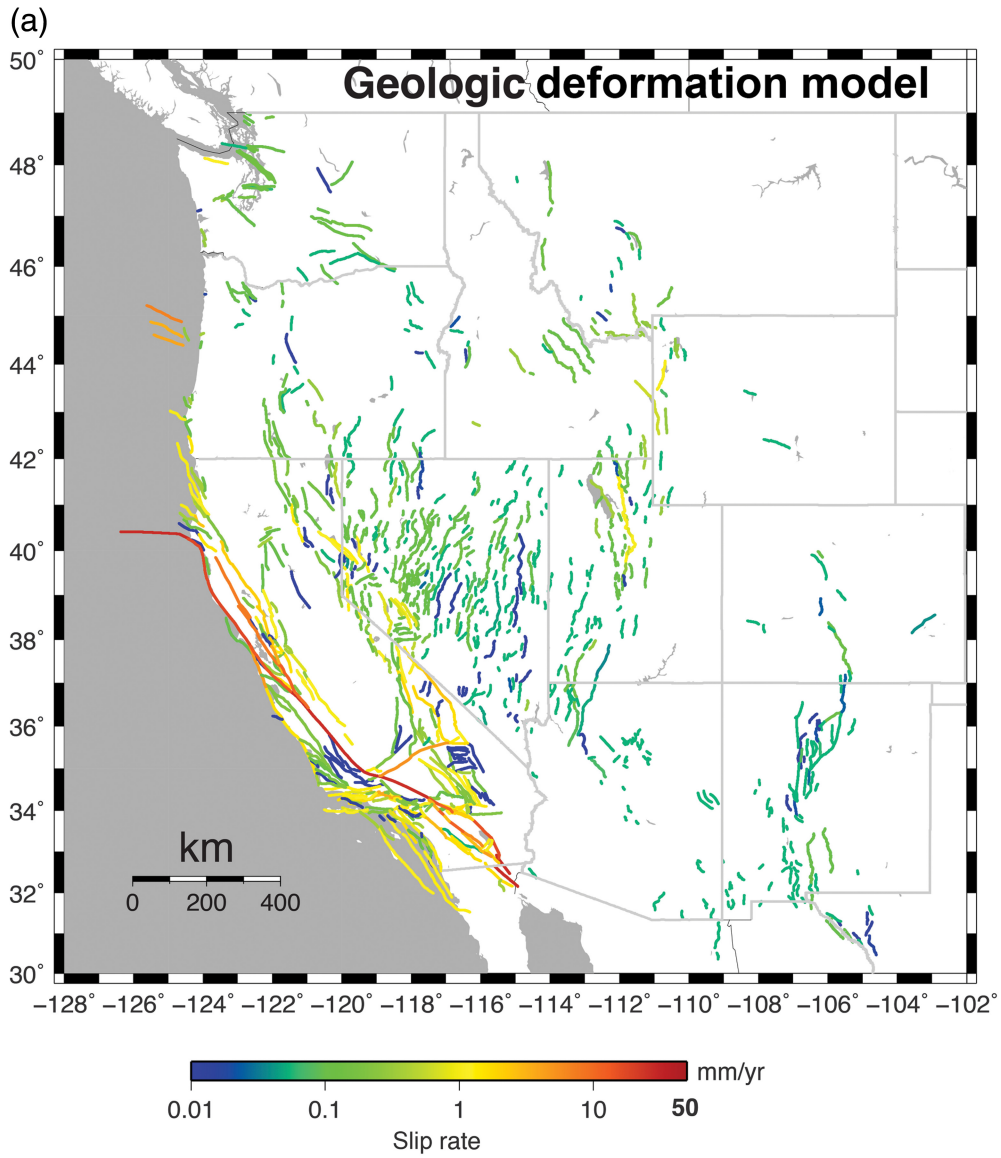

Figure 7. (a) Geologic deformation model slip rates and (b) ratio of slip rates for the four other deformation models (Table 2) relative to geologic slip rates. Adapted from Pollitz *et al.* (2022). The color version of this figure is available only in the electronic edition. (*Continued*)

approximation of the epistemic uncertainty probability distribution function (PDF; e.g., what the distribution would be if we had 10,000 credible models). Part of this question is how any null space is being sampled by each model (the range of solutions that fit the data equally well). For example, consider two parallel faults that lack direct geologic slip-rate constraints but are nestled between two GPS stations; these faults could exhibit a near-perfect slip-rate trade-off in terms of satisfying the GPS deformation (e.g., a maximum slip rate on one with a minim on the other, or vice versa, or any linear combination of these could fit the data equally well). Ideally, we would sample multiple models to represent this epistemic uncertainty, for which the average of these would split the difference (equal slip rates on each fault). This average would seemingly reflect what we want from a policy perspective if we are getting only one sample from a given model (as is the case here). The Zeng and Shen-Bird models sample the geodetic null space by staying as close as possible to the geologic constraint. The Pollitz and Evans models are less restrictive, by design, and therefore have a greater number of outliers in both the directions, and we cannot rule out the possibility that many of these slip rates better approximate the system. However, questioning the robustness of high versus low outliers on nearby faults is warranted, could the slip rates be swapped without degrading the fit to data? This gets at the question of whether currently reported slip rates represent an average of all viable samples from the null space of each model. This question has not been thoroughly investigated and represents an important challenge to be addressed.

The question here is how to handle the five slip-rate samples we have for each fault, and it turns out that outliers are quite consequential. This was discovered by examining hazard maps generated with the original weights (Table 2), for which mean hazard was appearing far above the median. Because hazard generally scales linearly with slip rate, we can illustrate the problem here without resorting to hazard calculations (slip rate change is a good proxy for hazard change). Figure 8a shows a scatter plot of the original branch-averaged slip rate versus the median for each fault section, indicating that 12% of the means are more than a factor of 2 above the median, and Figure 8b shows all the individual model slip rates versus the median (color coded by deformation model). The most extreme case is the King Range fault in northwest California, for which the mean (0.84 cm/yr) is a factor of 60 above the median (0.014 cm/yr) due to the Evans model having a slip rate that is a factor of 570 above the median (8.0 cm/yr). Thus, high slip rate outliers can have a disproportionate influence on mean hazard, because the slip rate can be no less than the product of the outlier value times

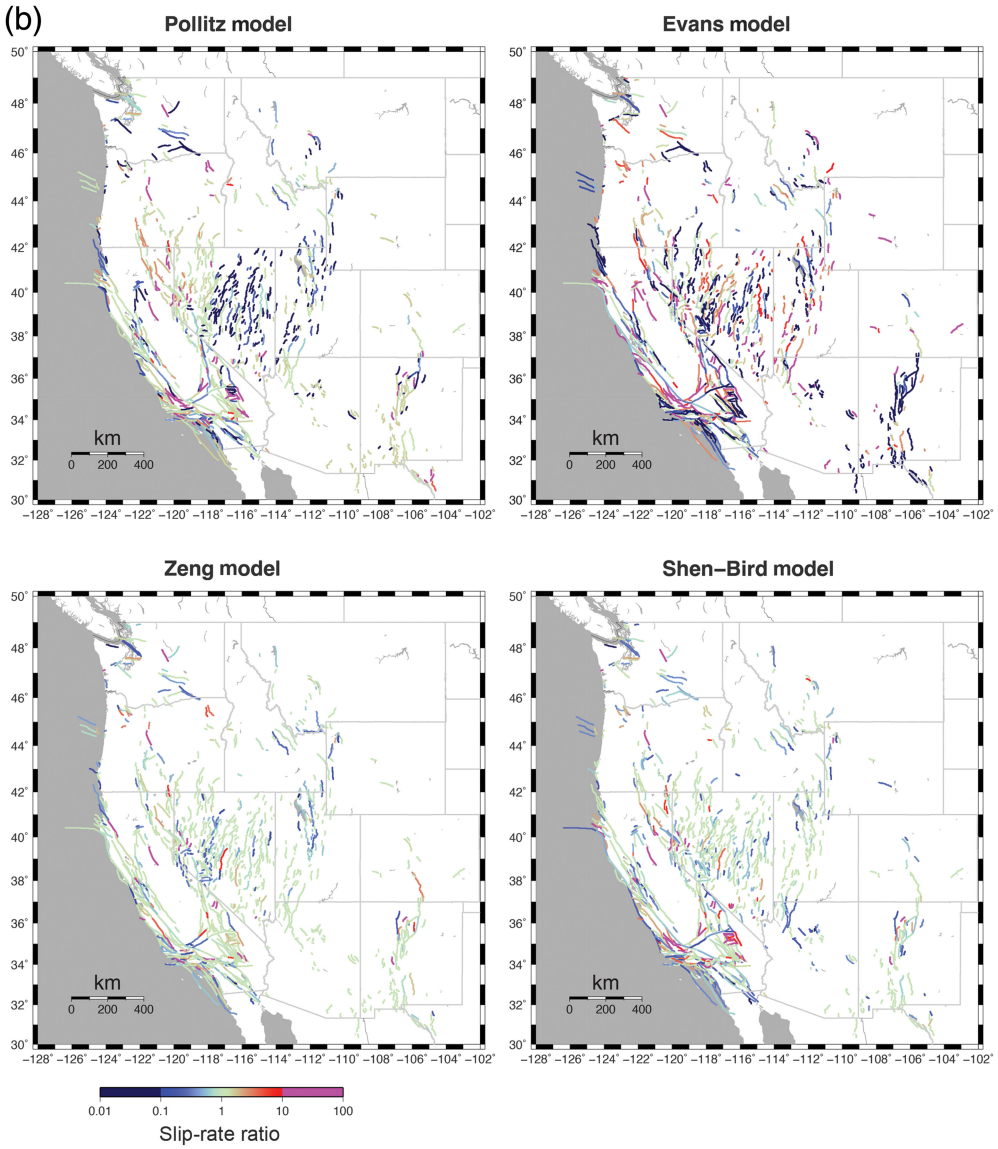

Figure 7. Continued

that model's weight. For example, if an outlier is a factor of 100 above the average of the other models, the average is increased by more than factor of 20 if all five models are equally weighted. This bias is asymmetric with respect to outliers at the low end, because a slip rate of zero can only bring the mean down by 20% if weights are equal, which explains why the means are generally pulled above the medians in Figure 8a.

One solution is to use a deformation model composed of median slip rates for our "best estimate" hazard model (propagating this through all other logic tree branches), while keeping the individual branches with their respective weights to better understand overall epistemic uncertainties. This makes sense from a policy perspective in that slip rates effectively stay anchored near geologic values unless at least three models deviate in the same direction and with the third-least outlier being adopted as the slip rate. The disadvantage is that we have yet another model to process and document, and this goes for any users who want to implement and explore epistemic uncertainties themselves (and we do not want anyone to ignore deformation model epistemic uncertainties because they are among the most consequential). In other words, there is a danger that adding this complexity could represent a further impediment to properly exploring epistemic uncertainties, especially among user groups.

Another solution suggested and explored by members of the participatory review panel is to apply an outlier replacement scheme, which seems to work well, but requires some arbitrary decisions and additional processing steps. In the end, we opted for the simplest approach of downweighting models that have both null-space-sampling questions and concerning outliers. Specifically, where the mean is more than a factor of 2 above the median in Figure 8a, the Evans and Pollitz models contribute the most consequential outliers in 64% and 24% of these cases, respectively. We therefore lowered the weight on the Evans model from 0.1 to 0.02 and that on the Pollitz model from 0.2 to 0.08 (and consequently raised the weights on the other models proportionally; Table 2). A scatter plot of mean versus median slip rates following this revision is shown in Figure 8c. The fraction of faults in which the mean is more than a factor of 2 above the median is now 5% (down from 12%), and the Evans and Pollitz models contribute the most consequential outliers for 16% and 14% of these cases (down from 64% and 24%, respectively). We not only used these final weights in the model presented here, but we also evaluated this against hazard computed using the median slip-rate model and the various outlier pruning schemes described earlier to confirm overall consistency.

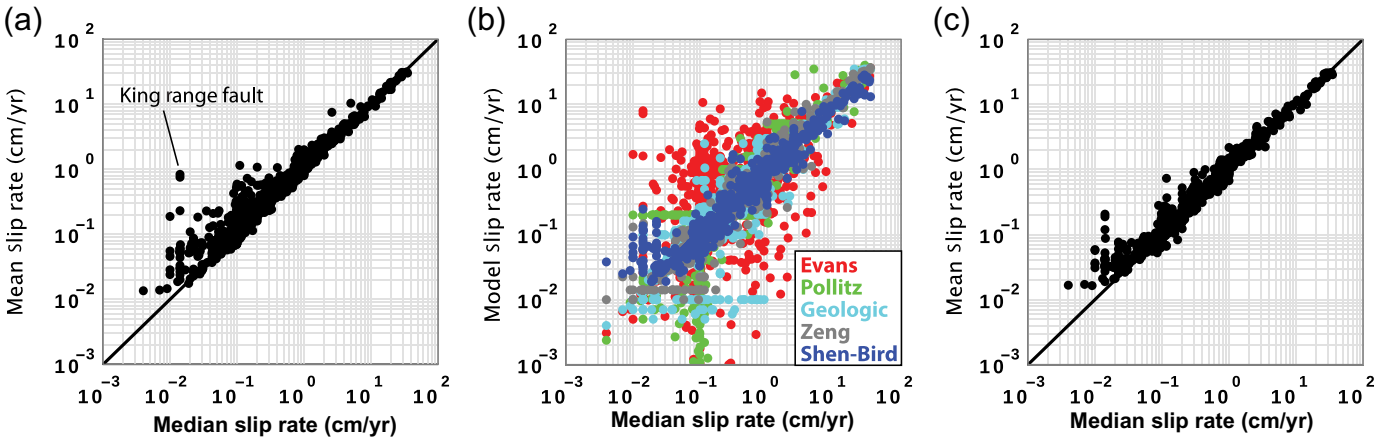

Figure 8. Deformation model slip-rate scatter plots. (a) Original branch-averaged slip rate versus the median among all models for each fault section (based on the weights recommended by the deformation model review team, Table 2). (b) The slip rate from each deformation model (Table 2, color coded as labeled) versus the median. (c) Branch-averaged slip rates, based on final revised weights (Table 2), versus the median. The color version of this figure is available only in the electronic edition.

One might also be tempted to apply regionally dependent weights, and in fact there was much discussion of this during development and review, but this raises challenges that could not be addressed for the ERF-CONUS-2023-TI (like exactly how to define the subregions and associated weights). That said, site specific studies could reweight the complete set of hazard curves with customized weights (with the implicit assumption that the weights apply to all faults that influence the hazard at a site), but this would obviously need to be based on science.

Off-fault deformation

The four geodetic deformation models also provided estimates of off-fault deformation (fig. 14 of Pollitz *et al.*, 2022 or fig. 4 of Johnson *et al.*, 2023). However, and as in UCERF3, it is not clear how much of the implied features are real versus artifacts of model assumptions and approximations, so we have once again declined use of these, at least for the ERF-CONUS-2023-TI. This is consistent with recommendations of the review team (Johnson *et al.*, 2023), which also discusses what it might take to improve such estimates.

EARTHQUAKE RATE MODELS

An earthquake rate model gives the long-term rate of every possible earthquake rupture in a region (and at some level of discretization). The model is essentially a list of "sources," for which each of the latter represents a collection (or list) of related ruptures. The next four sections define and describe each of the source model types, and the instances developed and utilized in this update, followed by a section describing details and issues associated with combining them into a complete model. The goal has not only been to be as concise as possible, but also to highlight all salient changes and influential decisions; many important but potentially distracting implementation details can be found in the references cited.

Inversion-based fault system solutions

An inversion-based fault system solution is just one type (or subclass) of fault system solution, with the latter being defined as a source that represents the long-term rate of every possible rupture on a potentially interconnected fault system. More specifically, this generalized source is composed of:

1. a list of fault subsections (including a finite-surface representation of each), and
2. a list of fault ruptures (each of which has a magnitude, long term rate, average rake, and a finite rupture surface defined as a list of utilized subsection indices).

The primary advantage of this source type is representation of multifault ruptures, although it is equally applicable to a single, isolated fault (e.g., Field, Milner, and Page, 2020). In addition, this definition says nothing about how the model is created; traditionally, this was via an inversion approach (discussed subsequently), but it could also represent a prescriptive model (e.g., segmented or isolated faults with a prescribed magnitude–frequency distribution (MFD) and "floating" rupture assumptions) or a model inferred from multicycle physics-based simulators, the latter of which might also provide rupture slip-time histories for use in physics-based ground motion modeling (e.g., Milner *et al.*, 2021). Another important advantage is built-in tools for computing implied attributes such as slip rates, recurrence intervals, nucleation and participation MFDs, and slip probability distributions along strike (e.g., to predict what would be seen at a paleoseismic site; Hecker *et al.*, 2013). Depending on how the model is constructed, potential disadvantages are discretization issues and non-smooth models (e.g., jagged MFDs).

At present, all WUS faults are modeled as fault system solutions, with the vast majority being inversion based. The inversion approach is now well-documented in the literature

(Andrews and Schwerer, 2000; Field and Page, 2011; Field *et al.*, 2014; Page *et al.*, 2014; Field, Milner, and Page, 2020; Valentini *et al.*, 2020), and one could argue that these models have undergone much more scrutiny and testing than the classic models discussed subsequently. Significant uncertainties remain, however, especially with respect to the prevalence of multifault ruptures, with Schwartz (2018) arguing that UCERF3 went too far and Page (2021) countering that it did not go far enough. To acknowledge this uncertainty, and to better quantify the influence on hazard, recent papers have endeavored to make the degree of segmentation and the propensity for multifault ruptures an adjustable parameter (Field, Milner, and Page, 2020; Valentini *et al.*, 2020). Further improvements on this and other aspects of the inversion have also been made in the context of this project, leading us to assert that we can now span a complete range of reasonable models (e.g., from strictly segmented models to ruptures that can jump up to 15 km). Full details of the new inversion protocol are given in Milner and Field (2023), including a quantification of methodological differences (by comparing UCERF3 results to the new inversion protocol applied with UCERF3 data constraints). This new inversion protocol and results for WUS faults are summarized here.

Defining the rupture set. The goal of the inversion is to quantify the rate of all plausible supra seismogenic ruptures, which are defined as events that have rupture lengths greater than or equal to the down-dip width (DDW). To this end, the 1016 fault sections are subdivided into lengths that are equal to (or just less than) half the DDW, yielding 5572 subsections in the WUS (and note that, to avoid confusion, the original fault sections are sometimes referred to as "parent fault sections"). Supra seismogenic rupture surfaces are defined by two or more neighboring subsections.

The consequent set of possible earthquakes is effectively infinite without further considerations, so a plausibility filter is applied to cull the ruptures to a credible, representative, and manageable set. A new approach was developed by Milner *et al.* (2022) for this purpose, which, relative to that applied in UCERF3, is more permissive and has more connectivity (e.g., rupture jumps up to 15 km), yet heavily penalizes long ruptures that take multiple improbable jumps. It also reduces the number of nearly identical ruptures by increasing rupture lengths geometrically at large magnitudes. Milner *et al.* (2022) also found the new approach to be more consistent with results implied by the RSQSim multicycle physics-based simulator (Dieterich and Richards-Dinger, 2010; Shaw, 2019).

Figure 9 shows which sets of WUS faults are interconnected by <15 km, implying multifault ruptures are possible almost everywhere. Applying the Milner *et al.* (2022) plausibility filter to the WUS fault model yields 582,004 ruptures, which is roughly double the number in UCERF3. Again, this is the set that is considered to have a nonzero probability of occurrence; the long-term rates will be determined by the inversion.

Treatment of fault creep. The Johnson *et al.* (2022) analysis of creep also provided deformation model-specific moment-rate reductions (*creep fraction*) for each creeping fault. Following UCERF3, we partition this between an *aseismicity factor* (a reduction in rupture area) and a *coupling coefficient* (a reduction of slip rate). The idea is that for slowly creeping faults, creep occurs predominantly at the top of the seismogenic zone, resulting in a reduction of seismogenic area, whereas there is creep at all depths for highly creeping faults, which effectively reduces the seismogenic slip rate, and therefore the rate of ruptures through highly creeping areas. We define a threshold creep fraction (γ), such that if creep fraction $\leq\gamma$

$$\text{aseismicity factor} = \text{creep fraction}$$

$$\text{coupling coefficient} = 1.0,$$

or if creep fraction $>\gamma$:

$$\text{aseismicity factor} = \gamma$$

$$\text{coupling coefficient} = 1.0 - \frac{1}{1-\gamma}(\text{creep fraction} - \gamma).$$

In UCERF3, the creep fraction threshold was set as $\gamma = 0.9$, meaning rupture areas were reduced by up to 90%. This rather large reduction was applied to get magnitude (M) ~6 earthquakes from the Parkfield section of the San Andreas fault. We have lowered γ to a more physically realistic value of 0.4 here, in part, because the new creep and deformation models imply greater creep fractions at Parkfield, and consequent magnitudes are within uncertainties. UCERF3 also capped *creep fraction* at 0.95 (preventing seismogenic slip rates from going to zero on the San Andreas fault creeping section); we have relaxed this cap, because the deformation models now span a wider range of implied moment-rate reductions. For faults that lack a *creep fraction* constraint, we apply a default value of 0.1 (the approximate average over where it is known), consistent with UCERF3.

Scaling relationships. The magnitude and average displacement for each rupture are defined by a scaling relationship, the choices of which are based on the recent revaluation by Shaw (2023). The four magnitude–area scaling relationships for plate boundary faults are as follows:

$$M = \log(A) + 4.1$$

(Working Group on California Earthquake Probabilities [WGCEP], 2003),

$$M = \log(A) + 4.2$$

(WGCEP, 2003),

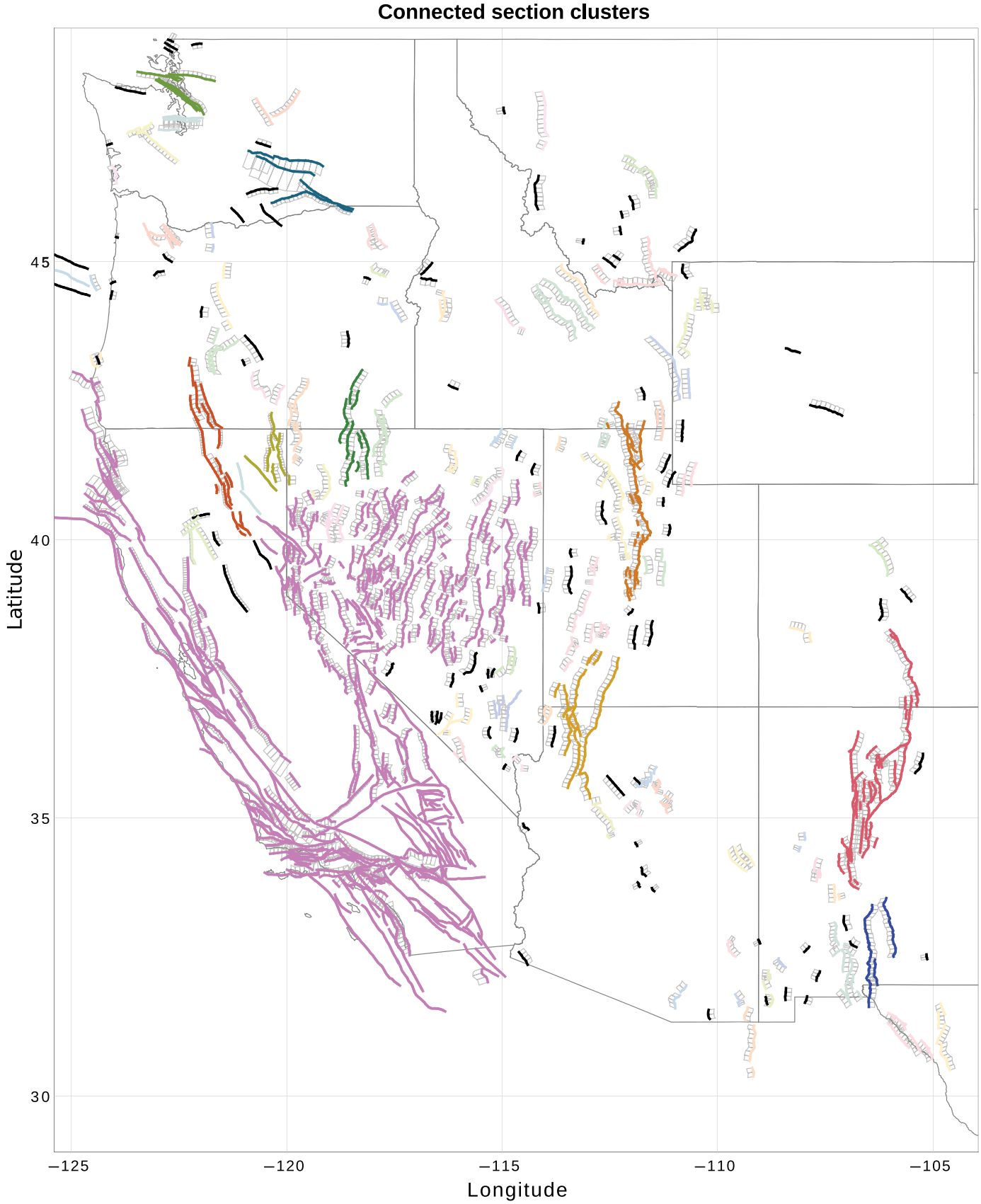

Figure 9. WUS fault system interconnectivity. Colors represent sets of faults that are connected by <15 km (measured in three dimensions). There may not be any single rupture that connects all such sections, but, rather, chains of ruptures connect the sections. Only the 10 largest clusters are plotted with bold colors; smaller clusters are plotted in random saturated colors, and fully isolated faults are plotted in black. The color version of this figure is available only in the electronic edition.

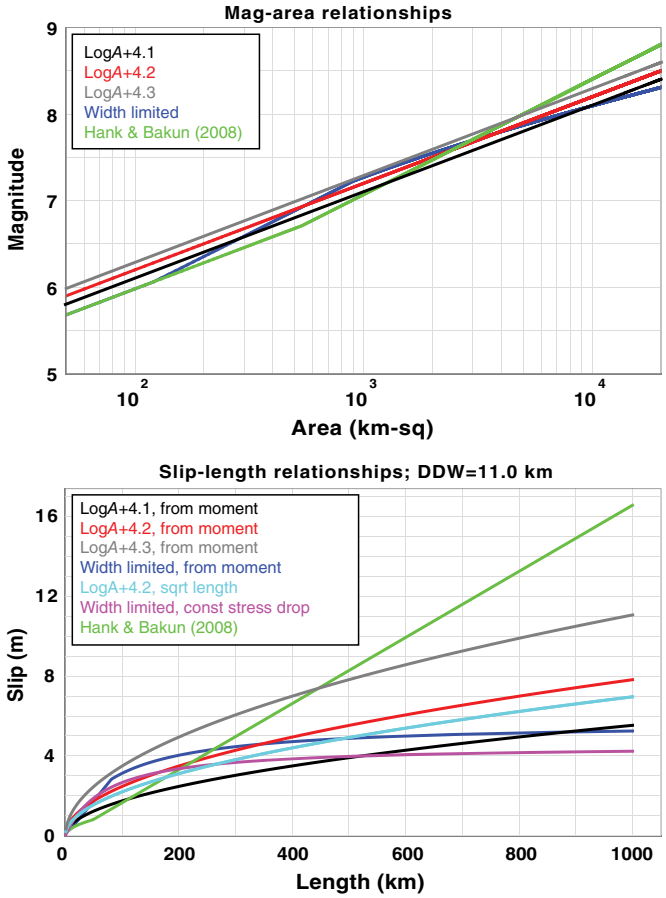

Figure 10. (a) The magnitude–area and (b) slip–length relationships utilized here, plus one (Hanks and Bakun, 2008; green) used previously in the Uniform California Earthquake Rupture Forecast, Version 3 (UCERF3), but now excluded due to the large, implied slips for long ruptures (refer to Shaw, 2023 for full description). These curves assume a down-dip width (DDW) of 11 km. The color version of this figure is available only in the electronic edition.

$$M = \log(A) + 4.3$$

(WGCEP, 2003),

$$M = 3.98 + \log(A) + (2/3)\log\left(\frac{2\mathrm{Max}\left(1.0, \sqrt{A/W_o^2}\right)}{1 + \mathrm{Max}\left(1.0, \left(\frac{A}{7.4W_o^2}\right)\right)}\right)$$

(Shaw, 2023), in which M is the magnitude, A is the area (kilometers, and reduced by aseismicity factor), and W_o is the original DDW (unreduced by aseismicity). These options, plotted in Figure 10a, are referred to as "Log$A$ + 4.1," "Log$A$ + 4.2," "Log$A$ + 4.3," and "width limited," respectively. Log$A$ + 4.3 was added after Shaw (2023) was published to represent the possibility of even larger slip for given rupture length, based on reasons documented by the review panel (Jordan *et al.*, 2023).

Three different approaches (Shaw, 2023) are used to get average slip for each rupture (D_r). The first, called "from moment," is computed from the magnitude-implied moment ($Mo_r = 10^{1.5M+9.05}$), rupture area (A_r), and shear modulus ($\mu = 3.0 \times 10^{10}$ Pa) as follows:

$$D_r = \frac{Mo_r}{\mu A_r} = \frac{10^{1.5M+9.05}}{\mu A_r}.$$

The second average slip equation, called "sqrt length," is

$$D_r = 0.22\sqrt{L_r},$$

in which L_r is rupture length in kilometers, and the third, called "const stress drop," is

$$D_r = 0.151\left[\frac{7}{3L_r} + \frac{1}{30}\right]^{-1}.$$

The logic tree branches shown in Figure 2 represent the six scientifically viable combinations of the three magnitude and three average slip equations, each of which is given equal weight (refer to Shaw, 2023 for details, including full functional forms of equations in terms of physical parameters). Figure 10b shows implied average slip versus rupture length for the six branches. The "sqrt length" and "const stress drop" relationships, relative to "from moment," generally give smaller D_r for longer ruptures. This difference reflects the epistemic uncertainty regarding the depth to which large ruptures penetrate; the from moment model assumes that ruptures do not penetrate below the depth of microseismicity, necessitating a larger average slip than typically observed at the surface, whereas the other two models assume that surface slip is consistent with that at depth, and that large ruptures must therefore penetrate to greater depths.

The branches are largely consistent with those applied in UCERF3, with the exception that the Hanks and Bakun (2008) model has been removed due to unrealistically large slips for large ruptures (green line in Fig. 10b), and the Log$A$ + 4.1 and Log$A$ + 4.3 options have been added to provide more epistemic uncertainty. We also removed a UCERF3 restriction in which the sqrt length and const stress models were not used if average aseismicity was greater than 0.2. All of these scaling relationships are new for faults outside California, as previous USGS NSHMs only applied the Wells and Coppersmith (1994) magnitude–length relationship in those areas (ignoring DDW variations). The latter has been abandoned for consistency, and because it is insensitive to DDW.

Slip-rate and paleoseismic event-rate matching. The equations currently used in the inversion are summarized and described in Table 3. Equation set (1) matches the slip rates provided by a chosen deformation model. These equations require a slip along rupture (D_{sr}) model, which gives the average slip on the sth subsection for the rth rupture. UCERF3 utilized two options (logic tree branches): a tapered ($\mathrm{Sin}^{1/2}$) and a uniform (boxcar) model. These alternatives were consistently nonconsequential across all hazard and risk metrics analyzed, so we now use only the uniform (boxcar) option, although the tapered option is still maintained for sensitivity

TABLE 3
Inversion-Based Fault-System Solution Equation Sets

Equation Set*	Description
(1) $\sum_{r=1}^{R} D_{sr} f_r = v_s$	**Slip-rate matching:** v_s is the subsection slip rate, and D_{sr} is the slip on the sth subsection in the rth event, averaged over multiple occurrences of the rupture and as measured at midseismogenic depth.
(2) $\sum_{r=1}^{R} G_{sr} P_r^{\text{paleo}} f_r = f_s^{\text{paleo}}$	**Paleoseismic event rate matching:** f_s^{paleo} is a paleoseismically inferred event rate estimate, G_{sr} specifies whether the rth rupture utilizes the sth subsection (0 or 1), and P_r^{paleo} is the probability that the rth rupture would be seen in a paleoseismic trench.
(3) $R_s = \frac{R_{s-1}+R_{s+1}}{2}$	**Fault section smoothness constraint:** This forces the total participation rate R_s to vary smoothly along a parent fault section, in which the s–1 and s+1 subsections are adjacent to the sth subsection.
(4) $\sum_{r}^{R} f_r = f^{\text{apriori}}$	**A priori constraint**: This constrains a set of ruptures ($,R$) to share a collective target rate (f^{apriori}).
(5) $\sum_{r=1}^{R} M_{gr}^{m} f_r = R_g^m$	**Regional MFD constraint**: This enables forcing a group (g) of ruptures (e.g., those in a geographic region or those on an interconnected set of faults) to have a specified total MFD, such as Gutenberg–Richter. R_g^m represents the nucleation rate for the mth magnitude bin for the gth rupture group. Matrix M_{gr}^m indicates whether the rth rupture is both part of the gth group and falls in the mth magnitude bin (0 or 1).
(6) $\sum_{r=1}^{R} M_{sr}^{m} f_r = R_s^m$	**Fault section MFD constraint**: This enables forcing subsections to have a specific nucleation MFDs. R_s^m is the nucleation rate for the mth magnitude bin on the sth subsection. Matrix M_{sr}^m contains the product of whether the rth rupture falls in the mth magnitude bin (0 or 1) multiplied by the fraction of that rupture that nucleates on the sth subsection.
(7) $R_{ss} \le F_{ss} \text{Min}(R_s, R_{\acute{s}})$	**Basin segmentation constraint**: This constrains the maximum co-rupture rate ($R_{s\acute{s}}$) between two subsections (s and $\acute{s}$) to be less than or equal to a specified fraction ($F_{s\acute{s}}$) of the lowest participation rate on either subsection (R_s and $R_{\acute{s}}$).
(8) $R_{s\acute{s}} \le \text{Min}\left(1, e^{\frac{d_{s\acute{s}}-\delta}{d_o}}\right) \text{Min}(R_s, R_{\acute{s}})$	**Distance-dependent segmentation constraint**: Same as equation set (7), but where $F_{s\acute{s}}$ is replaced with a function that decreases exponentially with jump distance ($d_{s\acute{s}}$) according to decay-rate parameter d_o and offset parameter δ (the latter relaxes the penalty up to this distance).

*f_r represents the frequency or rate of the rth rupture (what we are solving for).

tests. Although each deformation model provided a fault-specific slip-rate uncertainty, we originally assumed a 10% standard deviation due to questions of overall reliability and consistency between models, and to control the inversion behavior for which uncertainties are high (essentially overfitting the data with an assumption that a given deformation model is correct). This 10% uncertainty turned out to be too large for higher slip-rate faults (poor solution fits), which we remedied by applying a 10% cap to uncertainties, retaining the original deformation model uncertainty if it is less than this threshold, which is often the case for high slip-rate faults.

Equation set (2) matches paleoseismic recurrence intervals as in the previous studies, and equation set (3) enforces an along-strike smoothness to prevent strong rate spikes or troughs at paleoseismic sites (or where segmentation is imposed, as discussed subsequently); this was applied independently in UCERF3 for each magnitude bin, but we have since determined that applying this to the total supra seismogenic rate is adequate (Field, Milner, and Page, 2020). We also now have three logic tree branches with respect to how well paleoseismic recurrence intervals are fit (under-, even-, and overfit; Figure 2) to further quantify the influence of these data (in UCERF3 results were effectively slightly underfit); this was achieved by multiplying data uncertainties in the inversion by 0.2, and 10 for the over and underfit cases, respectively

Equation set (4) constrains a group of ruptures to have a specified total rate, which is only used to ensure that M ~6 ruptures on the Parkfield fault section have a collective rate of once every 25 yr (as was done in UCERF3).

Target MFDs and *b*-value branches. Equation set (5) in Table 3 imposes a total regional MFD constraint for supraseismogenic, on-fault ruptures. This was derived using a reasonable but somewhat complex and confusing procedure in UCERF3, which involved summing gridded seismicity rates inside assumed fault zone polygons and making other assumptions to obtain the target MFD. As such, the target MFD was conditioned on the gridded seismicity branch, increasing the number of inversions by a factor of 18 (the number of gridded seismicity branches in UCERF3; here it would be a factor of 54). Our new inversion protocol decouples inversion-based fault system solutions from the gridded seismicity model; that is, the gridded seismicity model now depends on the inversion rather than the other way around.

It is useful to introduce another constraint and logic tree branch before discussing how the total regional target MFD is now computed. Equation set (6) allows us to target a specific nucleation MFD on each fault subsection. In UCERF3, this was used to constrain results to be as close to the previous model (UCERF2; Field *et al.*, 2009) as possible, thereby allowing deviations from UCERF2 only to the extent required by other data constraints. Although this was defensible at the time from a policy perspective, it did limit the range of epistemic uncertainties considered and perhaps anchored the model inappropriately.

To map out a more complete set of models, we sweep over a range of target on-fault b-values for supraseismogenic rupture nucleation. The target MFD in equation set (6) is generated for each fault subsection by constructing a truncated Gutenberg–Richter (GR) distribution between the minimum and the

TABLE 4
Segmentation Branch Options

Branch Name	Segmentation Rules Applied
None	No segmentation constraint (jumps allowed up to 15 km) No limit on the maximum rupture length
Low	Distance-dependent parameters: $d_o = 4$ km; $\delta = 3$ km Maximum rupture length = 800 km San Andreas fault (SAF) creeping section: $F_{ss} = 0.75$* Wasatch: $F_{ss} = 0.75$
Medium	Distance-dependent parameters: $d_o = 3$ km; $\delta = 2$ km Maximum rupture length = 700 km SAF creeping section: $F_{ss} = 0.5$ Wasatch: $F_{ss} = 0.5$
High	Distance-dependent parameters: $d_o = 2$ km; $\delta = 1$ km Maximum rupture length = 600 km SAF creeping section: $F_{ss} = 0$ Wasatch: $F_{ss} = 0.25$
Classic	Parent fault sections prevented from rupturing with neighbors and ruptures are prescribed using target MFDs† "Special" faults can rupture designated sections ($d_o = 2$ km; $\delta = 1$ km) Maximum rupture length = 500 km SAF creeping section: $F_{ss} = 0$ Wasatch: $F_{ss} = 0$

*Note that the SAF creeping section fractional passthrough constraint is applied at each end of the parent fault section (see Milner and Field, 2023 for details).
†Note that if supra-seismogenic *b*-value = 0, full-fault rupture is applied for nonspecial faults to be consistent with traditional implementations.

maximum supraseismogenic magnitude on that subsection, applying the chosen *b*-value and scaling the *y* axis to satisfy the moment rate implied by the target subsection slip rate (from the chosen deformation model). By applying a range of *b*-values (e.g., branches between 0.0 and 1.0; Fig. 2), we are effectively sweeping over a range of total rupture rates (because the latter varies monotonically with *b*-value). Total rupture rate is a reasonable proxy for hazard, and varying *b*-value allows us to dial between the two extremes: the maximum rate model (if only the minimum magnitude ever occurs) and the minimum rate model (if only the maximum magnitude occurs); refer to figure 6 of Field, Milner, and Page (2020) for an illustration of this. Instead of applying the entire nucleation MFD to each subsection, we also support the option of applying only total nucleation rate, which was found by Field, Milner, and Page (2020) to produce equivalent hazard even though final MFDs can be a bit different (their fig. 16). We use the latter constraint in the inversion results presented here (i.e., we apply a *b*-value consistent total rate constraint to each subsection rather than a complete target MFD; this is equivalent to removing the *m* superscript in equation set 6 or having a single magnitude bin that is wide enough to include all ruptures).

The total regional MFD constraint for supraseismogenic ruptures (equation set 5) is simply the sum the subsection MFD targets just described. We assume that supraseismogenic, on-fault *b*-values are correlated across the region, which, as noted in the Introduction, may not be correct. Although adjacent fault sections most certainly have correlated *b*-values, because they participate in the same larger events, it is reasonable to presume that distant faults do not. It is not clear how one would define and sample from some *b*-value correlation structure, so we are stuck with assuming perfect spatial correlation, at least for now. Again, this is a safer assumption for site-specific hazard curves, but reconsideration of outlier branch weights might be appropriate for spatially distributed studies (e.g., portfolio risk analyses), but such adjustments should be based on science.

Segmentation constraints. The simplest segmentation constraint (equation set 7, Table 3) involves constraining the co-rupture rate of two subsections (i.e., on opposite sides of a segmentation boundary) to be less than some specified fraction (F_{ss}) of the minimum final participation rate on either of those subsections (referred to hereafter as the "fractional passthrough rate"). As F_{ss} goes to zero, no ruptures can pass through the boundary, and the constraint has no impact as it goes to 1.0. This constraint is applied at the Wong *et al.* (2016) segmentation points on the Wasatch fault (Fig. 5), for which we apply F_{ss} values of 0.0, 0.25, 0.5, 0.75, or 1.0 depending on the segmentation logic tree branch (Table 4).

For all other faults we apply the jump-distance-dependent segmentation model represented by equation set (8), for which the fractional passthrough rate is now distance dependent. There is no penalty out to some specified distance (δ), beyond which the maximum passthrough rate falls exponentially according to the value of the decay parameter (d_o). This is an inequality constraint, meaning relative passthrough rates can be less but not more than the constraint. Figure 11 shows the passthrough rates versus jump distance for our three intermediate segmentation branches (also described in Table 4). Recall that UCERF3 had only a strict cutoff distance at 5 km, with no penalty for shorter jumps and zero allowance for longer ones.

Introducing segmentation constraints creates a potential inconsistency with how we construct the subsection target nucleation MFDs (discussed earlier). Recall that the chosen *b*-value was said to be applied out to the maximum supraseismogenic magnitude available. However, because we dial up segmentation, we must also be lowering the frequency of these largest ruptures (plus increasing the rate of smaller events to match slip rates). In other words, the target MFD should depend on the segmentation model, with more rolloff being applied at higher magnitudes for more segmented models. Milner and Field (2023) explored a variety of options for correcting this. The simplest option involves using strict distance cutoffs in the inversion, as in UCERF3, for which the target MFD algorithm described earlier is most credible (a strict cutoff in jump distance is more consistent with a

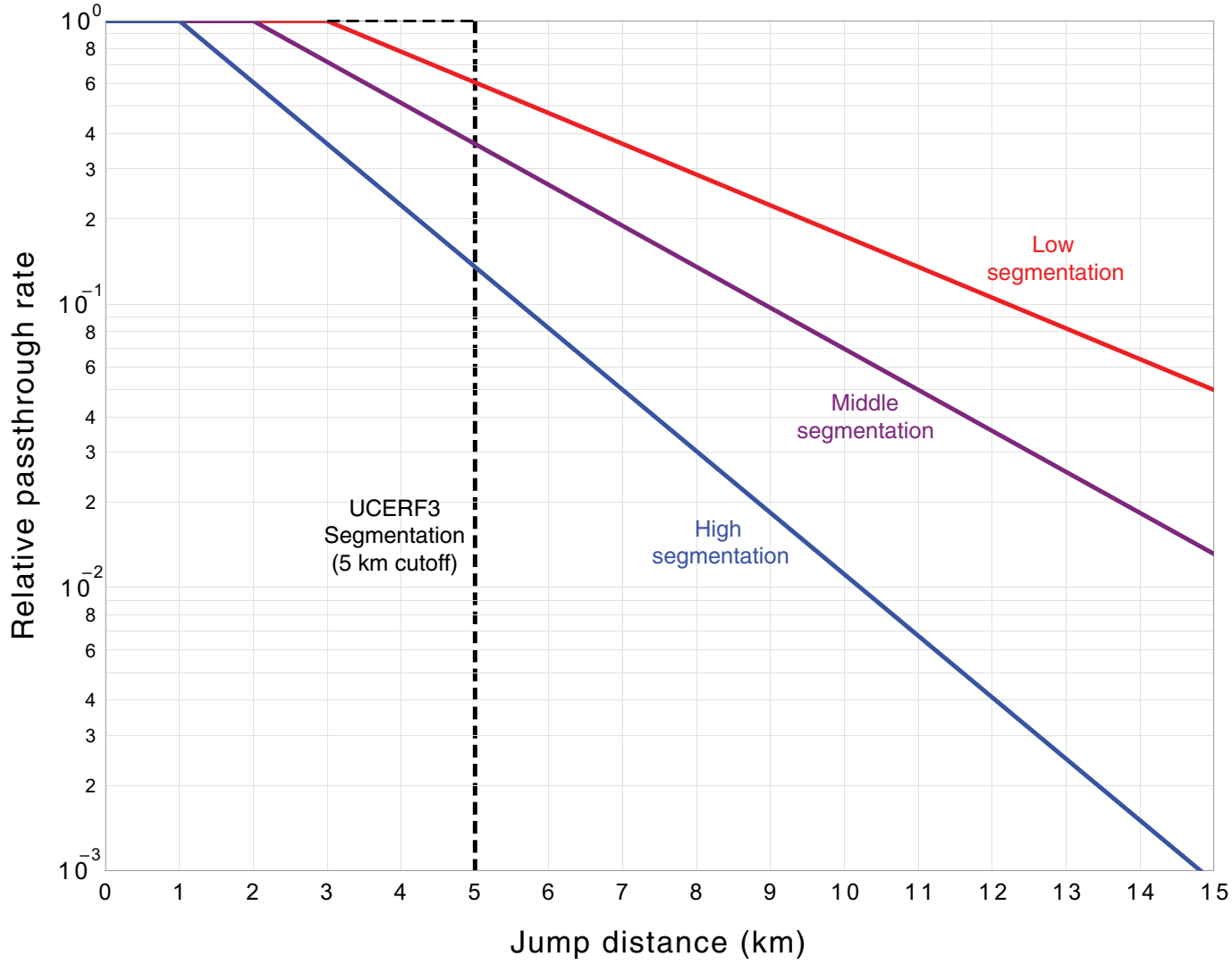

Figure 11. The solid lines represent the distance-dependent segmentation models (relative passthrough rates). The red, purple, and blue lines correspond to the low, middle, and high segmentation branch options, respectively. The dashed line depicts segmentation used in UCERF3. See Table 4 for details. The color version of this figure is available only in the electronic edition.

strict cutoff in the MFD). We then compute a suite of inversions for a range of strict distance cutoffs (e.g., at 1 km increments between 3 and 15 km) and then weight-average these solutions by whatever amounts produce the desired distant-dependent segmentation (average passthrough rates) using the property that a linear sum of models is also a viable model. Although conceptually simple (and effective), this approach requires more inversions and postprocessing steps (inverting for weights that match the distance decay and summing the models accordingly). We, therefore, not only applied one of the more conceptually complicated options for the results presented here (refer to appendix A of Milner and Field, 2023 for details), but we also confirmed that implied differences for the various options are minimal (≤3%) compared with other epistemic uncertainties.

Two final segmentation branches were applied to bracket the others with more extreme end members. One branch (*None*) applies no segmentation constraint and allows rupture jumps up to 15 km (with no distance penalty). A justification for this is that we do not really know the true connectivity at depth, so this branch errs on the side of caution (e.g., what appears to be a 10 km gap might be less). The other branch (*Classic*) mimics the traditional strict-segmentation approach in confining ruptures to parent faults sections (no jumps between them). A range of *b*-values is still applied in accordance with the logic tree branches, and rupture rates are prescribed in the traditional way (distributed uniformly along the fault) rather than conducting an inversion, unless one or more paleoseismic event rates are available. A further modification is that only full-fault rupture is imposed on the *b*-value = 0 branch (effectively changing the *b*-value to $-\infty$), thereby ensuring that we have this traditional full-fault-rupture-only model as well. Exceptions are made on this *Classic* branch for the

TABLE 5
Special Faults: The Fault Sections (Index, Name) Associated with Each of These Are Combined for the Classic Segmentation Model Branch

Name (Inclusion Basis)	Index (Name of Parent Sections Included)
San Jacinto (UCERF2 type A)*	154, Lytle Creek (San Jacinto, connector); 803, San Jacinto (Clark); 804, San Jacinto (Anza); 805, San Jacinto (stepover); 806, San Jacinto (San Jacinto Valley); 807, San Jacinto (San Bernardino); 800, San Jacinto (Superstition Mountain); 801, San Jacinto (Borrego); 802, San Jacinto (Coyote Creek)
Calaveras (UCERF2 type A)	84, Franklin; 295, West Napa; 346, Southampton; 354, South Napa; 920, Calaveras (south, Paicines); 921, Calaveras (south); 922, Calaveras (center); 923, Calaveras (north)
Hayward-Rodgers creek (UCERF2 type A)	11, Bennett Valley; 155, Maacama; 900, Hayward (south, extension); 901, Hayward (south); 902, Hayward (north); 903, Rodgers Creek-Healdsburg
Garlock (UCERF2 type A)	880, Garlock (west); 881, Garlock (center); 882, Garlock (east)
San Andreas (UCERF2 type A)	19, Brawley; 126, Imperial; 166, Mill Creek (San Andreas, north branch); 168, Mission Creek; 244, San Gorgonio Pass; 355, Cox Ranch; 700, San Andreas (Coachella); 701, San Andreas (San Gorgonio Pass - Garnet Hill); 702, San Andreas (San Bernardino, south); 703, San Andreas (San Bernardino, north); 704, San Andreas (Mojave, south); 705, San Andreas (Mojave, north); 706, San Andreas (Big Bend); 707, San Andreas (Carrizo); 708, San Andreas (Cholame); 709, San Andreas (Parkfield); 710, San Andreas (Creeping); 711, San Andreas (Santa Cruz Mountains); 712, San Andreas (Peninsula); 713, San Andreas (North Coast); 714, San Andreas (Offshore); 715, San Andreas (Banning)
Elsinore (UCERF2 type A)	840, Elsinore (Coyote Mountains); 841, Elsinore (Julian); 842, Elsinore (Temecula); 843, Elsinore (stepover); 844, Elsinore (Glen Ivy)
Wasatch (Wong *et al.*, 2016)	2780, Wasatch (Brigham City); 2778, Wasatch (Clarkston Mountain); 2789, Wasatch (Collinston); 2782, Wasatch (East Bench); 2786, Wasatch (Fayette); 2791, Wasatch (Foothills); 2785, Wasatch (Levan); 2229, Wasatch (Malad City); 2787, Wasatch (Nephi, north); 2784, Wasatch (Nephi, south); 2783, Wasatch (Provo, north); 2790, Wasatch (Provo, south); 2792, Wasatch (Salt Lake City, north); 2793, Wasatch (Salt Lake City, south); 2788, Wasatch (Virginia Street); 2781, Wasatch (Weber)
Landers (Hist. Qk)	27, Camp Rock; 78, Emerson-Copper Mountain; 119, Homestead Valley; 129, Johnson Valley (north); 135, Kickapoo; 23, Burnt Mountain; 79, Eureka Peak
Hector Mine (Hist. Qk)	113, Hector Mine; 210, Pisgah-Bullion Mountain-Mesquite Lake
Hebgen Lake (Hist. Qk)	2305, Hebgen; 2329, Red Canyon
Pleasant Valley (Hist. Qk)	1208, Pleasant Valley (Sou Hills); 1207, Pleasant Valley (Pearce); 1209, Pleasant Valley (Tobin); 1206, Pleasant Valley (China Mountain)
Cedar Mountains (Hist. Qk)	1080, Monte Cristo Valley; 1260, Gabbs Valley (unnamed); 1171, Gabbs Valley
Lost River (Hist. Qk)	2505, Battle Rock; 2226, Lone Pine
Sonora (Hist. Qk)	2062, Pitaycachi (north); 2063, Pitaycachi (south)
Fairview Peak	1173, Gold King; 1126, West Gate; 1182, Louderback Mountains; 1051, Fairview

Fault sections are either treated as such in the previous studies or based on historical earthquakes ("Hist. Qk") as noted next to the names.
*"UCERF2 type A" means that it was defined in Field *et al.* (2009). UCERF2, Uniform California Earthquake Rupture Forecast, Version 2.

"Special" faults listed in Table 5, each of which was either connected in the previous studies or has had a large historic earthquake that extended beyond individual fault sections (refer to Table 5 caption for details). For these we apply an inversion for which ruptures are confined to the set of subsections defined for each special fault (with $d_o = 2$ km and $\delta = 1$ km), and we do not apply the 0 to $-\infty$ b-value override. For the Wasatch fault, we also apply strict segmentation ($F_{ss\acute{s}} = 0$) in the inversion for this classic branch.

An additional option is whether ruptures can pass through the San Andreas creeping section, which is handled by effectively varying $F_{ss\acute{s}}$ (in equation set 7) between 0 and 1 depending on the segmentation branch (Table 4). However, on even the most permissive branch ($F_{ss\acute{s}} = 1$) there are still significant slip-rate reductions due to creep, the additional penalty provided $F_{ss\acute{s}} \le 1$ accounts for other possible dynamic rupture impediments.

A final constraint applied for each segmentation branch is the maximum rupture length, which varies from a hard cutoff at 500 km on the *Classic* branch, increases by 100 km increments on intermediate branches, and ends with no limit on the "*None*" branch. This length restriction, which has nearly zero impact on hazard metrics considered here, was added late in the project based on feedback from our review panel and for reasons that are discussed subsequently in the context of results.

Some implementation details. We continue to use the Page *et al.* (2014) simulated annealing algorithm to solve the inversion, but with some enhancements from Field, Milner, and Page (2020) and even more from Milner and Field (2023). These include refinements with respect to the various simulated annealing options (rupture sampler, perturbation function, cooling schedule, completion criteria, and nonnegativity constraint). The first author of Milner and Field (2023) has

also made the following important enhancements: (1) a new OpenSHA modules framework to track what options were used for each inversion (for reproducibility); (2) implementation of dynamic equation set reweighting to ensure more uniform fits to different data types; (3) improved code efficiencies, which have reduced compute times by a factor of 200 relative to UCERF3 computations; and (4) operationalized generation of web-based solution reports (see Data and Resources).

The inversions can be done for the entire WUS or separately for each group of interconnected faults (those depicted in Fig. 9, some of which are single, isolated fault sections). We chose the latter for the results presented here, but differences are negligible provided other constraints are handled consistently.

UCERF3 applied a slip-rate reduction of 4%–10% (depending on the logic tree branch) to account for the moment released by subseismogenic, on-fault ruptures, whereas no such reduction was made outside California in NSHM14/18. We tried but failed to come up with a new, defensible approach for specifying these values on a fault-specific basis (attempts are fraught with debatable assumptions), so we are currently applying no such correction, although a single across-the-board value (e.g., 7%) might be more defensible.

Model nonuniqueness. It is well-documented that fault system solutions are nonunique, given the underdetermined nature of the problem, because there are many more unknowns (rupture rates) than there are data constraints (Field *et al.*, 2014; Page *et al.*, 2014; Field, Milner, and Page, 2020). This means there is an effective infinite number of different models that will satisfy the data constraints (the so-called "null space"), although these are also bounded by the minimum- and maximum-rate models discussed earlier (and in Field, Milner, and Page, 2020). Given that simulated annealing is a random sampling algorithm, one might hope that multiple runs would sample the null space uniformly, thereby mapping out a complete range of models (epistemic uncertainties). However, this in not generally the case, meaning additional constraints need to be applied to sweep across the null space, and not doing this can lead to solutions that are biased by the simulated annealing starting model or rupture sampler (Field, Milner, and Page, 2020). This is one of the primary reasons we added the *b*-value branches because we believe that these give us more control over where solutions land, and allow us to sweep across a reasonable range of models between the minimum- and the maximum-rate solutions.

Another manifestation of nonuniqueness is that solutions typically have only a small fraction of nonzero rate ruptures (~9% on average here), and that different simulated annealing runs will have a somewhat different set due to the random sampling. Fortunately, these differences have negligible influence on hazard, because the latter is generally independent of the exact endpoint of ruptures (being much more influenced by the MFD at the nearest point on a fault, which is now more explicitly constrained). In fact, Field, Milner, and Page (2020) demonstrated that two solutions with no overlapping ruptures (i.e., the second run was prevented from sampling ruptures that had nonzero rates in the first) produce nearly identical hazard (their fig. 12b). Having a lot of zero rates is good in terms of faster hazard calculations (fewer ruptures to loop over) but problematic in terms of testing models against the future earthquakes (in which case it is unwise to say anything cannot happen if the data are equivocal). In UCERF3, we applied a water level to rupture rates to ensure all had nonzero values, but we have dropped this approach here in part because it has no effect on hazard. Averaging over all logic tree branches raises the percentage of nonzero rate ruptures to 99%.

Another attempt we have made is to use the random nature of simulated annealing to even fit the data, meaning it would produce a range of models for which misfit statistics exactly match the uncertainties of applied data. Unfortunately, we have not been able to get this to work either, as average models can end up significantly biased with respect to the target constraints (e.g., fig. 14 of Field, Milner, and Page, 2020). Achieving this would apparently require random sampling the data constraints (from the associated uncertainty distribution) and overfitting these samples in the inversion. The challenge is that data constraints are likely correlated (e.g., slip rates on adjacent fault subsections), so again, we have not attempted this here. The bottom line is that we have largely overfit data constraints in this study, except where there are incompatibilities between them, and the set of nonzero rate ruptures for individual branches is certainly sensitive to this overfitting (data "noise" is affecting which ruptures are given a nonzero rate). Averaging over all branches helps smooth these variations out. None of these issues have been found to affect hazard inferences.

Other considerations. Given the set of logic tree branches governing these fault system solutions, we have 2250 different inversion models. Each takes about 1 hr to compute on a typical desktop computer. The set presented here was computed on a cluster computer at the University of Southern California's Center for Advanced Computing Research, which took about 2.5 days utilizing 36 nodes (and 1.8 TB of disk space). Computing all the hazard diagnostics described subsequently took a few more days.

Also note that, in contrast to the classic fault models discussed next, the minimum supraseismogenic magnitudes vary between fault sections here, and we do not account for dip uncertainties or depth to top of rupture variability (although the latter two could be handle in the hazard calculations if desired).

Classic fault sources

This source type is the traditional representation for faults, which is typically composed of a finite-fault surface, an MFD, rules for computing rupture dimensions from magnitude, and an assumption about the along-strike probability of occurrence. The advantages here are construction simplicity and guaranteed

smooth models due to their being prescriptive (not inversion based). The disadvantages are difficulties with respect to representing multifault ruptures, computing the implied attributes noted earlier, and including a broader set of data constraints (brokering their potential inconsistencies and understanding the consequent null space). Our calling these "classic" should not be interpreted pejoratively, because we acknowledge that a simpler or less realistic model can be more useful in some applications.

The following are treated as classic fault sources in the 2023 NSHM update: Alaska faults, most of the New Madrid fault system, and the Cascadia and Aleutian subduction zones (although we plan to try fault system solution representations for each of these). It is worth noting that the New Zealand has utilized inversion-based fault system solutions for all faults, including subduction zones, in their 2023 NSHM update (Gerstenberger *et al.*, 2022).

WUS classic fault sources. All WUS fault-based sources (excluding Cascadia) are now represented as fault system solutions described earlier, whereas here we describe the previous implementations for comparison purposes. In NSHM14/18, the WUS faults outside California had two main source types (logic tree branches).

1. A full-fault, "characteristic" rupture represented with a Gaussian MFD, for which the mean magnitude is computed from the Wells and Coppersmith (1994) magnitude–length relationship, the standard deviation is assumed to be 0.12, and the Gaussian is truncated at ±2 standard deviations. Mean magnitude is capped at M 7.5, in which case the rupture is floated down the fault (uniform distribution) with a single magnitude and length from the same Wells and Coppersmith (1994) relationship. Event rates are scaled to match the target fault slip rate (generally assuming a lower seis depth of 15 km).
2. A GR MFD with the minimum magnitude of 6.5, a b-value of 0.9, the maximum magnitude implied by the Wells and Coppersmith (1994) magnitude–length relationship, and event rates that match the target slip rate. Smaller ruptures are floated down the fault (uniform distribution), with length computed from magnitude using same Wells and Coppersmith (1994) relationship. The maximum magnitude is capped at M 7.5 here too. Depth to top of rupture is magnitude dependent, being zero at the largest magnitudes, and with different options and weights being applied at lower magnitudes (0, 2, 4, and 6 km at M 6.5 with equal weights); this is considered aleatory variability.

In both the models, some epistemic uncertainty is also applied to the maximum or mean magnitude (±0.2 with a weight of 0.2 on these outer branches and 0.6 for the central one). Fault dip for reverse and normal faults is generally assumed to be 35°, 50°, or 65° with branch weights of 0.2, 0.6, and 0.2, although note that the dip variability does not influence magnitudes or event rates.

A few faults receive further special treatment as follows: (1) historical magnitudes are used for the characteristic model if available; (2) if slip rate is unavailable, any paleoseismic event-rate constraint is applied to the characteristic magnitude, and the implied moment rate is applied to the GR model; (3) if maximum or mean magnitude is ≤ 6.7, the associated epistemic uncertainty is dropped; and (4) some speculative sources (e.g., offshore) are further assigned a "probability of activity."

As discussed in the previous section, we have attempted to capture the essence of these models in our fault system solution framework presented earlier. Potentially important implementation differences include the following: (1) fixed minimum magnitude here (M 6.5) versus scaling relationship and down-dip dependent values above; (2) a single magnitude–length scaling relationship used here (plus epistemic uncertainty added for maximum and mean magnitudes), whereas a range of magnitude–area and slip-length scaling relationships are utilized above; (3) a range of depth to top of rupture values are assigned for smaller floating events here (and not considered above because they are "supra-seismogenic" ruptures; such variation could be applied in GMMs); and (4) effective along-strike discretization of floating ruptures is finer here (1 km) and coarser above (half of the DDW). With respect to magnitude–length versus magnitude–area scaling relationships, the questions are whether shallower dipping faults should have larger maximum magnitudes than vertically dipping faults (all other things being equal) and how well DDWs are constrained given uncertainties in lower seismogenic depths. Our rules for supraseismogenic ruptures above mean that the minimum magnitude on some shallow dipping faults can be as large as M 7.

CEUS fault sources. These sources were updated and described under the leadership of Allison Shumway (USGS, written comm., 2023, referred to hereafter as Shumway2023), including quantification of implied changes in mean hazard. The defining characteristic of all CEUS fault-based sources (including the fault zone sources described subsequently) is the repeating large-magnitude earthquake (RLME) hypothesis introduced by Coppersmith *et al.* (2012, referred to hereafter as "CEUS SSCn (2012)"), which assumes that all events that occur on one of these sources will have a very similar magnitude (within 0.25 magnitude units with uniform distribution as specified by CEUS SSCn (2012), but with no such aleatory variability as applied in NSHM14/18). This assumption, based on the characteristic MFD of Youngs and Coppersmith (1985), is convenient in that whatever magnitude is inferred for any previous event is that expected for all the future events. Epistemic uncertainty is acknowledged, however, for what this characteristic magnitude is, with either fault surface area or fault zone length providing an upper bound, or the spatial extent of paleoliquifaction deposits being used to constrain a reasonable range.

The mean rate of the RLME source is either inferred by moment balancing if a slip-rate estimate is available, or it is inferred from an observation of N events having occurred in some timespan T (e.g., from paleoliquefaction deposits). In the latter case, a probability density function for the mean rate of the RLME is computed from N and T assuming a Poisson process (reflecting the relative likelihood that each rate is consistent with the observation), and five points are typically chosen from this distribution as event-rate branches for the logic tree. Epistemic uncertainties on the timespan (T) are also often represented using a uniform distribution over a range of values, and sometimes alternative sets of N and T are utilized to represent whether the future will be more consistent with any quiet versus more active time periods apparent in the paleoseismic record (treated as additional epistemic uncertainty). Chapter 5 of the CEUS SSCn (2012) report describes this all quite well.

Further complications arise when faults sources are deemed capable of rupturing together. The Meers, Commerce, and Eastern Margin (north) faults are all considered isolated, and only the Meers has an influential change since NSHM14/18 (hazard is increased to the west because the fault was extended in that direction; magnitudes and rates were unchanged). The Eastern Rift Margin (south) fault always ruptures either with Crittenden County or with the Meeman-Shelby fault (branch weights of 0.6 and 0.4, respectively), and no changes in hazard are implied since NSHM14/18 (in spite of these going from a zone to an explicit fault representation; magnitudes and rate were unchanged).

The remaining faults (Charleston Uplift, New Madrid West, New Madrid North, Reelfoot, Bootheel, and Axial) are all in the heart of the New Madrid, Missouri, area, and have been modeled as capable of rupturing alone or together in a handful of alternative scenarios. One set of branches honors the scenarios defined by CEUS SSCn (2012), and another set represents a USGS alternative model that utilizes a simplified "lightning bolt" fault model (refer to inset in fig. 6c or figs. 22 and 23 of Petersen *et al.*, 2014). There are no more than three different ruptures represented among all these faults on any given branch, and each of these ruptures is assumed to recur with the exact same magnitude. The CEUS SSCn (2012) set of branches include temporal variability in the long-term rate of ruptures (in vs. out of a "cluster sequence"), whereas the USGS model (Petersen *et al.*, 2014) has a branch where ruptures come in sets (doublets or triplets) versus their being temporally independent, the distinction of which is accounted for in hazard calculations. There are other branches representing epistemic uncertainties in rates and magnitudes, resulting in a total of 640 logic tree branches (according to our count) for this set of faults. The only changes since NSHM14/18 involve fault geometry modifications, and no changes in rupture rates or magnitudes, with the biggest change in hazard being an increase where the Axial fault is extended to the southwest (Shumway2023).

In short, the only consequential changes from a hazard standpoint are where the Meers and Axial faults have been extended. None of these sources have been updated to utilize the set of scaling relationships recommended by Shaw (2023) for stable continental regions. Although all models are a mere approximation of the system, one can ask whether the representations utilized here represent the best available science. Perhaps most debatable is the RLME assumption that all ruptures for a given source will have very similar magnitudes (as opposed to a wider range of aleatory variability). Limiting every branch for the five-fault cluster near New Madrid to only three different ruptures seems questionable as well. At the very least, these assumptions are philosophically inconsistent with how we are handling faults in the WUS.

A relatively straightforward modification would be to replace the single magnitude assumption with a wider range of magnitudes using a GR distribution with alternative branches for the b-value (e.g., between 0 and 1 as applied in WUS, or even beyond this range if deemed appropriate). In addition, the map of faults near New Madrid (Fig. 6b) implies that nearly all are plausibly interconnected, which begs the question of whether an inversion fault system solution is warranted. The fact that nearly all of these faults lack slip rate estimates is not a problem, because there is no such requirement for these in the inversion. The bigger question is how to interpret the N events in time span (T) constraints provided by paleoliquefaction studies because there is potential ambiguity in terms of what ruptures could cause each such observation. Assuming it is an occurrence on the nearest fault is one approach (and consistent with present assumptions), but then there is also the question of whether such observations at different locations represent any of the same events. Exploration of these questions is ongoing.

Another challenge is the wide heterogeneity in the number of logic tree branches among these fault sources, making a systematic hazard-map assessment of the influence of each a near impossibility. One might argue that the current models go overboard with respect to epistemic uncertainties (especially compared with the very limited aleatory variability). This does not matter much if you are only interested in mean hazard (for which epistemic uncertainties can be treated as aleatory), but one of our explicit goals is a better quantification of epistemic uncertainties with respect to hazard and risk metrics, which we also need to inform where efforts should be placed to improve the models. It would therefore be helpful to reduce the branches for all these sources to a common, necessary, sufficient, and manageable set.

Cascadia subduction zone. The Cascadia subduction zone model used in NSHM14/18, defined by Petersen *et al.* (2014) and Frankel *et al.* (2015), is composed of two additive (aleatory) components: full subduction zone ruptures every 526 yr plus some $M \geq 8$ partial ruptures. Logic tree branches were included for the following: whether $M \geq 8$ ruptures are segmented or unsegmented (floating); the b-value assumed for unsegmented ruptures (0 or 1); whether $M \geq 8$ ruptures occur on the northern end of the subduction zone; and whether the overall recurrence

interval of $M \geq 8$ events is set from turbidites (every 500 yr according to Goldfinger *et al.*, 2012), onshore geology (every 1000 yr based on the tsunami deposits and subsidence data of Kelsey *et al.*, 2005 and Nelson *et al.*, 2006), or double the latter (2000 yr, based on expert opinion that some inferred earthquakes might not be subduction events). There were also three branches for down-dip rupture extent and three scaling relationships, leading to nine different magnitudes estimates for full and segmented ruptures.

Updates for the Cascadia subduction zone, which were provided under the leadership of Peter Powers (USGS, written comm., 2023, referred to hereafter as PowersCascadia2023), are based on new paleoseismic data and discussions at a virtual workshop in February 2021. These include a new segmentation-model branch proposed by Goldfinger *et al.* (2017), which allows ruptures to extend farther north; the previous segmentation model from Goldfinger *et al.* (2012) is also retained. The branch with a 2000 yr recurrence interval for $M \geq 8$ events was replaced with two others based on interpretations of onshore data by Nelson *et al.* (2021): an 800 yr recurrence interval based on data going back 1600 yr and a 2300 yr recurrence interval based on the last 7000 yr.

A notable modification is that the full subduction-zone rupture branch has been split into two aleatory parts: 90% of the time this occurs as a full rupture (as before), but 10% of the time it is occurs as a temporal cluster of M 8–9 events filling the entire length in a matter of decades. The relative frequency of the latter is low due to lack of evidence in turbidite data, and that such events would presumably not satisfy plate-boundary slip rates. Another notable addition is a branch with a time-dependent, renewal-model probability for the full subduction-zone ruptures based on a lognormal distribution with a recurrence interval of 529 yr, a coefficient of variation of 0.5, and the last event having occurred in 1700; this yields a probability of 12.5% rather than the time-independent value of 9%. Questions remain as to whether this is applicable to the temporal cluster of M 8 events (would these smaller events really reset the system?), and whether this time dependence should be applied before doing so with other faults that are late in their cycles (e.g., the Hayward fault and the Coachella section of the San Andreas fault); our review panel recommended that we hold off on applying this time-dependent option (Jordan *et al.*, 2023). No changes were made to other logic tree branches, except that a Log$A$ + 4.1 scaling relationship option was added based on the Shaw (2023) assessment. Despite these enhancements, implied changes in mean hazard are relatively minor (<10%, as shown subsequently).

Fault source zones

This source type is utilized where faulting is clearly present, or suspected, but dispersed in that a single dominant fault is not clearly identifiable. These sources are defined with a geographic polygon and an associated MFD, whereas the latter is defined to satisfy any event-rate, slip-rate, or moment-rate constraints. Ruptures are typically assumed to have a uniform distribution inside the polygon, generally modeled as gridded seismicity, but where a fixed focal mechanism is usually applied based on the observed faulting. Rupture dimensions are computed from magnitude using an assumed scaling relationship and an assumed DDW, and ruptures are centered on the grid point. The USGS generally models these as "leaky" boundaries, meaning ruptures can extend outside the polygon if they nucleate near the edge.

CEUS fault zone sources. As described in Thompson Jobe *et al.* (2022) and as led by Shumway2023, five new fault zone sources have been added (Joiner Ridge, Crowley's Ridge [south], Crowley's ridge [west], Saline River, and Central Virginia), four are unchanged (Wabash Valley, Charleston, Charlevoix, and Marianna), and five that were zones in NSHM14/18 are now explicit faults (discussed earlier). As discussed in the 2018–2023 Hazard Changes section subsequently, the main consequence is that hazard has increased where the new fault zone sources have been added.

Again, the RLME assumption is utilized here (all occurrences of a source are the same magnitude), and rates are determined by either moment balancing with slip rate or inferred from N events in time span T (described earlier). The maximum magnitude is generally determined from the polygon length in the strike direction, using an assumed scaling relationship and DDW, which is 15 km here. The Wells and Coppersmith (1994) magnitude–length relationship (for unknown rake) has been used in the past, but the new fault zone sources added here utilize the average of the three Shaw (2023) relationships for stable continental faults (refer to his table 1). Epistemic uncertainty in the RLME magnitude is generally represented between magnitude 6.5 and the maximum magnitude, discretized at 0.25 increments. All five of these new source zones were downweighted by 50% to reflect uncertainty on whether they represent unique sources (relative to gridded seismicity).

Charleston has three different sized polygons, and Central Virginia has two, reflecting additional epistemic uncertainty for these sources. The larger polygon for the larger Central Virginia source implies the maximum magnitude of about 7.25, and the observational constraint of one event in 1800–2800 yr implies the mean recurrence interval of 1333 yr. Tish Tuttle, the scientist who provided the paleoliquefaction data, expressed concern that the spatial extent of liquefaction was not consistent with such a large event, so the maximum magnitude was reduced to 6.5 (only this magnitude is considered). This is a consequence of the RLME single-sized event assumption (i.e., what is implied for the last event is all you should ever see), and it might also be questionable to apply the 1333 yr recurrence interval to$M$ 7.25 events anyway (a moment rate that would imply more topographic relief?). But are we really sure that events larger than M 6.5 cannot

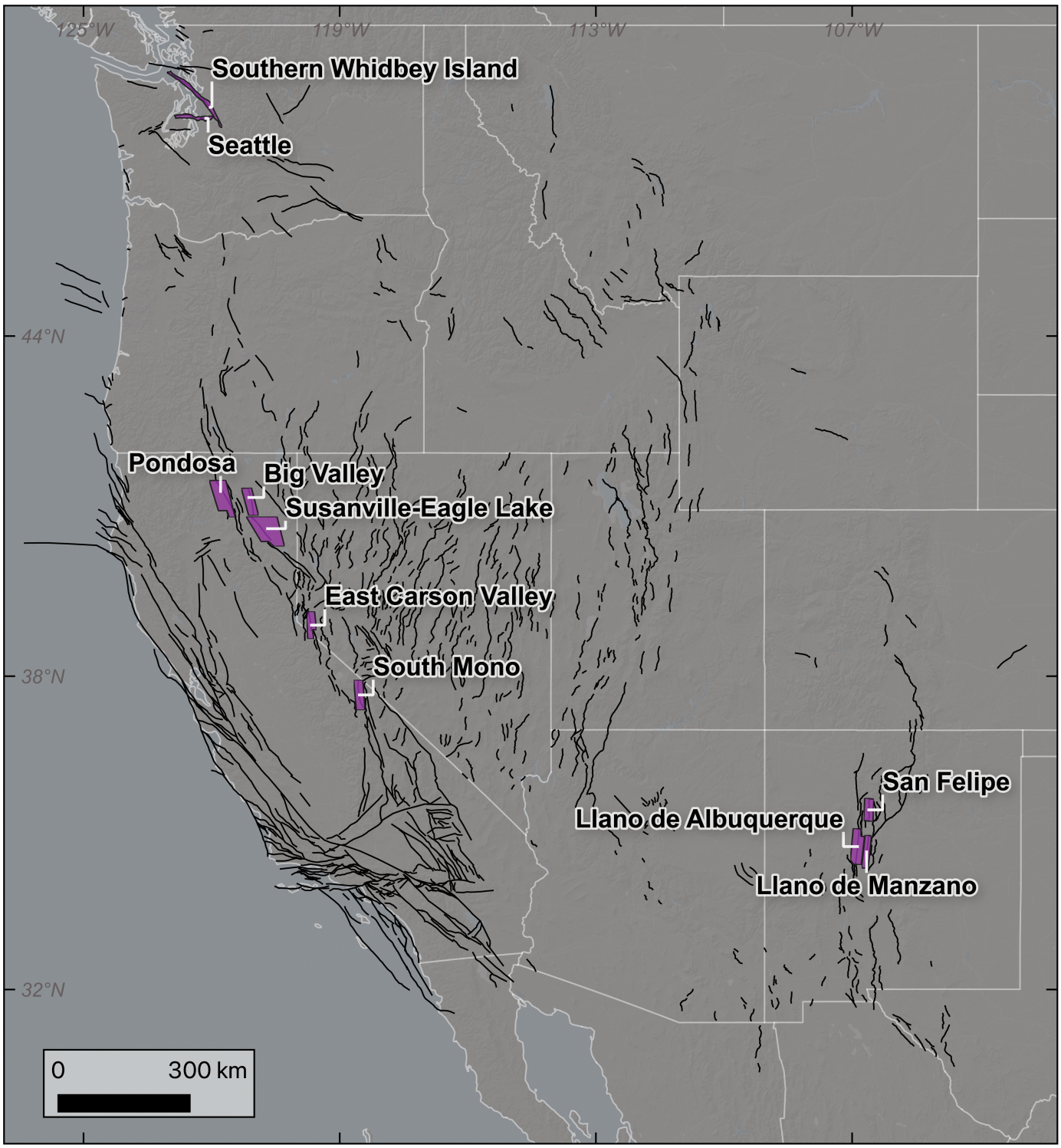

occur in this zone, especially if the polygon is large enough to accommodate them? Again, a rational alternative would be to model this with a GR distribution between M 6.5 and 7.25, and constrained so that the total rate of events implies a recurrence interval of 1333 yr; applying a b-value of 1.0 would make the $M \geq 6.5$ events feasible but relatively rare. In terms of hazard uncertainty quantification, it would also be good to reduce the number of logic tree branches for these sources to a common, necessary, sufficient, and manageable set as well.

Figure 12. Map of WUS fault zones (purple polygons) indicating where a clear predominant surface is lacking. From Hatem, Collett, *et al.* (2022). The color version of this figure is available only in the electronic edition.

WUS fault zone sources. The following WUS faults fall in this category as well (Hatem, Collett, *et al.*, 2022), broken out by state and shown in Figure 12:

1. Washington:

- Seattle
- Southern Whidbey Island

2. California:
   - Big Valley
   - Pondosa
   - South Mono
   - Susanville-Eagle Lake
3. Nevada:
   - East Carson Valley
4. New Mexico:
   - Llano de Albuquerque
   - Llano de Manzano
   - San Felipe

These zones of distributed deformation were also assigned proxy faults, the latter of which were used in both the deformation models and fault system solutions (treated the same as any other fault). Hazard tests show general insensitivity (less than a few percent) to whether a source is modeled as an explicit fault or a fault zone given the same MFD (rupture magnitudes and rates). The more consequential influence is whether these faults can co-rupture with neighbors, which is only currently supported when proxy faults are utilized. Thus, the "Classic" inversion-based solution should produce the same hazard as treating these as source zones, and sensitivity tests have found that removing these particular proxy faults from fault system inversions does not change implied hazard significantly (less than a few percent).

Gridded seismicity sources

Gridded seismicity or "background" sources represent the seismicity that is not captured by explicitly modeled faults. These are presently composed of (1) a polygon defining the region and a spatial discretization interval (0.1° here) to define the grid cells, (2) a spatial probability distribution defining the relative rate of earthquake nucleation within each grid cell, (3) a total $M \geq 5$ rate and b-value for the region, (4) an assumed maximum magnitude for the region, (5) a probability distribution of focal mechanisms for each grid cell, and (6) rules for converting a nucleation point into a finite rupture surface. Steps are also often taken to ensure that gridded seismicity sources are not double counted with fault-based sources. We develop these models separately for the WUS and CEUS collection regions shown in Figure 3, as well as for deeper events (>35 km) near the Cascadia subduction zone, which are processed separately.

Earthquake catalog updates. The WUS and CEUS earthquake catalogs have been updated through 2022 using the methodology of Mueller (2019) and are available as part of the NSHM 2023 data release (see Data and Resources). Important elements of this processing include the removal of duplicate earthquakes, explosions, mining-related events, and for CEUS, induced earthquakes based on an updated set of zones for such events. Network reported magnitudes are converted to uniform moment magnitudes, and bias corrections are made with respect to sampling events from a GR distribution. The final nondeclustered CEUS catalog contains 26,145 M 0.96–7.5 events since the year 1568, and that for WUS contains 60,214 M 3–9 events since the year 1700.

TABLE 6
Total $M \geq 5$ Rate (per yr), b-Value

Region	Mean	Mean–2σ	Mean + 2σ
WUS collection	12.0, 0.81	10.6, 0.91	13.5, 0.71
CEUS collection	0.45, 0.94	0.26, 1.1	0.75, 0.78
Deep Cascadia	0.23, 0.73	0.13, 0.93	0.41, 0.53

Total regional rate and b-value estimates. Following UCERF3, one improvement here is quantification of total $M \geq 5$ rate and b-value estimates for various regions, provided by Andrew Michael (USGS, written comm., 2023, referred to hereafter as Michael2023). More specifically, they provided three rate and b-value pairs, representing the mean and 95% confidence bounds, for the WUS and CEUS collection regions, as well as for the deep Cascadia seismicity (Table 6). The regional b-values were inferred using the recently developed "b-Positive" technique of van der Elst (2021), and total regional rates were inferred from a Monte Carlo sampling algorithm that accounts for uncertainties in b-value, spatially variable magnitudes of completeness, and individual event magnitudes.

For model comparison purposes, we apportioned these rates to analysis subregions (Fig. 3) using the branch-averaged spatial PDF, and uncertainties for the associated total $M \geq 5$ rate are expanded based on the square root of the implied data reduction. We refer to the result as the "observed" or "target" MFD for each region.

Gridded seismicity spatial PDFs. Inferring the long-term spatial probability density function of seismicity rates requires catalog declustering, otherwise rates will be biased high where larger events have produced aftershocks during our short observation period and biased low in areas that were randomly spared such events (e.g., Frankel, 1995). Lacking a perfect model for aftershock occurrence, a variety of catalog declustering algorithms have been developed. NSHM14/18 and other previous USGS models generally utilized the Gardner and Knopoff (1974) algorithm. A major improvement for 2023, as provided under the leadership of Andrea Llenos (USGS, written comm., 2023, referred to hereafter as Llenos2023), has been the addition of two other declustering algorithms as alternative logic tree branches: Reasenberg (1985), which was also utilized in previous Hawaii models (Klein *et al.*, 2001; Petersen *et al.*, 2021) and the nearest neighbor approach of Zaliapin and Ben-Zion (2020).

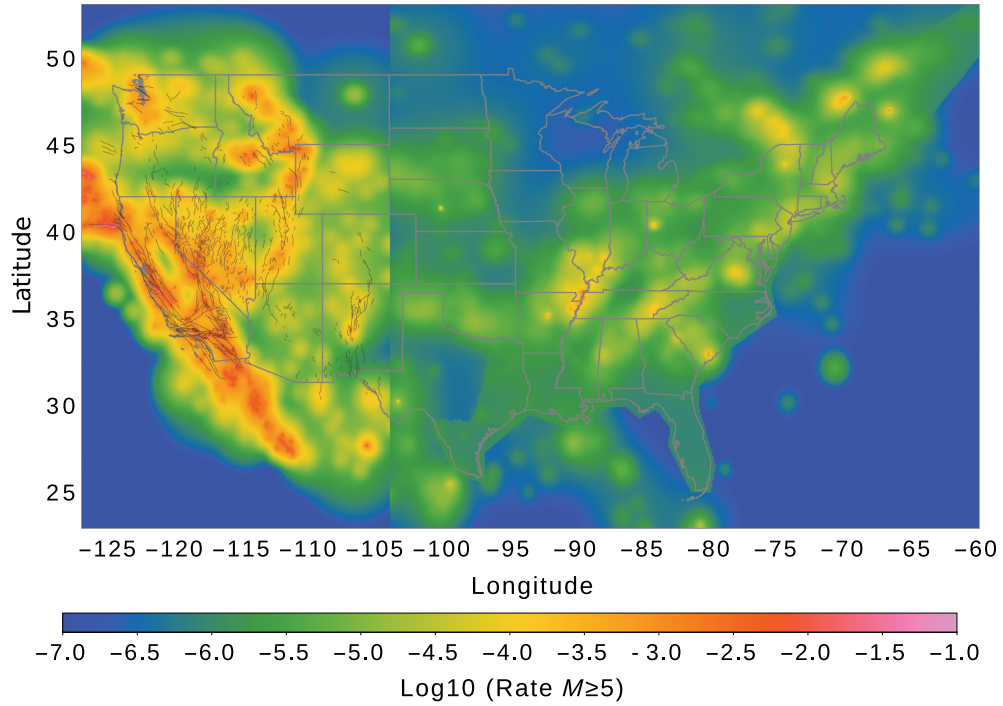

Figure 13. Branch-averaged $M \geq 5$ seismicity rate in 0.1° × 0.1° bins for the WUS and CEUS collection regions (defined in Fig. 3). The discontinuity at −104° longitude is the boundary between WUS and CEUS, which were processed independently. The color version of this figure is available only in the electronic edition.

For each declustered catalog, and considering various magnitude of completeness models, the number of events is tallied in each grid cell, and the result is spatially smoothed using the same two approaches utilized in NSHM14/18, both based on a 2D Gaussian kernel. One uses a fixed smoothing width as defined in equation (1) of Frankel (1995), with 50 km being applied in WUS and 50 or 75 km being applied in CEUS (depending on assumed minimum magnitude of completeness). The other is an adaptive smoothing width, which is defined by the distance to the Nth nearest earthquake (N is 3 and 4 in WUS and CEUS, respectively). In areas in which rates are unrealistically low using the fixed smoothing, floor rates are specified inside associated polygons; these persist in CEUS,

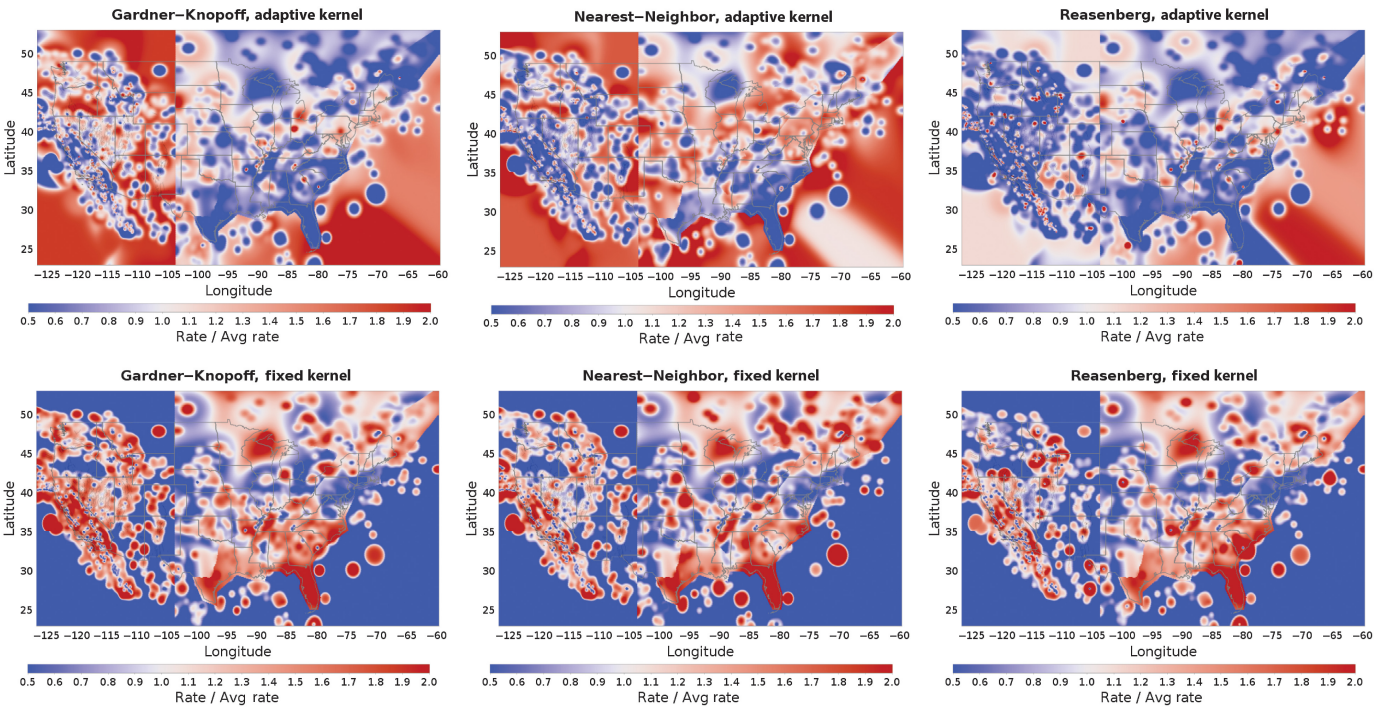

Figure 14. $M \geq 5$ seismicity rates for each Declustering and Smoothing Kernel branch combination normalized by the branch-averaged rates shown in Figure 13. The color version of this figure is available only in the electronic edition.

but those applied previously in WUS are no longer utilized (Llenos2023).

Each of the three declustering and two spatial smoothing algorithms were originally given equal weight. However, based on feedback from our review panel (Jordan *et al.*, 2023), Reasenberg declustering was downweighted, because it leaves several aftershock sequences still visible, and the fixed smoothing option was downweighted because it likely spreads seismicity too far, at least in some areas (refer to Fig. 2 for final branch weights). The branch-averaged smoothed seismicity map is shown in Figure 13, and the ratio of each branch to this average is shown in Figure 14. The discontinuity at longitude −104° W is a result of the different processing in each region. These results imply that differences between fixed and adaptive smoothing are generally greater than that between the different declustering algorithms. Llenos2023 also provided equivalent results for the deep seismicity near Cascadia, for which only the fixed smoothing option has been applied.

Maximum magnitudes, focal mechanisms, and finite rupture surfaces. Three branches are utilized for gridded seismicity maximum magnitude ($M_{\max}^{\text{off-fault}}$), with the options and weights for WUS being adopted from UCERF3 (Table 3, Fig. 2). The CEUS $M_{\max}^{\text{off-fault}}$ options are adopted from NSHM14/18 (four branch options in each seismotectonic zone defined in the 2014 model, with values ranging from M 6.5 to 8.0). The spatial distribution of relative focal mechanism likelihoods also remains unchanged compared with NSHM14/18. For example, ruptures in Pacific Northwest are assumed 50% strike slip and 50% reverse, ruptures in Intermountain West are assumed 50% strike slip and 50% normal, CEUS events are 100% strike slip, and the UCERF3 region has the spatial variability defined originally by Petersen *et al.* (2008). For the 2023 NSHM, a random strike is assumed, and rupture lengths are determined for $M \geq 6$ events using the Wells and Coppersmith (1994) magnitude–length relationship (for unknown rake).

Merging with other source models. In regions with numerous explicitly modeled faults, or perhaps near any individual fault, it can be important to avoid double counting earthquakes. In other words, the sum of the source model MFDs should be consistent with the total regional MFD estimate, and ensuring or testing this is precisely why we added total $M \geq 5$ rate and b-value estimates for the various subregions.

Each WUS fault system solution has an implied total MFD (for supraseismogenic on-fault events). Following UCERF3, we define the total gridded-seismicity MFD as the total regional target minus the total fault system solution MFD. More specifically, we construct a total target GR MFD from the regional b-value and the chosen total $M \geq 5$ rate branch, truncated at the chosen gridded seismicity $M_{\max}^{\text{off-fault}}$ branch; the gridded seismicity MFD is this target minus the total fault system solution MFD, for which any consequent negative values are set to zero (e.g., above $M_{\max}^{\text{off-fault}}$, or where the fault system solution MFD exceeds the regional target [the so-called bulge]).

We could apply this consequent gridded-seismicity MFD across the region according to the smoothed-seismicity spatial PDF (such that each grid cell has the same MFD shape). However, this might still be considered double counting near faults. Past models have avoided this by capping the maximum magnitude of gridded seismicity near faults to be just below the minimum magnitude on the associated fault. This is typically applied within 12 km of the fault trace (although this buffer was also dip dependent in UCERF3). The assumption is that the fault represents a proxy for all supraseismogenic magnitudes in that zone, and that gridded seismicity contributes no such events in this area.

This representation turned out to be problematic when adding a spatiotemporal clustering model to UCERF3 (Field *et al.*, 2017), because it implied unrealistic MFD shape transitions over the finer scales needed for such modeling. To produce a smoother transition between faults and gridded seismicity, we assume that fault nucleation rates decay linearly with distance out to some specified maximum distance (12 km here), and that gridded seismicity rates have the opposite linear trend near faults. This means that large gridded seismicity events can occur within 12 km of a fault, but with reduced rates that trend linearly toward zero at the fault surface. This linear partitioning is done in 3D, so dipping faults are handled more elegantly than in the past. The bookkeeping, which is achieved by subdividing grid cells into 3D "cubes," gets somewhat complicated due to variable supra-seismogenic minimum magnitudes across the fault system plus the fact that we account for the average depth dependence of earthquake nucleation (refer to Field *et al.*, 2017 for details).

There is no attempt to avoid double counting in CEUS, because gridded seismicity sources are relatively low and do not generally add much in the way of hazard (and if they did, then the fault-based sources might not be value added).

WUS RESULTS (EXCLUDING CASCADIA)

Each WUS logic tree branch has 582,004 fault-based ruptures. There are 2250 different branches for the fault system solutions and 121,500 total branches when the latter are combined with the set of gridded seismicity options. We therefore must resort to aggregate metrics when interpreting results. To this end, an extensive set of web-based "solution reports" have been created and made available (a link to which is provided in Data and Resources). These solution reports include results for the following:

- full logic tree solutions,
- branch-specific solutions (sensitivity tests),
- hazard maps (and comparisons with NSHM14/18), and
- hazard curves at sites (and comparisons with NSHM14/18).

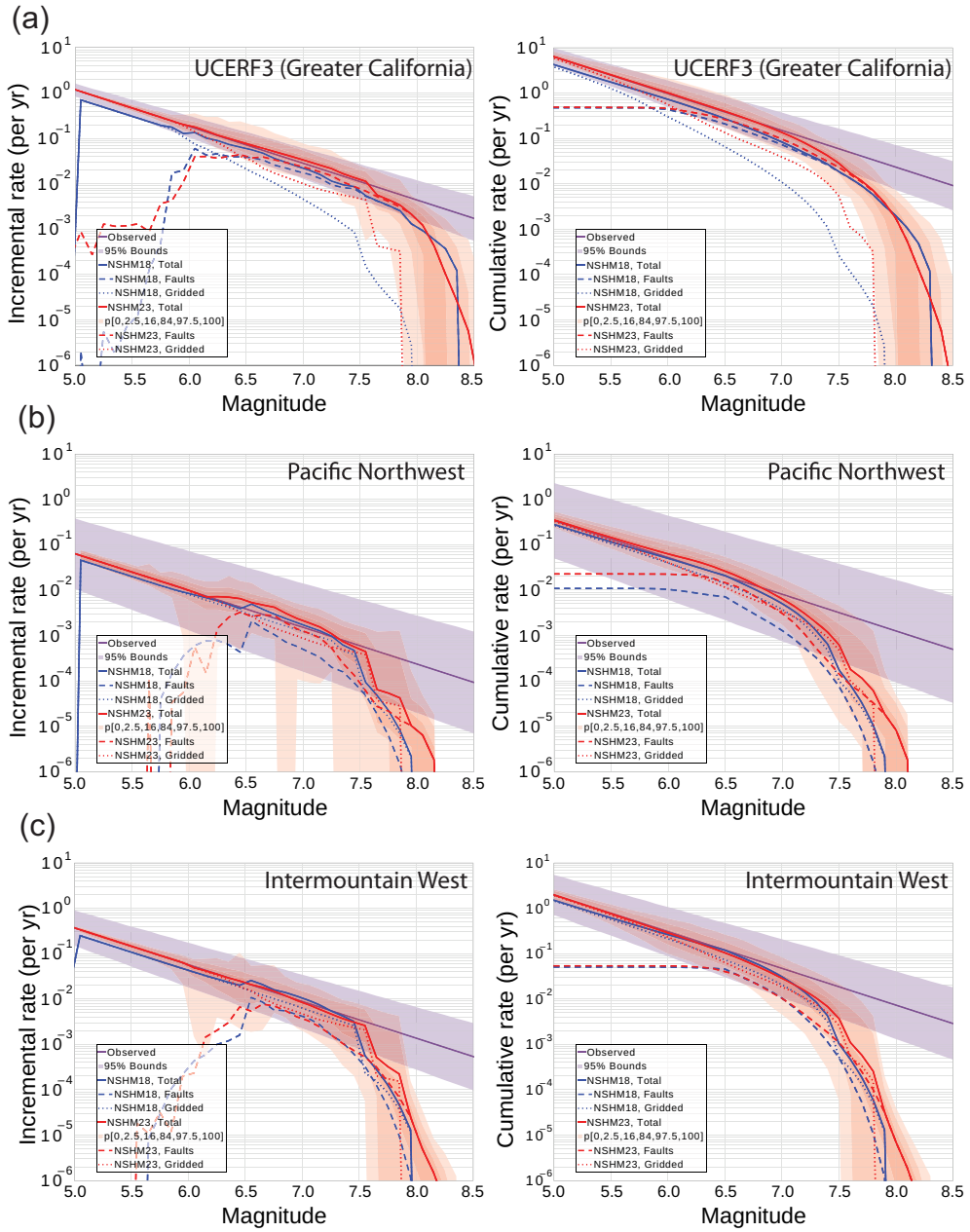

Figure 15. Model and target magnitude–frequency distributions (MFDs) for the three analysis regions in WUS: (a) UCERF3 (Greater California), (b) Pacific Northwest, and (c) Intermountain West. Blue and red curves are for the National Seismic Hazard Model (NSHM14/18) and new model, respectively. Solid curves are for the complete model; dashed curves are for faults; and dotted curves are for gridded seismicity. The red shaded areas represent various epistemic uncertainty percentiles, as labeled, for the new model. The purple line and shaded region represent the observed target and 95% confidence intervals, respectively, for each region (extrapolated from M 5 with no taper). The color version of this figure is available only in the electronic edition.

These reports embody an immense number of plots and diagnostics (virtually everything that has been envisioned and requested during analysis and review, plus this is a living archive in which things can be added upon request). We focus on a relatively small but representative subset of results here.

Model fits to data constraints

Here, we summarize how well the WUS models fit the data. It is important to recognize that, given the wide range of constraints (Table 3), it is not possible to fit all data perfectly due to potential incompatibilities. For example, a paleoseismic recurrence interval may be physically incompatible with an assigned slip rate, or spatial variability of slip rate in the system may be incompatible with the target nucleation MFD on a fault section. This means that scatter is expected between target constraints and those implied by final models. This scatter is not due to limited simulated annealing runtime (we confirmed that longer runs do not further reduce misfits). Milner and Field (2023) provide sensitivity tests on this and other potentially important inversion attributes.

Regional MFDs. The observed target and model implied cumulative MFDs for the three WUS analysis regions are shown in Figure 15, including the contributions from faults (dashed), gridded seismicity (dotted), and the combined total (solid). Comparisons with NSHM14/18-implied MFDs are also shown with blue lines. For the UCERF (Greater California) region (Fig. 15a), the mean rate of $M \geq 5$ events implied by the new model is 6.38 per year, in agreement with the new branch-average target of 6.30, but this is a factor of 1.5 greater than that of NSHM14/18 (4.26 events per year). This discrepancy is seemingly inconsistent with the fact that the total branch-averaged $M \geq 5$ rate dropped from 8.26 in UCERF3 to 6.38 here. However, the NSHM14/18 rates in Figure 15a also reflect a declustered model, which effectively reduced the $M \geq 5$

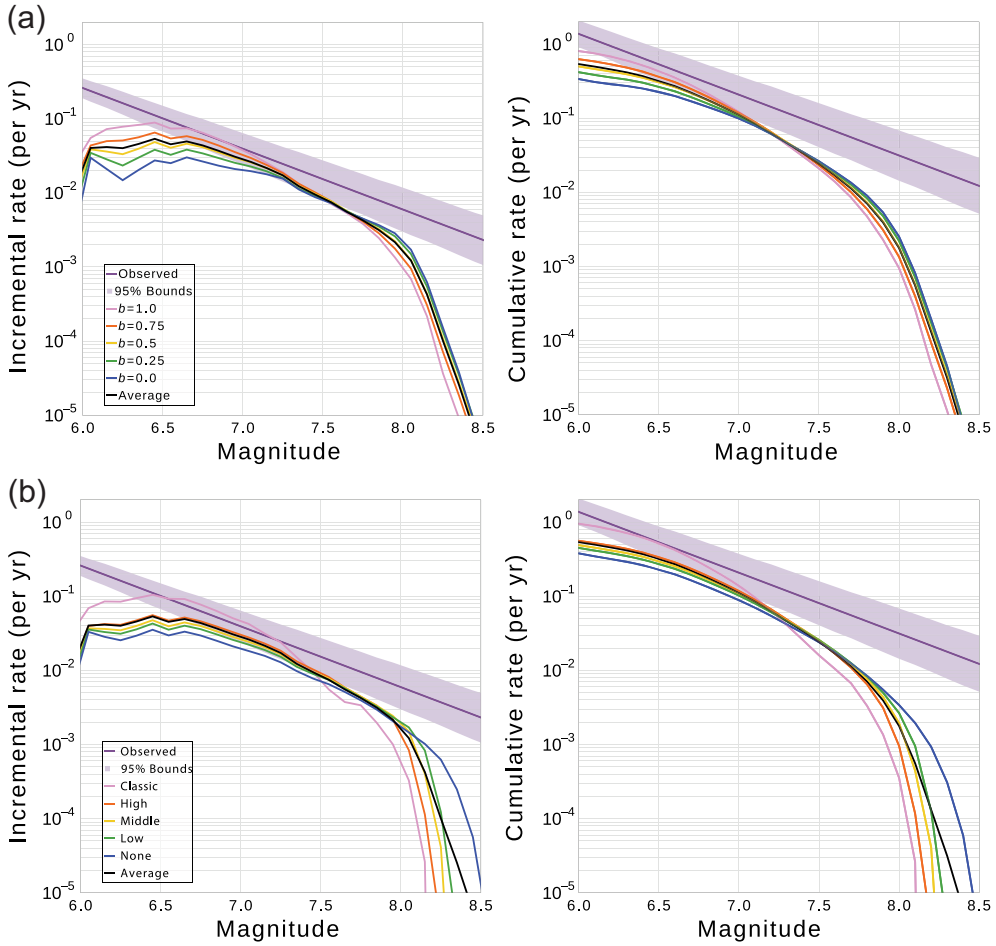

Figure 16. Average WUS fault system solution MFDs for (a) *b*-value branches and (b) segmentation branches. The full logic tree branch average is shown with the black line. The color version of this figure is available only in the electronic edition.

rates in NSHM14/18 by a factor of 1.9 (compared with the unclustered mean UCERF3 rate). In other words, most of the change in the $M \geq 5$ rate comes from the inclusion of aftershocks, which also explains why the NSHM14/18 value is near the lower 95% confidence bound of the new model. This difference does not necessarily propagate proportionately to larger magnitudes, because the total target *b*-value has also changed (from 1.0 in UCERF3 to 0.9 here); plus the NSHM14/18 declustering also created a magnitude-dependent *b*-value below *M* 6.5. The rate of $M \geq 7.5$ gridded seismicity events has increased by about an order of magnitude, owing to an increase in overall rate, a lowering of the regional target *b*-value, and changes in how the on- versus off-fault seismicity is defined (e.g., the new model essentially assumes zero MFD rolloff up to the maximum magnitude for gridded seismicity). Changes in fault-based supraseismogenic rupture rates are relatively small (<35%). The red shaded areas in Figure 15a show the range of total MFDs spanned by the new logic tree branches (for various percentiles, as labeled), the spread of which mimics, as expected, the observed rate uncertainties at lower magnitudes, but with some small fraction of models falling outside the observed 95% confidence bounds at intermediate magnitudes. MFD plots showing the epistemic uncertainties for faults and gridded seismicity, separately, are available in the solution reports (links 1 and 2 in Data and Resources). These reveal that gridded seismicity rates can be quite low or even zero at intermediate magnitudes on some branches. This occurs when fault system solutions approach or exceed the target MFD, producing a final total MFD that overshoots the target by the amount of exceedance (because gridded seismicity rates cannot be negative). As demonstrated subsequently, this is a problem with the more segmented and higher *b*-value fault system solutions. The extent to which consequent gridded seismicity rates are inconsistent with observed "off-fault" events could be used as a basis for downweighting such models (something we have not yet explored).

MFDs for the Pacific Northwest region are shown in Figure 15b. The new model matches the target $M \geq 5$ rate of 0.34 events per year and exceeds the NSHM14/18 value of 0.28 by 21%. The contribution from faults has increased since NSHM14/18, which is consistent with faults having been added. The new total average MFD exceeds the target by more than 30% and up to ~70% between *M* 6.3 and 7.1, which we will see is more of a problem with the more segmented models, but results are well within the confidence bounds. MFDs for the Intermountain West region are shown in Figure 15c. Total $M \geq 5$ rates have increased from 1.5 to 2.0 events per year since the NSHM14/18 model. Changes are otherwise relatively small for both faults and gridded seismicity. The solution reports include data files for extracting numerical values plus equivalent results for logic tree subsets and for smaller regions near Los Angeles, San Francisco, the Puget Lowland, and the New Madrid seismic zone (green rectangles in Fig. 3).

Figure 16a shows the influence of supraseismogenic *b*-value branches on average fault system solution MFDs for the entire WUS, and Figure 16b shows the same for the

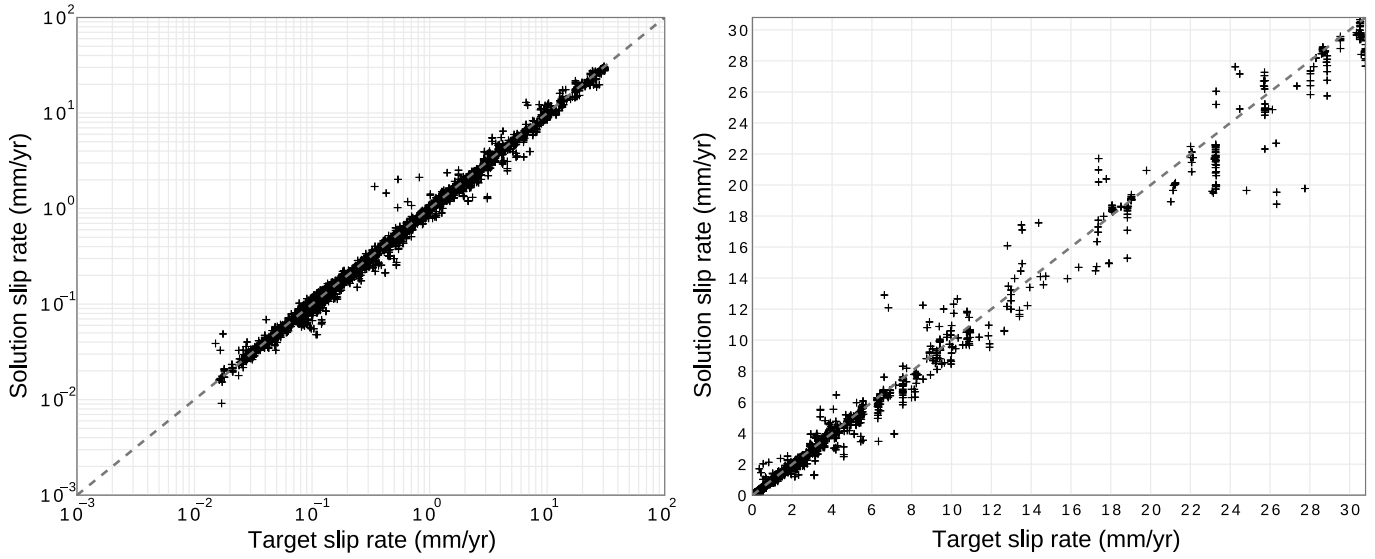

Figure 17. Branch-averaged solution slip rate for each subsection versus the average target value (the average deformation model slip rate including creep reductions), shown in both log and linear plots.

segmentation branches. Both plots exhibit expected behavior (higher rates at lower magnitudes for more segmented and higher *b*-value branches, and vice versa at higher magnitudes). This indicates that these inversion constraints are working exactly as intended, at least on average throughout the system. The *b*-value = 0 branch produces, when all combined, a *b*-value of about 0.8 between *M* 6.5 and 8.0, which is due to variable maximum magnitudes and slip rates throughout the system, as well as the segmentation constraints. In addition, the classic segmentation model has the highest rates at $M \leq 7.3$ and is somewhat of an outlier (e.g., in terms of pulling the overall mean MFD above the middle segmentation result and making it just under high segmentation). Consequently, this is also the most problematic branch in terms of producing fault-system MFDs that approach or exceed the regional target, which again leads to low gridded seismicity rates at intermediate magnitudes and perhaps an MFD over prediction.

Slip rates. Figure 17 shows a scatter plot of mean solution slip rates versus the mean target value for all 5572 fault subsections. Again, this reveals that the inversion is working properly, with discrepancies reflecting inconsistency with other constraints (specific examples are discussed in the next section). A map view of these misfits and a variety of other slip-rate plots are available in the solution reports (e.g., link 3 in Data and Resources for branch-averaged model).

Although each deformation model generally provided slip-rate uncertainty estimates, these were not used to weight the inversion for several reasons. One is that it is not clear exactly what these uncertainties represent (just data misfits or also some representation of any null space?), especially in the absence of covariance estimates. It is also not clear whether uncertainties were handled consistently between models. A more practical reason is that in areas with high uncertainties (relative to slip rates, like in the Intermountain West), the inversion will tend to over- or underfit all slip rates, and such a systematic bias is unlikely to be correct (and violates likely correlation between neighboring slip rates). Consequently, we cap uncertainties at 10% (one sigma values) as noted earlier, meaning we generally overfit the slip-rate data. This issue was discussed originally in Field *et al.* (2020) and more recently in the context of this model in Milner and Field (2023). The latter also has a more detailed discussion solution misfits (including *z*-scores with respect to the original slip rate uncertainty estimates; their table 3).

Paleo event rates. A scatter plot depicting paleoseismic event-rate misfits is shown in Figure 18a for the branch-averaged model, as well as for the underfit and overfit paleoseismic data fit branches (Fig. 18b,c, respectively; the result for the even-fit branch is similar the branch-averaged plot). As expected, the scatter is the greatest for the underfit branch and the smallest for the overfit branch. Figure 18 also shows scatter plots of associated slip rates (at collocated fault subsections), which clearly reveal the trade-off in fits between paleoseismic event rates and slip rates (e.g., slip rates are fit best when paleoseismic data are underfit). Perhaps most importantly, Figure 18 indicates where the two types of data constraints are incompatible. For example, two paleosites on the Wasatch fault (Alpine and Corner Canyon) are never fit within the 95% confidence bounds, even on the overfit branch. Similarly, the slip rate at the Green Valley Mason Road site is never fit within the 95% confidence bounds either. With respect to the branch-averaged model, other sites outside the 95% bounds include Little-Salmon-Strongs and four additional Wasatch sites with respect to paleo event rates, and the

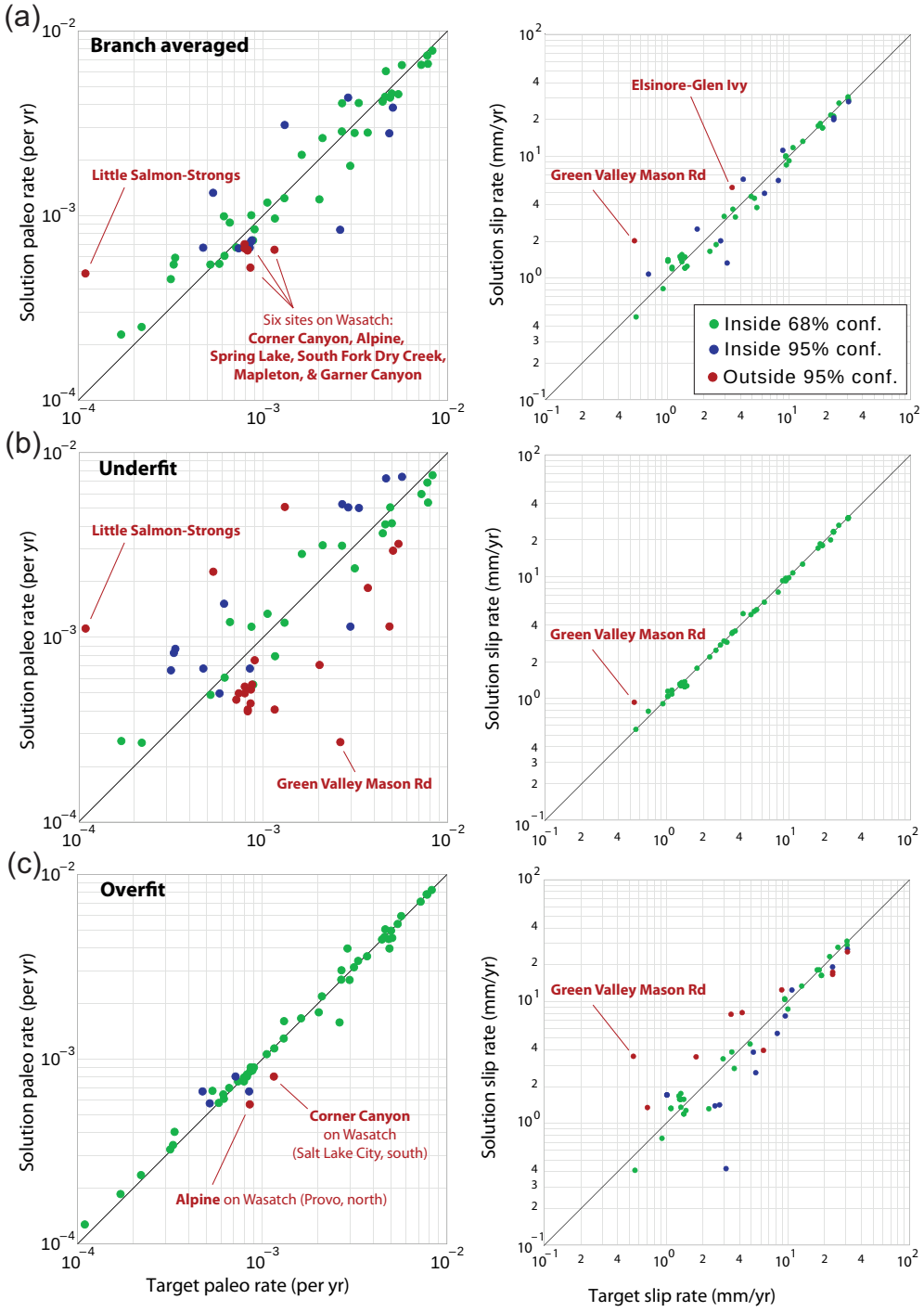

Figure 18. WUS paleoseismic data fits (solution vs. target rate) shown on the left with associated slip-rate fits (at the associated subsection) shown on the right. Results for the (a) branch-averaged model, (b) under-fit paleoseismic data fit branch, and (c) over-fit branch. The even-fit result, not shown, is similar to that of branch averaged. Symbol colors indicate for which solution values land with respect to 68% and 95% confidence bounds (see legend in top right panel). The paleosites for some values that are outside the 95% confidence bounds are labeled. The color version of this figure is available only in the electronic edition.

Elsinore-Glen Ivy site with respect to slip rate. These sites warrant further scrutiny in the future studies. Map views of the misfits shown in Figure 18a, as well as tabulated values for each paleoseismic site, are provided in the solution reports (e.g., link 4 in Data and Resources for branch-averaged solution); also available are fault-specific misfits plots, including along fault trends, for all parent fault sections and for the special faults defined in Table 5.

Fits to other inversion constraints

Supraseismogenic *b*-values. Recall that the supraseismogenic *b*-value constraint is simply a mechanism to sweep over a range of viable models (between the minimum and maximum rate models), and we use it to compute a total nucleation rate constraint for each fault subsection. The logic tree defines target supraseismogenic *b*-values between 0 and 1 with uniform weights (Fig. 2). These get modified for consistency with the chosen segmentation model, as discussed earlier, which generally increases the target *b*-value due to the consequent MFD rolloff at higher magnitudes. Furthermore, the ability of the inversion to match target values depends on other factors, including nearby paleoseismic event-rate constraints and slip-rate heterogeneity (e.g., a greater proportion of smaller events will be needed where slip rates vary over smaller spatial scales). All of this produces substantial variability among post-inversion supraseismogenic *b*-values among subsections, making their evaluation complicated. We already saw from Figure 16a that, on average over the system, these *b*-values constraints are having the intended effect, but are there individual faults in which this is not the case? Because the whole point of this constraint is to vary the total rate of events on each fault, we check for this by comparing average fault participation rates among these branches (participation indicates the frequency at

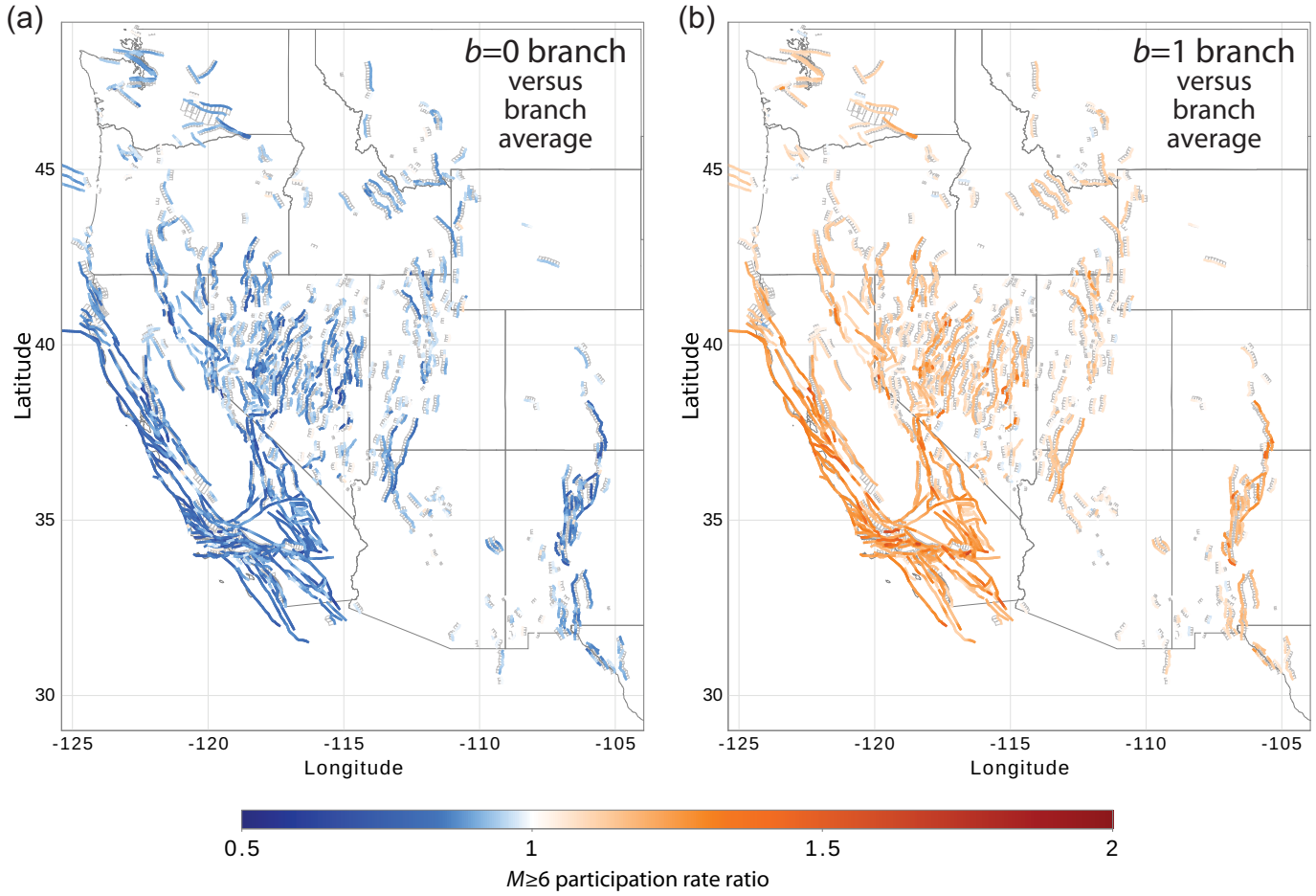

Figure 19. Average $M \geq 6$ fault participation rates for the two extreme supra-seismogenic *b*-value branches (0.0 in panel a vs. 1.0 in panel b), both normalized with respect to values from the full logic tree. This demonstrates that this constraint is systematically dialing over a range of total rates. The color version of this figure is available only in the electronic edition.

which events pass by a point on a fault, even if the events nucleated some distance away). To this end, Figure 19a shows $M \geq 6$ fault participation rates for the *b*-value = 0 branch, and Figure 19b shows those for the *b*-value = 1 branch, both normalized by equivalent average rates from the full branch-averaged logic tree. As intended, the $M \geq 6$ participation rates for *b*-value = 0 are lower than average across the region, and those for *b*-value = 1 are relatively high, and the reverse occurs at higher ($M \geq 7.5$) magnitudes (which must be true because moment is balanced). This gives us confidence that this constraint is indeed allowing us to map out a wider range of models than considered in the UCERF3 inversion.

Segmentation constraints. The distance dependence of segmentation (i.e., the relative passthrough rate among neighboring faults as a function of separation) is shown in Figure 20 for the branch-averaged model as well as for each segmentation branch. The smaller circles in each plot are values for each connection between faults in the fault system, the larger circles are mean values as a function of distance, and larger squares are median values. Recall that this is an inequality constraint, such that all passthrough rates must fall below the target line for the low, mid, and high branches (and mean results are consequently below the lines as well, but with about the same distance trend as the target). As expected, the no segmentation (*None*) branch shows almost no trend with distance, and the *Classic* branch shows relatively few connections (only within the special faults defined in Table 5). Again, these plots give us confidence that the inversion is working as intended.

The solution reports contain a variety of other plots relating to segmentation, including a map view of fractional passthrough rates (e.g., link 5 in Data and Resources for branch averaged solution). The pages for each parent fault section also include a map showing the frequency of co-ruptures with neighboring faults, as well as examples of individual ruptures for a range of likelihoods including the most extreme case (e.g., links 6 and 7 in Data and Resources for the Cucamonga fault).

Fits to data not used in the inversion

Figure 21 shows how the cumulative frequency distribution of rupture length implied by the model compares with the Wells and Youngs (2013) global compilation of 258 observed earthquakes (curves have been normalized for comparison purposes). For the nonclassic models, the agreement for WUS (Fig. 21a) is

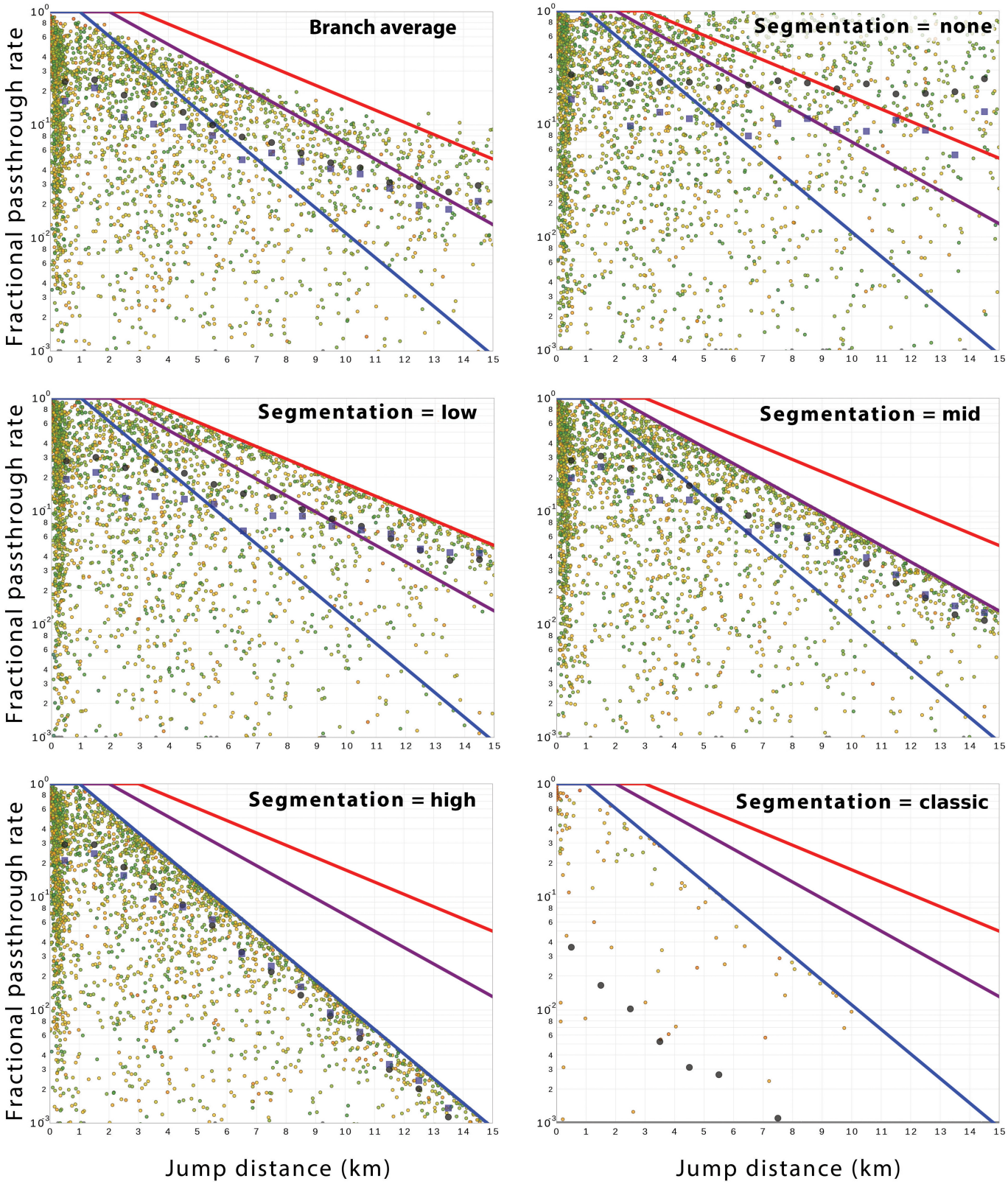

Figure 20. Fractional passthrough rates at each WUS fault connection (small circles) as a function of distance for each segmentation branch as labeled. Solid lines represent the upper bounds for the low (red), middle (purple), and high (blue) segmentation branches. Large circles and squares represent average and median values, respectively, for 1 km distance bins. The color version of this figure is available only in the electronic edition.

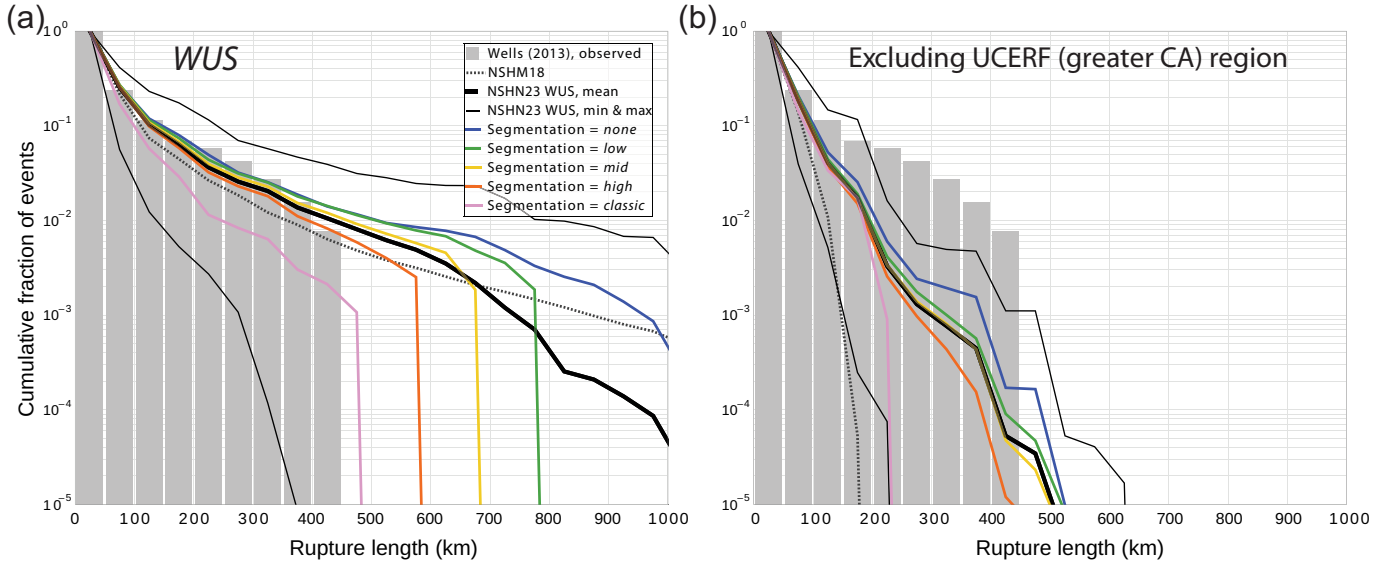

Figure 21. Cumulative distribution of rupture lengths for the full model (thick black line) and for the different segmentation branches (colored lines as labeled), normalized by total rate. Gray histograms represent the global data compilation of Wells and Youngs (2013), also normalized. (a) WUS and (b) excludes ruptures in the UCERF (Greater California) region. The color version of this figure is available only in the electronic edition.

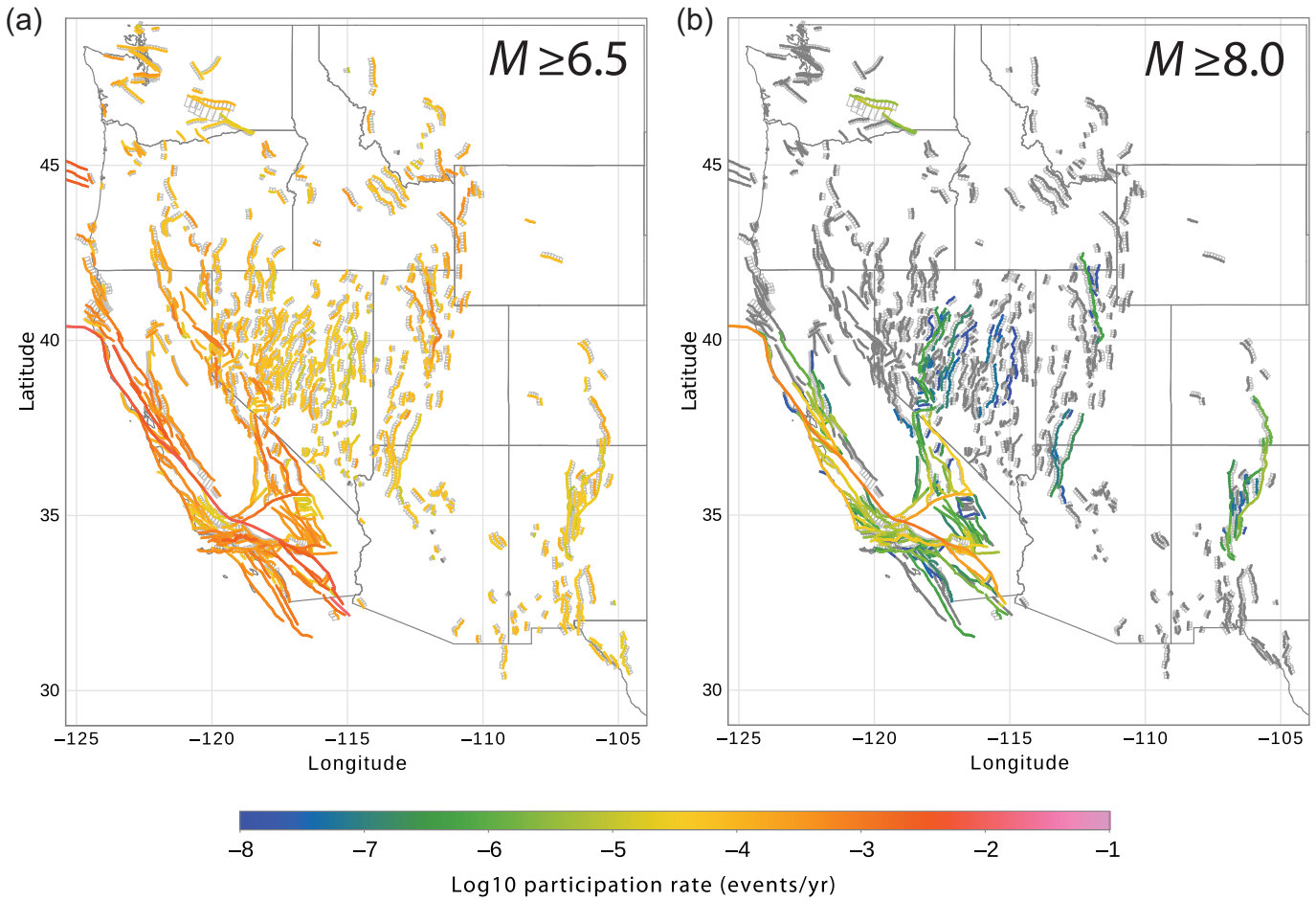

Figure 22. WUS branch-averaged fault participation rates for (a) $M \geq 6.5$ and (b) $M \geq 8.0$ earthquakes. Gray color indicates a rate of zero. The color version of this figure is available only in the electronic edition.

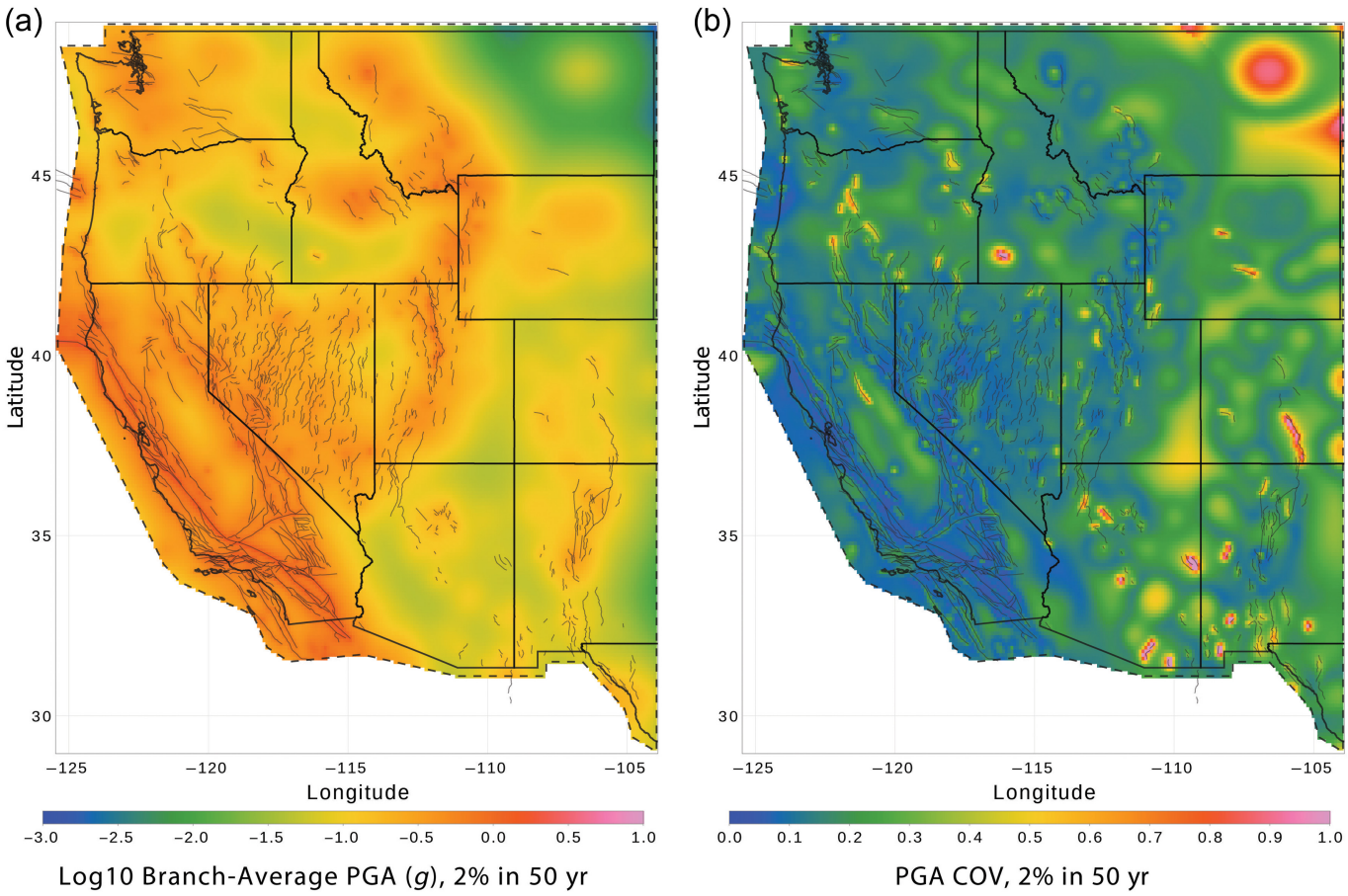

Figure 23. (a) The peak ground acceleration (PGA) that has a 2% chance of exceedance in 50 yr according to the new WUS branch-averaged model (computed using the Abrahamson *et al.*, 2014 ground-motion model (GMM) with $V_{S30} = 760$ m/s). (b) The coefficient of variation (COV) implied by the full logic tree. The color version of this figure is available only in the electronic edition.

quite good up to about 450 km, beyond which there is a discrepancy due to a lack of observation of such events. The latter implies there might be a physical upper bound on rupture length, which would be an easy constraint to add to the model. Figure 21b shows the same result, except that California ruptures are excluded, revealing a steeper trend.

Two salient questions are whether the Wells and Youngs (2013) data set represents an unbiased global sample and whether it is applicable to WUS. Another question is whether the lack of observations above 450 km is a sampling issue with respect to rare events; in other words, can we reject our model by demonstrating that it implies a significant probability of having seen such an event by now? Until these questions can be adequately addressed, it seems prudent to avoid over interpreting the match implied by Figure 21a. One question we can address is the fraction of super long ruptures (e.g., ≥ 700 km) that traverse the creeping section of San Andreas fault; the answer is 72% for the branch-averaged model (thick black line), meaning 28% take a different path (but all are within the UCERF region).

We also endeavored to utilize the detailed surface rupture observations and statistical analyses of Biasi and Wesnousky (2016, 2017). For example, they found for strike-slip faults that "steps of 1 km or greater will be effective in stopping rupture about 46% of the time" (Biasi and Wesnousky, 2016, p. 1110). However, these are based on fresh, high-resolution surface-rupture maps (obtained soon after large events and before substantial erosion); therefore, it is not obvious how to compare these to our highly simplified fault representations. In other words, if any one of the fault ruptures in our model was to occur, we do not expect surface rupture features to look anything like our simplified fault traces. Furthermore, it is not clear what these surface features tell us about rupture connectivity at depth (where the dynamics play out). We have, therefore, thus far, been unsuccessful in utilizing the Biasi and Wesnousky (2016, 2017) studies to evaluate our model, but future efforts may be more fruitful.

Hazard-related metrics

This section discussed the implications of the model in terms of various hazard-related metrics.

Fault section participation MFDs. Hazard at a site is often dominated by one or more nearby faults, so a particularly relevant metric is the participation MFD, which quantifies the rate at which ruptures involve (or pass by) each fault section,

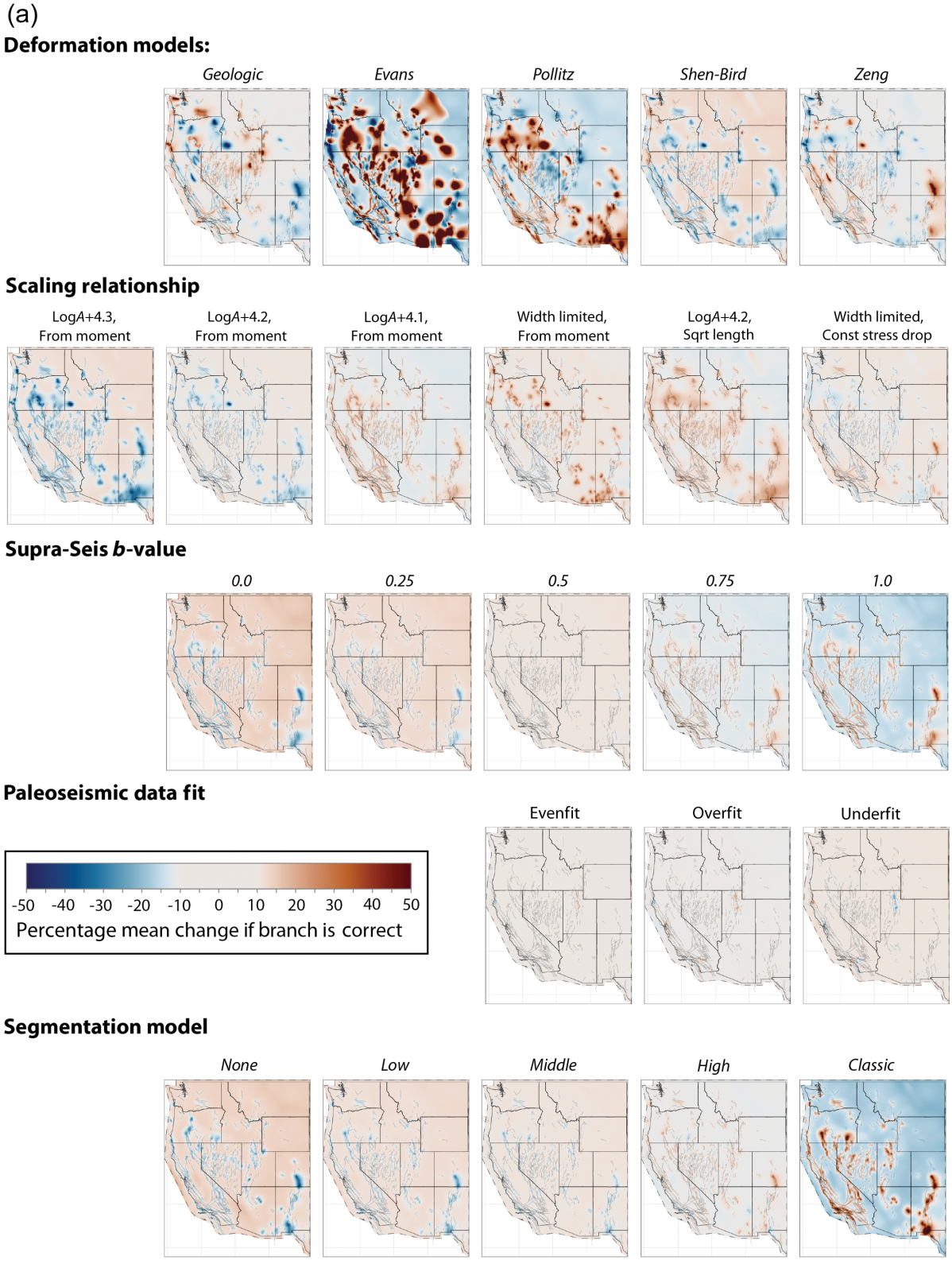

Figure 24. The percent change for the map in Figure 23a (the PGA that has a 2% chance of being exceeded in 50 yr), if each branch choice is found to be correct (others branch options removed). Branch options are shown in Figure 2. The color version of this figure is available only in the electronic edition. (*Continued*)

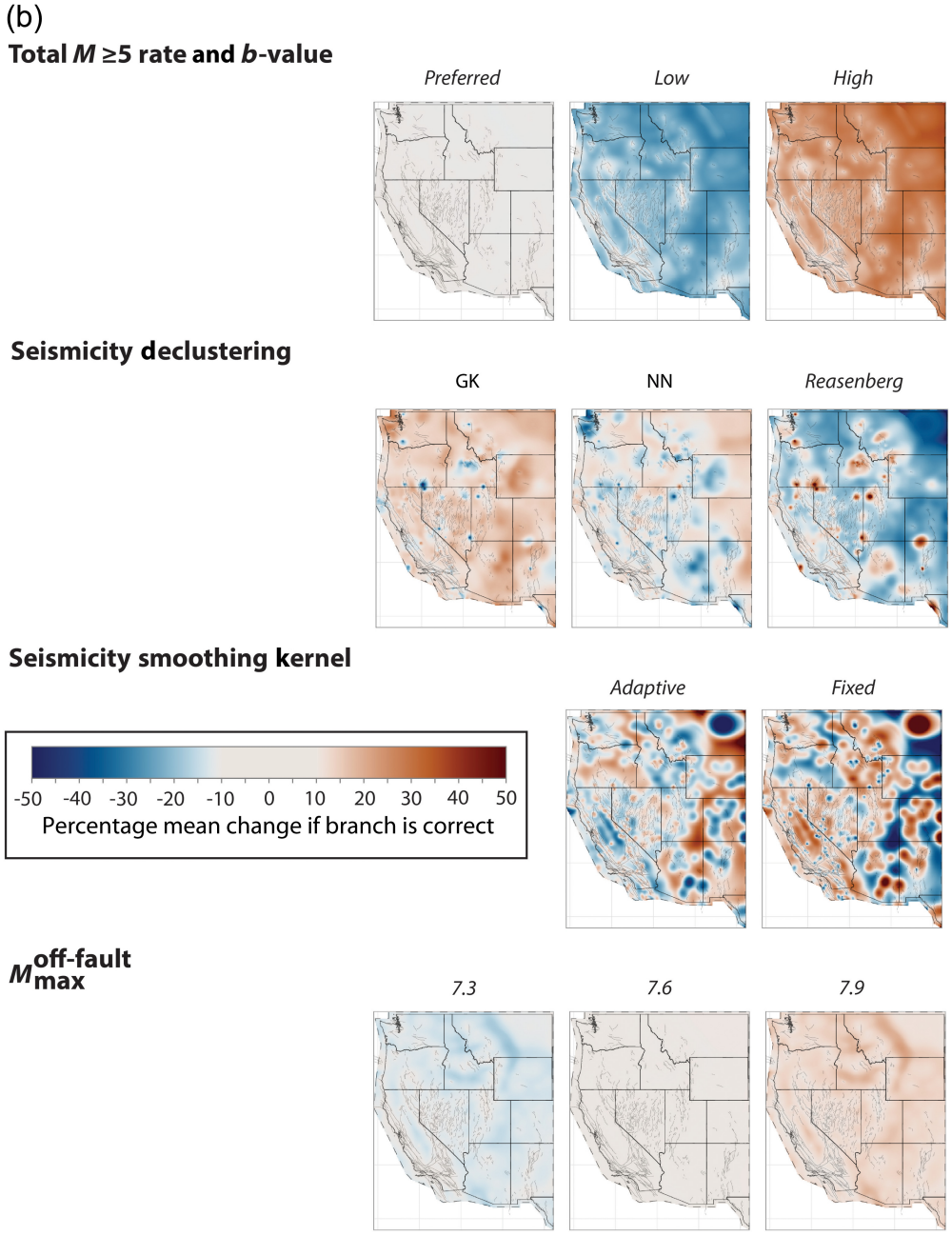

Figure 24. Continued

even if they nucleate elsewhere. It is not practical to look at the participation MFDs for all 5572 fault subsections, so we take two approaches here. One is to plot subsection participation rates above a specified magnitude threshold in map view, examples of which are shown in Figure 22 for $M \geq 6.5$ and $M \geq 8$ events in the branch-averaged model. The $M \geq 6.5$ participation rates are a pretty good proxy of the hazard posed by each fault, particularly in a relative sense. The plot for $M \geq 8$ reveals which faults participate in these more extreme events and at what frequency; for example, the Wasatch fault is expected to have an $M \geq 8$ event every ~1 million years. Participation rate maps for other thresholds are available in the solution reports (link 8 in Data and Resources for the branch-averaged model).

The other approach taken here is to aggregate MFD results for the 5572 fault subsections back onto the 1016 parent fault sections, which also aids in making meaningful comparisons to previous models. These participation MFDs, as well as nucleation MFDs and incremental and cumulative versions of each, are included for each parent fault section in the solution

reports (link 9 in Data and Resources for the branch-averaged model). For example, the participation MFD for the Wasatch (Salt Lake City, north) fault section (link 10 in Data and Resources) can be used to confirm the ~1 million yr recurrence interval for $M \geq 8$ events plus the range of values implied by epistemic uncertainties; such aggregate plots are also available for the special faults listed in Table 5 (link 11 in Data and Resources for the branch-averaged model).

Hazard maps and sensitivities. Figure 23a shows a map of the peak ground acceleration (PGA) that has a 2% chance of being exceeded in 50 yr, abbreviated as 2in50 hereafter, and we may refer to these as "hazard maps" even though they really represent a ground motion at a particular hazard level. The WUS hazard calculations presented in this section utilize the Abrahamson *et al.* (2014) GMM with default site parameters (e.g., $V_{S30} = 760$ m/s), although test calculations indicate that this choice has no effect on our overall conclusions. Hazard comparisons with the NSHM14/18 model are presented and discussed in the 2018–2023 hazard changes section. The point here is to illustrate sensitivity with respect to WUS model choices. To this end, Figure 24 shows the influence of each logic tree branch or, more specifically, how the mean hazard map would change if each branch choice was proven correct (and all others zeroed out). Keep in mind that this ignores branch weights. For example, the Evans deformation model may not only imply large changes in hazard, but it also has a relatively low likelihood of being correct (a weight of 2%). With this caveat in mind, the deformation models generally have the biggest influence on hazard near faults (Fig. 24a). The next most influential uncertainty is the segmentation model, with the *Classic* branch implying the greatest hazard near faults (higher frequency of events due to lower maximum magnitudes) and lower hazard away from faults due to fewer events available to gridded seismicity (to honor the total regional MFD target); the opposite is true for the other extreme segmentation branch (*None*). The supraseismogenic *b*-value and scaling relationship branches are also influential, at least, in some areas. The paleoseismic data fit appears to be the least influential, which is expected in that it is only relevant where such constraints are incompatible with slip rates (as exemplified earlier), and such areas are harder to discern in broader-scale maps.

Figure 24b shows the influence of the various gridded seismicity logic tree branches. The rank of overall impact, going from most to least influential, is generally the seismicity smoothing kernel, the seismicity declustering, the regional total $M \geq 5$ rate and *b*-value, and $M_{\max}^{\text{off-fault}}$.

Figure 23b shows the coefficient of variation (COV) implied by all epistemic uncertainties (the standard deviation divided by the mean). The minimum value is 0.035 at a site near San Francisco, California. If a Gaussian distribution is applicable, the 95% confidence bounds are about 1 ± 2COV, or ~7% above and below the mean for this site. The highest COV is 1.7 (in eastern Arizona at latitude and longitude of 34.3 and −109.3, respectively), which is above the color-scale saturation in Figure 23b (COV ≥ 1 is magenta); the Gaussian approximation obviously fails for such cases, given 2in50 PGA cannot be negative.

The results presented here are for only one hazard metric (2in50 PGA). Results for 1 Hz spectral acceleration, as well as for 2%, 10%, and 40% in 50 yr probability levels, are available in the solution reports (although the 40% in 50 yr values warrant careful consideration given the full catalog and Poisson assumption). Hazard curves, including thorough epistemic uncertainty analyses, are also available for a number of sites (link 12 in Data and Resources). It is important to emphasize that the inferences described here, including the relative influence of various epistemic uncertainties, will certainly vary among different hazard and risk metrics. The goal here has not been an exhaustive investigation with respect to all potential model uses, but rather to demonstrate that model makes sense with respect to one commonly used metric, especially with respect to branch sensitivities, and to showcase how the solution can be used for further investigations. It is probably best to assume that each logic tree branch could be most influential at some location, or for some other hazard or risk metric, meaning it is premature to start trimming branches at this point.

CEUS AND CASCADIA RESULTS

Although we endeavor to apply more uniform methodologies in all regions, updates in CEUS and Cascadia have been more modest, which means our level of model interrogation is more limited as well. The logic tree branches for CEUS-gridded seismicity are identical to those in WUS (the bottom half of Fig. 2). For CEUS faults and area sources, however, the logic trees are highly variable and are therefore not reproduced here. Most are unchanged since NSHM14/18 and are therefore available in Petersen *et al.* (2014), and uncertainties for the new sources were developed by Shumway2023. The new logic tree for Cascadia was developed by PowersCascadia2023.

Given this logic tree heterogeneity, as well as unspecified correlation structure between nearby sources, we have not been able to conduct the type of branch sensitivity analyses shown in Figure 24. Doing so would require redefining these sources to have a more common, minimum, necessary, and sufficient set of branches, as mentioned in the CEUS fault sources section, or the ability to handle Monte Carlo sampling of logic trees. Both the options are planned to be pursued in the future.

One thing we can plot are the model implied MFDs. Those for CEUS are shown in Figure 25a, revealing a total $M \geq 5$ event rate of 0.32 and 0.35 per year for the target and model average, respectively, up from 0.23 in NSHM14/18, which is consistent with the new model now including aftershocks. The regional *b*-value is relatively unchanged because the rate change for gridded seismicity is weakly dependent on magnitude. As

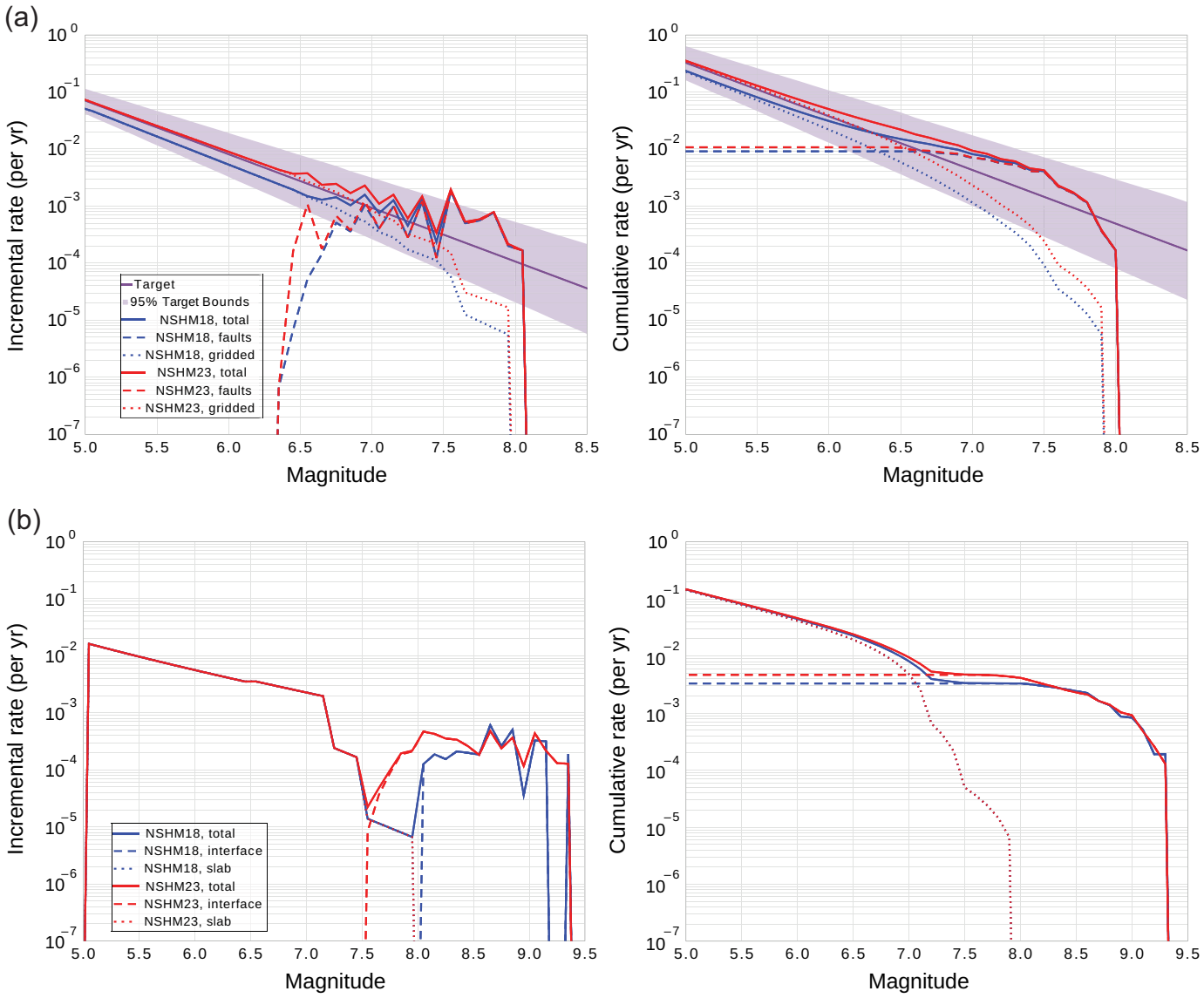

Figure 25. Model MFDs for (a) the CEUS and (b) the Cascadia subduction zone. Blue and red curves are for the NSHM14/18 and new model, respectively. Solid curves are for the complete model; dashed curves are for faults; and dotted curves are for gridded seismicity (or intra slab seismicity in panel b, for which the blue dotted line is hidden behind the red dotted line). The purple line and shaded region in panel (a) represent the observed target and 95% confidence intervals, respectively, CEUS (extrapolated from *M* 5 with no taper). The color version of this figure is available only in the electronic edition.

expected, the MFD for CEUS faults (including fault area sources) is relatively unchanged since NSHM14/18, except at lower magnitudes where the new Central Virginia and perhaps Saline River sources are influential. However, that the incremental MFD for faults in both the models exceeds the regional target over most magnitudes, as well as the associate upper 95% confidence bound just above *M* 7.5, implies a significant model overprediction (often referred to as a "bulge"), although one could argue that the observational uncertainties should be greater at higher magnitudes, given there are very few observations.

The MFDs for Cascadia are plotted in Figure 25b. This shows no change for the gridded seismicity (intraslab) model; the work by Llenos2023 has not yet been incorporated. The changes for the fault (subduction interface) are modest at larger magnitudes, and as shown in the next section subsequently, do not produce ≥10% changes with respect to 2% in 50 yr ground motions.

2018–2023 HAZARD CHANGES

This section documents where and why CONUS hazard has changed relative to NSHM14/18, holding GMMs constant so that we can focus on ERF-related differences. Only branch-averaged comparisons are made, and here we utilize the full logic tree set of GMMs from NSHM14/18. Figure 26 shows a map of 2in50 PGA for the new ERF, plus ratio and difference maps relative to NSHM14/18. The ratio map (Fig. 26b) saturates at plus and minus 50%, whereas ratios are up to a factor of

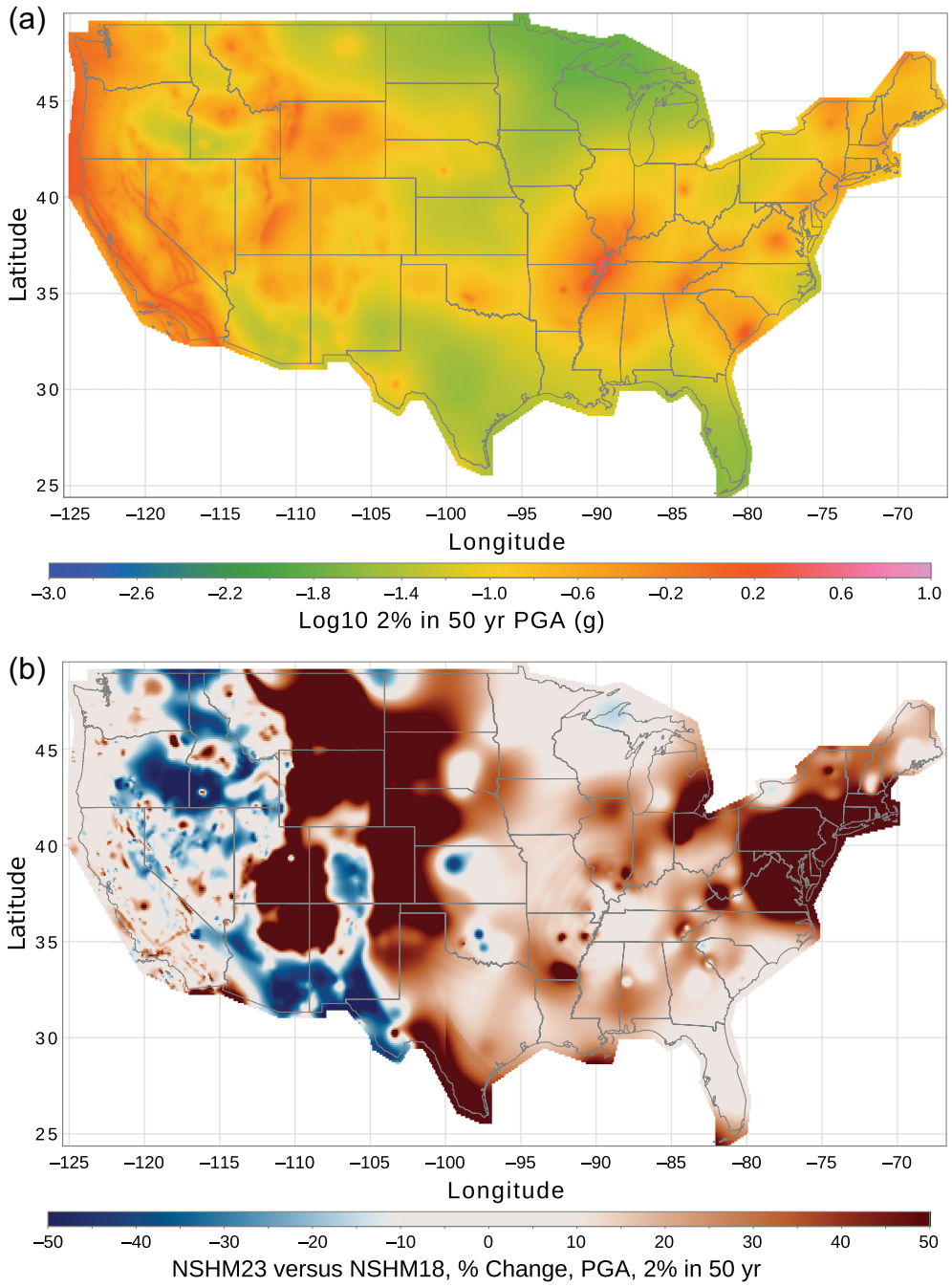

Figure 26. (a) The PGA that has a 2% chance of exceedance in 50 yr according to the new conterminous United States (CONUS) branch-averaged model (and the set of GMMs used in NSHM14/18 with $V_{S30} = 760$ m/s). (b) The percent change and (c) difference relative to that of the NSHM14/18 earthquake rupture forecast. All sources, such as Cascadia, are included. The color version of this figure is available only in the electronic edition. (*Continued*)

8.1 in some areas (this highest value being near the southern tip of Texas). However, the higher ratios are generally in lower hazard areas, meaning absolute differences are small as indicated in Figure 26c. The discontinuity in $M \geq 5$ rates at −104° longitude in Figure 13 is not visible in Figure 26, because the GMMs effectively smooth it out. The goal of our analysis has been to understand and explain all changes of more than 10%.

Figure 27a shows where fault model changes are influential; this map was generated using the new gridded seismicity model in both the numerator and denominator, which masks fault-related changes in areas dominated by gridded seismicity. The changes in CEUS are easy to explain; hazard has increased where sources were added (Central Virginia and Saline River in southern Arkansas) and where fault traces were extended (the Meers fault in Oklahoma and the Axial fault in the New Madrid area). Three sources added in the New Madrid area—Joiner Ridge and Crowley's Ridge (south) and (west)—did not increase hazard by more than 10%.

Explaining fault-related changes in WUS is much more complicated due to methodological changes, particularly outside California, and the strong influence of deformation models. Fortunately, the bottom line is simple: most differences are explained by fault moment-rate changes (the addition, removal, or modification of faults or changes in mean slip rates), with just a few areas influenced by other factors. Parsing this out required careful analysis (refer to recording number 8 under Video Recordings of Review Panel Briefings in Data and Resources). In short, we first made an approximate prediction of hazard changes caused only by fault moment-rate changes (involving mapping the moment rates in each fault model to grid cells and computing hazard using grid sources with otherwise identical MFD parameters). Examining correlation between this and hazard map ratio in Figure 27a allowed us to identify areas that may not be explained by fault moment-rate changes. Next, we held the deformation model constant (the average used in NSHM14/18) and incrementally stepped through other changes in going from

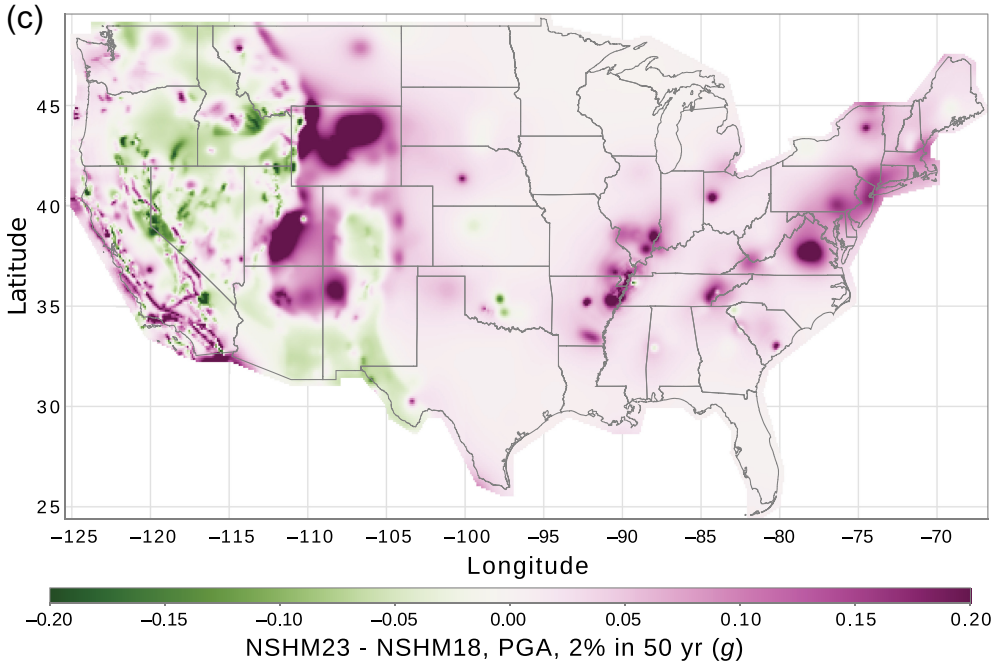

Figure 26. Continued

NSHM14/18 to the new model. This revealed the following with respect to non-California fault sources: (1) we can reproduce the previous classic model within our new fault system solution framework (a verification step); (2) adding alternative segmentation branches generally lowers hazard a bit (by 5%–15%), because allowing multifault ruptures lowers overall rates; and (3) replacing the Wells and Coppersmith (1994) magnitude–length model with the set of magnitude–area relations utilized here also generally lowers hazard by 5%–15% (because magnitude–length models predict lower maximum magnitudes for the predominantly dipping faults outside California). This analysis, and that conducted by Milner and Field (2023) with respect to hazard changes in the UCERF region, enabled us to identify the few areas that are dominated by something other than moment-rate differences; these cases are labeled in Figure 27a, and Milner and Field (2023) provide additional details for California.

Figure 27b shows areas in which hazard changes are dominated by gridded seismicity (computed using the new fault sources in both the numerator and denominator to mask areas dominated by faults). The causes of these differences, which determined by Llenos2023, are one or more of the following: (1) new earthquakes observed since 2018; (2) the addition of two new declustering algorithms (the Reasenberg, 1985 method tends to remove fewer aftershocks); (3) the removal of floor-rate zones in WUS; (4) updated induced seismicity zones; and (5) a change in the boundary between WUS and CEUS (now defined by −104° longitude). Areas dominated by each of these are identified in Figure 27b.

Again, the goal here has not been to document and describe changes with respect to a complete set of hazard and risk metrics, but rather to demonstrate an understanding and comfort with those of one commonly used metric (2in50 PGA). Our solution reports provide results for some other hazard metrics, and additional information on 2018–2023 NSHM hazard changes, including the influence of new GMMs, is given by Petersen *et al.* (2023a).

DISCUSSION AND CONCLUSIONS

Improvements over previous models

The new CONUS ERF presented here embodies a number of significant improvements, including an increase in the number of explicitly modeled faults, updates to other geologic constraints, the addition of two new deformation modeling techniques, a new fault creep model, and consideration of ghost transient (viscoelastic) effects. We also have new regional seismicity rate and *b*-value estimates, including uncertainties, which allows us to compare model MFDs with observations (for the first time outside California). Additional declustering algorithms were also added, as well as a revamped set of scaling relationships.

We have also improved the representation of multifault ruptures in WUS, both in terms of allowing more and less fault connectivity than in the previous models, and in sweeping over a broader range of total-rate models (rather than being constrained to stay as close as possible to the previous model, as in UCERF3). The inversion methodology has been completely overhauled for efficiency, reproducibility, and the generation of exhaustive web-based reports that include hazard analyses.

A semi-independent review team evaluated the deformation models (Johnson *et al.*, 2023), involving a novel scorecard approach in which each model was evaluated against 16 different metrics. An ad hoc group of USGS geologists (Hatem2023) evaluated the fault system solutions, which led to several model adjustments and future recommendations including: (1) refining the Wasatch segmentations because large ruptures were sneaking around boundaries via subsidiary faults, (2) removal of average paleo slip constraints as already noted, and (3) refinement of Wasatch and West Valley fault subsurface geometries near Salt Lake City.

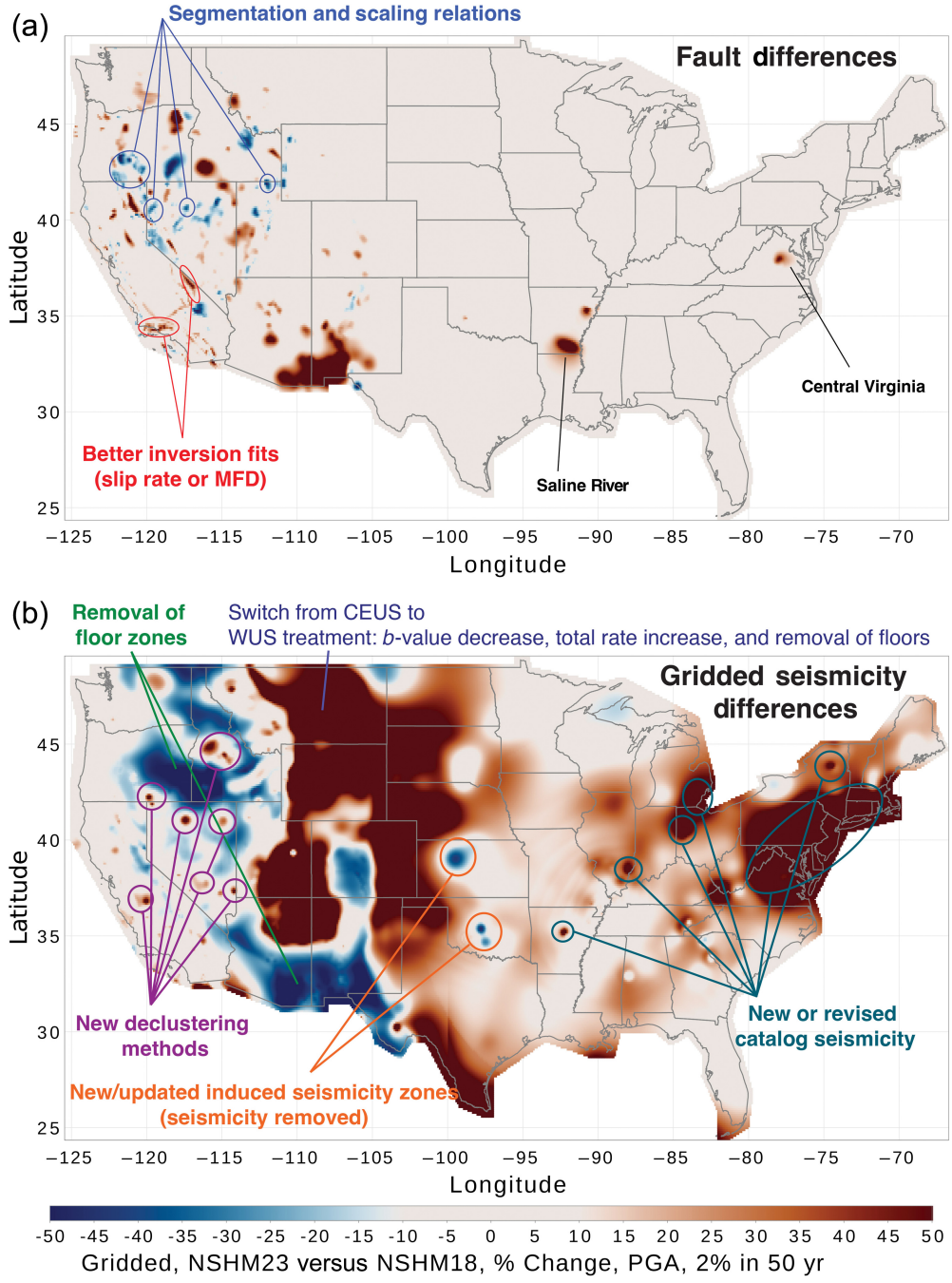

Figure 27. The 2% in 50 yr PGA percent changes, as in Figure 26b, but separated out by the (a) contribution from faults and (b) from gridded seismicity, constructed using the new gridded seismicity in both the numerator and denominator in panel (a), and doing similarly with respect to the new fault sources in panel (b). In panel (a), and outside California, all differences are caused by fault moment rate changes (addition, removal, or extension of faults or a change in mean slip rate), except where labeled differently. The color version of this figure is available only in the electronic edition.

The 19-member participatory review panel participated heavily indeed (Jordan *et al.*, 2023) and had substantial impact on the final model, some of which involved our heeding the following suggestions:

1. downweight the deformation models in accordance with slip-rate outlier analyses,
2. fix some erroneous fault rakes,
3. add rupture-length limits to the segmentation branch constraints (to suppress questionable rates of very long ruptures),
4. address a problem in which higher slip-rate faults were being systematically underfit,
5. add a scaling relationship that allows even higher average slip for large ruptures,
6. update the induced seismicity zones,
7. downweight the Reasenberg (1985) declustering and the fixed-smoothing branch,
8. downweight the classic segmentation branch (uniform weights were applied originally), and
9. verify model MFDs against historical observations at high magnitudes.

Downweighting the *Classic* segmentation branch (item 8) was one of the more controversial decisions, as many came into the project suggesting that the weight should be increased, at least outside California. However, this model is consistently problematic with respect to the following: (1) overpredicting the regional MFD (the "bulge" problem illustrated in Fig. 16b); (2) possible rupture length distribution issues (e.g., Fig. 21a); and (3) defining the exceptions (Table 5), which largely amounts to assuming faults cannot co-rupture until nature proves us wrong. The latter issue was the most frustrating for those implementing the model because a reproducible algorithm for defining the exceptions was not provided. Again, the extreme segmentation branches are partly a proxy for over- or underestimated connectivity in the fault model, and the exact branch weights are not highly influential with respect to the mean hazard metrics considered for the 2023 USGS NSHM. For these reasons, we were somewhat ambivalent

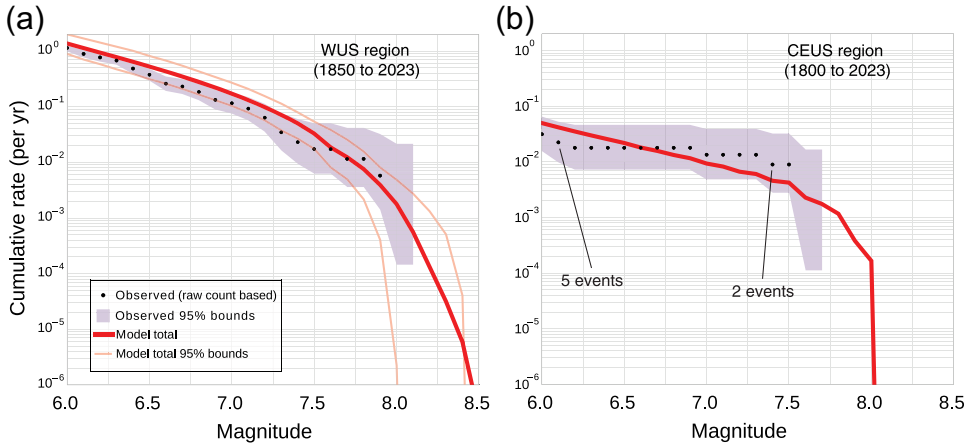

Figure 28. Comparison of (a) WUS and (b) CEUS branch-averaged model MFDs (thick red lines) with event-count-based rates (black circles) for $M \geq 6$ seismicity (number of events divided by the time period as labeled for each region). Uncertainties on the latter (shaded region) are based on a Poisson assumption, and model uncertainties are shown with the lighter red lines (for WUS only), both of which represent 95% confidence. The color version of this figure is available only in the electronic edition.

about final segmentation weights. As implied by the final branch weights (Fig. 2, Table 4), we ended up heeding the review panel advice, but with the stipulation that the other end members (*None* and *High*) be downweighted as well.

Regarding panel recommendation (item 8), the issue is that our total $M \geq 5$ rate and b-value constraints are effectively inferred from smaller ($M < 5$) earthquakes (Michael2023), which raises the question of how well our model is matching observations at higher (e.g., supraseismogenic) magnitudes. Figure 28 provides the answer for WUS and CEUS, for which the branch averaged model (red curve) is compared with the historically observed rate of $M > 6$ events (black circles representing raw counts divided by the associated catalog-completeness interval), with uncertainties on the latter derived by assuming a Poisson model as developed by Michael2023. For WUS, the observed cumulative rates are systematically lower than the model prediction up to M 7.5 but well within the uncertainties. For CEUS, the observed rate is not only lower near $M \geq 6.25$ (perhaps reflecting missed events) and higher at the largest magnitudes, but also well within the uncertainties at all magnitudes.

The review process also revealed remaining concerns over using undeclustered models for USGS NSHM hazard calculations, so some additional comments are provided here. The problem is illustrated in Figure 29, which compares the undeclustered MFD with those from declustered catalogs for the WUS and CEUS Collection regions (based on the total $M \geq 5$ rate and b-value inferences of Michael2023. In WUS, the GK declustering (red line in Fig. 29a) lowers total $M \geq 5$ rate by about 50%, but it also lowers the b-value, causing a crossover point above which rates are erroneously high (declustering cannot lead to an increase in rates). This issue was recognized and handled properly in UCERF3, so applying GK filtering in NSHM hazard calculations was both reasonable and needed for consistency with other regions. The bigger issue now is that the newly added NN declustering algorithm (Zaliapin and Ben-Zion, 2020) removes about half of all events at all the magnitudes (blue line in Fig. 29a), which we already noted is consistent with other modern declustering approaches (essentially because aftershocks can be larger than their mainshocks). However, no one is advocating that we remove half of all events from our hazard calculations. The same effect is seen for the CEUS region (Fig. 29b), but where the GK crossover point is near M 4.5, implying it erroneously overpredicts rates at higher magnitudes, which we do not want in hazard calculations either. The only solution is to calibrate models to the total MFD (including aftershocks). If treating the result as a Poisson process is problematic, then the proper solution is to develop and deploy models that explicitly and realistically represent spatiotemporal clustering. In fact, the latter is needed to explore whether the Poisson assumption is problematic in the first place, as exemplified by Field *et al.* (2021). As already noted in the Aftershocks section above, several studies have concluded that, with respect to USGS NSHM 2023 hazard metrics (2% and 10% in 50 yr ground motions), we are better off keeping aftershocks and assuming a Poisson process than declustering with antiquated or biasing methodologies (Marzocchi and Taroni, 2014; Field *et al.*, 2021; Wang *et al.*, 2021; Michael and Llenos, 2022). Although we consider this modification a model improvement, additional work is warranted with respect to deploying fully time-dependent ERFs nationwide.

Model limitations

Despite improvements, the new model is a limited representation of the system in terms of embodying assumptions, approximations, and data uncertainties. For example, we continue to differentiate between "on-fault" and "off-fault" ruptures, whereas nature will surely violate this model distinction. We also acknowledge that our fault model is a simplification of reality, and that future large ruptures will not exactly match it.

Although we believe the logic tree branch weights are applicable in general, adjustments may be warranted in certain situations. For example, further scrutiny may justify a

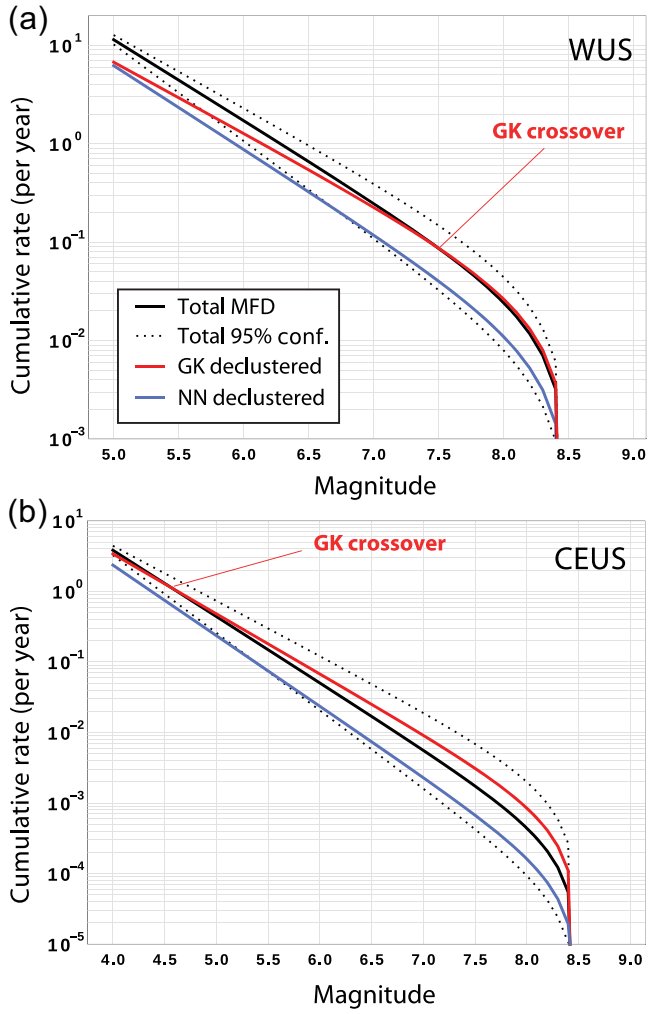

Figure 29. The influence of declustering on (a) WUS and (b) CEUS regional MFDs, as implied by the analysis of Micheal (written comm., 2023, as described in the Gridded seismicity sources section). Black shows the total MFD (including aftershocks) plus the 95% confidence bounds (dotted) implied by the total $M \geq 5$ rate and *b*-values listed in Table 6 (assuming the maximum magnitude of 8.5 for plotting purposes). Red and blue show the MFDs implied by the GK (Gardner and Knopoff, 1974) and NN (the nearest-neighbor approach of Zaliapin and Ben-Zion, 2020) declustering algorithms, respectively. Results for Reasenberg (1985) are not shown but are relatively close to the total MFD. Note that GK exhibits a crossover point, as labeled, above which there is an erroneous overprediction of larger events. The color version of this figure is available only in the electronic edition.

different set of deformation model weights near specific faults, especially given questions about how each model samples the null space (described in the Deformation models section). Correlation assumptions may also justify branch weight modifications. For example, a 10% weight on the *Classic* and no-segmentation branches seems rational for site-specific hazard (because the actual connectivity of nearby faults may be more or less than implied by the fault model), but the likelihood that either of these branches applies to all fault in a region is more doubtful, so weight adjustments might be appropriate for spatially distributed hazard and risk metrics (e.g., statewide portfolio losses). Of course, any such adjustments should be based on science (not desired outcomes), and the USGS can provide authoritative judgments as broadly needed.

Another presently unresolved issue is the best way to combine sources that have completely different (uncorrelated) logic tree branches. For example, if Cascadia has X branches, do we combine these with all N WUS branches, yielding $N \times X$ branches? Alternatively, should we keep them separate and combine the consequent hazard PDFs, or use Monte Carlo sampling, both of which might complicate quantifying the influence of different branches? Or do we construct philosophically similar sets of branches for each source and assume correlation? Until we address these questions, full consideration of all epistemic uncertainties will remain a challenge in hazard and risk analyses.

Each inversion-based fault system solution includes quantitative metrics on how well the final model fits each data constraint. In principle, these misfits could be used to adjust logic tree branch weights a posteriori (e.g., using Bayes theorem with a priori branch weights). This has proven challenging in practice, however, because better fits do not always reflect a better model. For example, a target MFD with higher *b*-value appears superior, but this is only because it has more, smaller earthquakes with which to fit noisy slip-rate fluctuations. That said, several branches were assigned uniform weights because we lacked a good basis for doing otherwise. Further scrutiny of the model, particularly in terms of data fits, will presumably lead to some desirable adjustments.

Finally, given the questions associated with using nondeclustered models and the correlation assumptions on the segmentation and *b*-value branches, care might be in order when applying the model to shorter-term probabilities (e.g., 40% in 50 yr ground motions) and to spatially broad hazard and risk metrics (e.g., statewide portfolio losses).

Future improvements

As mentioned in the Introduction, we plan to add time-dependent components in future versions (e.g., elastic rebound, spatiotemporal clustering, induced seismicity, and swarms). Fully time-dependent models are needed not only as a potential basis for operational earthquake forecasting (Jordan *et al.*, 2014), should that be deemed useful, but to also evaluate assumptions made in our time-independent model (e.g., assuming a Poisson process with a non-declustered model). But in terms of improving the time-independent model presented here, effort is warranted with respect to improving the deformation models because fault-slip rates continue to be one of the most influential factors on seismic hazard. Given the outlier problem with respect to the five models applied here, attention could be given to not only the viability of different modeling approaches but also with respect to how each maps out any solution null space;

in fact, it would be ideal if each approach provided a suite of viable models that represents both a systematic traversal of null spaces and a basis for representing slip-rate covariance. We also want to improve the reliability of the off-fault deformation estimates from these models, both in terms of total moment rate and the spatial distribution of off-fault earthquakes (on which we have made no progress since UCERF3).

In developing this ERF, we were continually asking whether a decision or model option is consequential with respect to hazard or risk estimates. Although we were often able to answer this question with respect to more traditional hazard metrics, the extent to which we can operationalize this capability, and with a broader set of risk metrics, would increase the rate at which we can provide even more useful models. For example, we are still unsure of the consequences of having exceptionally long (e.g., ≥ 700 km) ruptures with respect to statewide losses in California and of the influence of the various logic tree branches on this risk metric. Again, operationalized processing would be beneficial with respect to a necessary and sufficient set of hazard and risk metrics.

We also plan to explore applicability of fault system solutions in other areas (New Madrid and Alaska faults, and the Cascadia and the Aleutian subduction zones), in part to enable computing implied attributes, such as subduction slip rates, and for adding time dependencies. Another high priority is better quantification of epistemic uncertainties associated with the gridded seismicity model, especially given the limited sample of instrumental and historical earthquakes; we need better procedures for quantifying the implications of this sampling error, and fully time-dependent models would be highly useful for this purpose. We also need to determine the value of developing site-specific models for the probability of missed events at paleoseismic trenches (we are still using generic models).

Of course, model testing is of paramount importance, including everything from component-specific evaluations, based on traditional science, to more formalized, objective evaluations from entities like the Collaboratory for the Study of Earthquake Predictability (Zechar *et al.*, 2013; Savran *et al.*, 2022). Longer term, multicycle physics-based simulators (e.g., Tullis, 2012 and references therein) are perhaps our best opportunity for addressing many enduring ERF-related questions, including the propensity of multifault ruptures, earthquake scaling, the influence of creep, the shape of MFDs on faults, elastic rebound predictability, and spatiotemporal clustering details at larger magnitudes (e.g., Field, 2019). A more comprehensive list of research priorities can be found in the ERF section of the annual external grants announcement of the USGS Earthquake Hazards Program.

DATA AND RESOURCES

Web-based solution reports are available at https://data.opensha.org/nshm23/reports/reports.html. Solution report links referred to in the article are as follows: link 1: https://data.opensha.org/nshm23/reports/misc_plots/reg_mfds_comp_nshm18/CONUS_U3_RELM_mfds_SUPRA_ONLY_cml.pdf; link 2: https://data.opensha.org/nshm23/reports/misc_plots/reg_mfds_comp_nshm18/CONUS_U3_RELM_mfds_GRID_ONLY_cml.pdf; link 3: https://data.opensha.org/nshm23/reports/branch_averaged_gridded/#slip-rates; link 4: https://data.opensha.org/nshm23/reports/branch_averaged_gridded/#paleoseismic-data-comparison; link 5: https://data.opensha.org/nshm23/reports/branch_averaged_gridded/resources/conn_passthrough_MIN_supra_seis.png; link 6: https://data.opensha.org/nshm23/reports/branch_averaged_gridded/parent_sect_pages/Cucamonga/#connectivity; link 7: https://data.opensha.org/nshm23/reports/branch_averaged_gridded/parent_sect_pages/Cucamonga/#rupture-examples; link 8: https://data.opensha.org/nshm23/reports/branch_averaged_gridded/#fault-participation-rates; link 9: https://data.opensha.org/nshm23/reports/branch_averaged_gridded/#parent-section-detail-pages; link 10: https://data.opensha.org/nshm23/reports/branch_averaged_gridded/parent_sect_pages/Wasatch_Salt_Lake_City_north/#cumulative-rates-and-recurrence-intervals-table; link 11: https://data.opensha.org/nshm23/reports/branch_averaged_gridded/#special-fault-detail-pages; link 12: https://data.opensha.org/nshm23/reports/site_hazard_full_gridded/. All the websites were last accessed in May 2023. The National Seismic Hazard Model (NSHM) 2023 Data Release is available at doi: 10.5066/P9GNPCOD (Petersen *et al.*, 2023b). The video recordings of review panel briefings are available at https://earthquake.usgs.gov/static/lfs/nshm/workshops/workshop-recordings/erf/ (last accessed September 2023). The computer codes are as follows: most calculations were made using OpenSHA (http://www. OpenSHA.org, last accessed August 2023; Field *et al.*, 2003), which in turn utilizes the following for making plots: Generic Mapping Tools (GMT; https://www.generic-mapping-tools.org) and JFree-Chart (http://www.jfree.org/jfreechart/). Both the websites were last accessed in May 2023. Calculations were also based on the U.S. Geological Survey (USGS) nshmp-haz codes (Powers *et al.*, 2022, doi: 10.5066/P9STF5GK).

DECLARATION OF COMPETING INTERESTS

The authors acknowledge that there are no conflicts of interest recorded.

ACKNOWLEDGMENTS

First and foremost, the authors owe a huge debt of gratitude to the chair of their review panel (Tom Jordan) and to all the other participants of that panel: Norm Abrahamson, John Anderson, Glenn Biasi, Kenneth Campbell, Timothy Dawson, Heather De Shon, Matt Gerstenberger, Nick Gregor, Keith Kelson, Yajie Lee, Nicolas Luco, Warner Marzocchi, Badie Rowshandel, David Schwartz, Nilesh Shome, Gabriel Toro, Ray Weldon, and Ivan Wong. The authors are also indebted to the deformation models review team (Kaj Johnson, William Hammond, and Ray Weldon) and to the ad hoc group of U.S. Geological Survey (USGS) geologists that scrutinized the western U.S. (WUS) fault system solutions (Alex Hatem, Rich Briggs, Chris DuRoss, Kate Scharer, Steve DeLong, Jessie Thompson Jobe, Suzanne Hecker, Rob Witter, Belle Philibosian, Nadine Reitman, Devin McPhillips, Austin Elliott, Steve Angster, Brian Sherrod, Chad Trexler, and Sylvia Nicovich). Finally, two *BSSA* reviewers provided many constructive suggestions.

REFERENCES

Abrahamson, N. A., W. J. Silva, and R. Kamai (2014). Summary of the ASK14 ground motion relation for active crustal regions, *Earthq. Spectra* **30,** 1025–1055, doi: 10.1193/070913EQS198M.

Andrews, D. J., and E. Schwerer (2000). Probability of rupture of multiple fault segments, *Bull. Seismol. Soc. Am.* **90,** 1498–1506, doi: 10.1785/0119990163.

Biasi, G. P. (2013). Appendix H: Maximum likelihood recurrence intervals for California paleoseismic sites, in *Uniform California Earthquake Rupture Forecast, Version 3 (UCERF3): The Time-Independent Model*, E. H. Field, G. P. Biasi, P. Bird, T. E. Dawson, K. R. Felzer, D. D. Jackson, K. M. Johnson, T. H. Jordan, C. Madden, and A. J. Michael, *et al.* (Editors), *U.S. Geol. Surv. Open-File Rept. 2013-1165 and California Geol. Surv. Special Rept. 228*, 25 pp., doi: 10.3133/ofr20131165.

Biasi, G. P., and S. G. Wesnousky (2016). Steps and gaps in ground ruptures: Empirical bounds on rupture propagation, *Bull. Seismol. Soc. Am.* **106,** 1110–1124, doi: 10.1785/0120150175.

Biasi, G. P., and S. G. Wesnousky (2017). Bends and ends of surface ruptures, *Bull. Seismol. Soc. Am.* **107,** 2543–2560, doi: 10.1785/0120160292.

Bird, P. (2009). Long-term fault slip rates, distributed deformation rates, and forecast of seismicity in the western United States from joint fitting of community geologic, geodetic, and stress direction data sets, *J. Geophys. Res.* **114,** B11403, doi: 10.1029/2009JB006317.

Coppersmith, K. J., L. A. Salomone, C. W. Fuller, L. L. Glaser, K. L. Hanson, R. D. Hartleb, W. R. Lettis, S. C. Lindvall, S. M. McDuffie, R. K. McGuire, *et al.* (2012). Central and Eastern United States seismic source characterization for nuclear facilities, *U.S. Nuclear Regulatory Commission (NRC) Rept. NUREG-2115, U.S. Department of Energy (DOE) Rept. DOE/NE-0140, and Electric Power Research Institute (EPRI) Rept. 1021097*, 3176 pp., doi: 10.2172/1041187, full report available at http://www.ceus-ssc.com/ (last accessed May 2023).

Dieterich, J. H., and K. B. Richards-Dinger (2010). Earthquake recurrence in simulated fault systems, *Pure Appl. Geophys.* **167,** 1087–1184.

Evans, E. L. (2022). A dense block model representing western continental United States deformation for the 2023 update to the National Seismic Hazard model, *Seismol. Res. Lett.* **93,** 3024–3036, doi: 10.1785/0220220141.

Field, E. H. (2019). How physics-based earthquake simulators might help improve earthquake forecasts, *Seismol. Res. Lett.* **90,** 467–472, doi: 10.1785/0220180299.

Field, E. H., and M. T. Page (2011). Estimating earthquake-rupture rates on a fault or fault system, *Bull. Seismol. Soc. Am.* **101,** 79–92, doi: 10.1785/0120100004.

Field, E. H., R. J. Arrowsmith, G. P. Biasi, P. Bird, T. E. Dawson, K. R. Felzer, D. D. Jackson, K. M. Johnson, T. H. Jordan, C. Madden, *et al.* (2014). Uniform California Earthquake Rupture Forecast, version 3 (UCERF3)—The time-independent model, *Bull. Seismol. Soc. Am.* **104,** 1122–1180, doi: 10.1785/0120130164.

Field, E. H., G. P. Biasi, P. Bird, T. E. Dawson, K. R. Felzer, D. D. Jackson, K. M. Johnson, T. H. Jordan, C. Madden, and A. J. Michael (2015). Long-term time-dependent probabilities for the third uniform california earthquake rupture forecast (UCERF3), *Bull. Seismol. Soc. Am.* **105,** 511–543, doi: 10.1785/0120140093.

Field, E. H., T. E. Dawson, K. R. Felzer, A. D. Frankel, V. Gupta, T. H. Jordan, T. Parsons, M. D. Petersen, R. S. Stein, R. J. Weldon II, *et al.* (2009). Uniform California Earthquake Rupture Forecast, Version 2 (UCERF2), *Bull. Seismol. Soc. Am.* **99,** 2053–2107, doi: 10.1785/0120080049.

Field, E. H., T. H. Jordan, and C. A. Cornell (2003). OpenSHA: A developing community-modeling environment for seismic hazard analysis, *Seismol. Res. Lett.* **74,** 406–419, doi: 10.1785/gssrl.74.4.406.

Field, E. H., T. H. Jordan, M. T. Page, K. R. Milner, B. E. Shaw, T. E. Dawson, G. P. Biasi, T. Parsons, J. L. Hardebeck, A. J. Michael, *et al.* (2017). A synoptic view of the third uniform California earthquake rupture forecast (UCERF3), *Seismol. Res. Lett.* **88,** 1259–1267, doi: 10.1785/0220170045.

Field, E. H., K. R. Milner, and N. Luco (2021). The seismic hazard implications of declustering and Poisson assumptions inferred from a fully time-dependent model, *Bull. Seismol. Soc. Am.* **112,** 527–537, doi: 10.1785/0120210027.

Field, E. H., K. R. Milner, and M. T. Page (2020). Generalizing the inversion-based PSHA source model for an interconnected fault system, *Bull. Seismol. Soc. Am.* **111,** 371–390, doi: 10.1785/0120200219.

Field, E. H., K. R. Milner, and K. Porter (2020). Assessing the value of removing earthquake-hazard-related epistemic uncertainties, exemplified using average annual loss in California, *Earthq. Spectra* **4,** 1912–1929, doi: 10.1177/8755293020926185.

Frankel, A. (1995). Mapping seismic hazard in the central and eastern United States, *Seismol. Res. Lett.* **66,** 8–21, doi: 10.1785/gssrl.66.4.8.

Frankel, A., R. Chen, M. Petersen, M. Moschetti, and B. Sherrod (2015). 2014 Update of the Pacific Northwest portion of the U.S. National Seismic Hazard Maps, *Earthq. Spectra* **31,** S131–S148, doi: 10.1193/111314EQS193M.

Gardner, J. K., and L. Knopoff (1974). Is the sequence of earthquakes in southern California with aftershocks removed Poissonian? *Bull. Seismol. Soc. Am.* **64,** 1363–1367, doi: 10.1785/BSSA0640051363.

Gerstenberger, M. C., R. J. Van Dissen, C. Rollins, C. DiCaprio, C. Chamberlain, A. Christophersen, G. L. Coffey, S. M. Ellis, P. Iturrieta, K. M. Johnson, *et al.* (2022). The seismicity rate model for the 2022 New Zealand National Seismic Hazard Model, *GNS Science Rept. 2022/47*, GNS Science, Lower Hutt, New Zealand, 156 pp., doi: 10.21420/2EXG-NP48.

Goldfinger, C., S. Galer, J. Beeson, T. Hamilton, B. Black, C. Romsos, J. Patton, C. H. Nelson, R. Hausmann, and A. Morey (2017). The importance of site selection, sediment supply, and hydrodynamics: A case study of submarine paleoseismology on the northern Cascadia margin, Washington USA, *Mar. Geol.* 384**,** 4–16, doi: 10.1016/j.margeo.2016.06.008.

Goldfinger, C., C. H. Nelson, A. E. Morey, J. E. Johnson, J. R. Patton, E. B. Karabanov, J. Gutierrez-Pastor, A. T. Eriksson, E. Gracia, G. Dunhill, *et al.* (2012). Turbidite event history: Methods and implications for Holocene paleoseismicity of the Cascadia subduction zone, *U.S. Geol. Surv. Profess. Pap. 1661-F*, 170 pp., doi: 10.3133/pp1661F.

Hanks, T. C., and W. H. Bakun (2008). M-log A observations of recent large earthquakes, *Bull. Seismol. Soc. Am.* **98,** 490.

Hatem, A. E., C. M. Collett, R. W. Briggs, R. D. Gold, S. J. Angster, E. H. Field, P. M. Powers, and , and Earthquake Geology Working Group (2022). Simplifying complex fault data for systems-level

analysis: Earthquake geology inputs for U.S. NSHM 2023, *Sci. Data* **9,** 506, doi: 10.1038/s41597-022-01609-7.

Hatem, A. E., N. Reitman, R. Briggs, R. Gold, and J. Thompson Jobe (2022). Western U.S. geologic deformation model for use in the U.S. National Seismic Hazard Model 2023, *Seismol. Res. Lett.* **93,** 3053–3067, doi: 10.1785/0220220154.

Hearn, E. H. (2022). "Ghost transient" corrections to the southern California GPS velocity field from San Andreas fault seismic cycle models, *Seismol. Res. Lett.* **93,** 2793–2989, doi: 10.1785/0220220156.

Hecker, S., N. A. Abrahamson, and K. E. Wooddell (2013). Variability of displacement at a point: Implications for earthquake-size distribution and rupture hazard on faults, *Bull. Seismol. Soc. Am.* **103,** 651–674, doi: 10.1785/0120120159.

Johnson, K. J., W. C. Hammond, and R. Weldon (2023). Review of geodetic and geologic deformation models of 2023 US National Seismic Hazard Model, *Bull. Seismol. Soc. Am.* doi: 10.1785/0120220137.

Johnson, K. J., J. R. Murray, and C. Wespestad (2022). Creep rate models for the 2023 US National Seismic Hazard Model: Physically constrained inversions for the distribution of creep on California faults, *Seismol. Res. Lett.* **93,** 3151–3169, doi: 10.1785/0220220186.

Jordan, T. H., N. Abrahamson, J. G. Anderson, G. Biasi, K. Campbell, T. Dawson, H. DeShon, M. Gerstenberger, N. Gregor, K. Kelson, *et al.* (2023). Panel review of the USGS 2023 conterminous U.S. time-independent earthquake rupture forecast, *Bull. Seismol. Soc. Am.* doi: 10.1785/0120230140.

Jordan, T. H., W. Marzocchi, A. J. Michael, and M. C. Gerstenberger (2014). Operational earthquake forecasting can enhance earthquake preparedness, *Seismol. Res. Lett.* **85,** 955–959, doi: 10.1785/0220140143.

Kelsey, H. M., A. R. Nelson, E. Hemphill-Haley, and R. C. Witter (2005). Tsunami history of an Oregon coastal lake reveals a 4600 yr record of great earthquakes on the Cascadia subduction zone, *Geol. Soc Am. Bull.* **117,** 1009–1032, doi: 10.1130/B25452.1.

Klein, F. W., A. D. Frankel, C. S. Mueller, R. L. Wesson, and P. G. Okubo (2001). Seismic hazard in Hawaii: High rate of large earthquakes and probabilistic ground-motion maps, *Bull. Seismol. Soc. Am.* 91**,** 479–498, doi: 10.1785/0120000060.

Madden, C., D. E. Haddad, J. B. Salisbury, O. Zielke, J. R. Arrowsmith, R. J. Weldon II, J. Colunga (2013). Appendix R: Compilation of slip in the last event data and analysis of last event, repeated slip, and average displacement for recent and prehistoric ruptures, in *Uniform California Earthquake Rupture Forecast, Version 3 (UCERF3): The Time-Independent Model*, E. H. Field, G. P. Biasi, P. Bird, T. E. Dawson, K. R. Felzer, D. D. Jackson, K. M. Johnson, T. H. Jordan, C. Madden, and A. J. Michael, *et al.* (Editors), *U.S. Geol. Surv. Open-File Rept. 2013-1165, and California Geol. Surv. Special Rept. 228*, 65 pp., doi: 10.3133/ofr20131165.

Marzocchi, W., and M. Taroni (2014). Some thoughts on declustering in probabilistic seismic-hazard analysis, *Bull. Seismol. Soc. Am.* **104,** 1838–1845, doi: 10.1785/0120130300.

McPhillips, D. (2022). Revised earthquake recurrence intervals in California, U.S.A.: New paleoseismic sites and application of event likelihoods, *Seismol. Res. Lett.* **93,** 3009–3023, doi: 10.1785/0220220127.

Michael, A. J., and A. L. Llenos (2022). An efficient, analytic solution using order statistics for probabilistic seismic-hazard assessment without the Poisson assumption, *Bull. Seismol. Soc. Am.* **112,** 1678–1693, doi: 10.1785/0120210216.

Milner, K. R., and E. H. Field (2023). A comprehensive fault system inversion approach: Methods and application to NSHM23, *Bull. Seismol. Soc. Am.* doi: 10.1785/0120230122.

Milner, K. R., B. E. Shaw, and E. H. Field (2022). Enumerating plausible multifault ruptures in complex fault systems with physical constraints, *Bull. Seismol. Soc. Am.* **112,** 1806–1824, doi: 10.1785/0120210322.

Milner, K. R., B. E. Shaw, C. A. Goulet, K. B. Richards-Dinger, S. Callaghan, T. H. Jordan, J. H. Dieterich, and E. H. Field (2021). Toward physics-based nonergodic PSHA: A prototype fully deterministic seismic hazard model for southern California, *Bull. Seismol. Soc. Am.* **111,** 898–915, doi: 10.1785/0120200216.

Mueller, C. S. (2019). Earthquake catalogs for the USGS National Seismic Hazard Maps, *Seismol. Res. Lett.* **90,** 251–261, doi: 10.1785/0220170108.

Nelson, A. R., C. B. DuRoss, R. C. Witter, H. M. Kelsey, S. E. Engelhart, S. A. Mahan, H. J. Gray, A. D. Hawkes, B. P. Horton, and J. S. Padgett (2021). A maximum rupture model for the central and southern Cascadia subduction zone—Reassessing ages for coastal evidence of megathrust earthquakes and tsunamis, *Quaternary Sci. Rev.* **261,** 106922, doi: 10.1016/j.quascirev.2021.106922.

Nelson, A. R., H. M. Kelsey, and R. C. Witter (2006). Great earthquakes of variable magnitude at the Cascadia subduction zone, *Quaternary Res.* **65,** 354–365, doi: 10.1016/j.yqres.2006.02.009.

Ogata, Y. (1988). Statistical models of point occurrences and residual analysis for point processes, *J. Am. Stat. Assoc.* **83,** 9–27, doi: 10.2307/2288914.

Ogata, Y. (1998). Space-time point-process models for earthquake occurrences, *Ann. Inst. Statist. Math.* **50,** 379–402, doi: 10.1023/A:1003403601725.

Page, M. T. (2021). More fault connectivity is needed in seismic hazard analysis, *Bull. Seismol. Soc. Am.* **111,** 391–397, doi: 10.1785/0120200119.

Page, M. T., E. H. Field, K. R. Milner, and P. M. Powers (2014). The UCERF3 grand inversion: Solving for the long-term rate of ruptures in a fault system, *Bull. Seismol. Soc. Am.* 104**,** 1181–1204, doi: 10.1785/0120130180.

Petersen, M. D., A. D. Frankel, S. C. Harmsen, C. S. Mueller, K. M. Haller, R. L. Wheeler, R. L. Wesson, Y. Zeng, O. S. Boyd, D. M. Perkins, *et al.* (2008) Documentation for the 2008 update of the United States National Seismic Hazard Maps, *U.S. Geol. Surv. Open-File Rept. 2008-1128*, 61 pp., doi: 10.3133/ofr20081128.

Petersen, M. D., M. P. Moschetti, P. M. Powers, C. S. Mueller, K. M. Haller, A. D. Frankel, Y. Zeng, S. Rezaeian, S. C. Harmsen, O. S. Boyd, *et al.* (2014). Documentation for the 2014 update of the United States National Seismic Hazards Maps, *U.S. Geol. Surv. Open-File Rept. 2014-1091*, 243 pp., doi: 10.3133/ofr20141091.

Petersen, M. D., M. P. Moschetti, P. M. Powers, C. S. Mueller, K. M. Haller, A. D. Frankel, Y. Zeng, S. Rezaeian, S. C. Harmsen, O. S. Boyd, *et al.* (2015). The 2014 United States National Seismic Hazard Model, *Earthq. Spectra* **31,** S1–S30, doi: 10.1193/120814EQS210M.

Petersen, M. D., A. M. Shumway, P. M. Powers, E. H. Field, M. P. Moschetti, K. S. Jaiswal, K. R. Milner, S. Rezaeian, A. D. Frankel, A. L. Llenos, *et al.* (2023a). The 2023 U.S. 50-State

National Seismic Hazard Model: Overview and implications, *Earthq. Spectra*, available at https://journals.sagepub.com/doi/abs/10.1177/8755293023/1215428.

Petersen, M. D., A. M. Shumway, P. M. Powers, E. H. Field, M. P. Moschetti, K. S. Jaiswal, K. R. Milner, S. Rezaeian, A. D. Frankel, A. L. Llenos, *et al.* (2023b). 2023 50-State National Seismic Hazard Policy Model: Overview, *U.S. Geol. Surv. Data Release*, doi 10.5066/P9GNPCOD.

Petersen, M. D., A. M. Shumway, P. M. Powers, M. P. Moschetti, A. L. Llenos, A. J. Michael, C. S. Mueller, A. D. Frankel, S. Rezaiean, K. S. Rukstales, *et al.* (2021). 2021 US National Seismic Hazard Model for the state of Hawaii, *Earthq. Spectra* **38,** 865–916, doi: 10.1177/87552930211052061.

Petersen, M. D., A. M. Shumway, P. M. Powers, C. S. Mueller, M. P. Moschetti, A. D. Frankel, S. Rezaeian, D. E. McNamara, N. Luco, O. S. Boyd, *et al.* (2020). 2018 Update of the U.S. National Seismic Hazard Model: Overview of model and implications, *Earthq. Spectra* **36,** 5–41, doi: 10.1177/8755293019878199.

Pollitz, F. F. (2022). Viscoelastic fault-based model of crustal deformation for the 2023 update to the US National Seismic Hazard model, *Seismol. Res. Lett.* **93,** 3087–3099, doi: 10.1785/0220220137.

Pollitz, F. F., E. L. Evans, E. H. Field, A. E. Hatem, E. H. Hearn, K. Johnson, J. R. Murray, P. M. Powers, Z.-K. Shen, C. Wespestad, *et al.* (2022). Western U.S. deformation models for the 2023 update to the U.S. National Seismic Hazard Model, *Seismol. Res. Lett.* **93,** 3068–3086, doi: 10.1785/0220220143.

Porter, K., E. Field, and K. Milner (2017). Trimming a hazard logic tree with a new model-order-reduction technique, *Earthq. Spec.* **33,** 857–874, doi: 10.1193/092616eqs158m.

Powers, P. M., B. S. Clayton, and J. M. Altekruse (2022). nshmp-haz: National Seismic Hazard Model Project hazard applications and web services, *U.S. Geol. Surv. Softw. Release*, doi: 10.5066/P9STF5GK.

Reasenberg, P. (1985). Second-order moment of central California seismicity, 1969-1982, *J. Geophys. Res.* **90,** 5479–5496, doi: 10.1029/JB090iB07p05479.

Savran, W. H., J. A. Bayona, P. Iturrieta, K. M. Asim, H. Bao, K. Bayliss, M. Herrmann, D. Schorlemmer, P. J. Maechling, and M. J. Werner (2022). pyCSEP: A Python toolkit for earthquake forecast developers, *Seismol. Res. Lett.* **93,** 2858–2870, doi: 10.1785/0220220033.

Schwartz, D. P. (2018). Review: Past and future fault rupture lengths in seismic source characterization—The long and short of it, *Bull. Seismol. Soc. Am.* **108,** 2493–2520, doi: 10.1785/0120160110.

Shaw, B. E. (2019). Beyond backslip: Improvement of earthquake simulators from new hybrid loading conditions, *Bull. Seismol. Soc. Am.* **109,** 2159–2167, doi: 10.1785/0120180128.

Shaw, B. E. (2023). Magnitude and slip scaling relations for fault based seismic hazard, *Bull. Seismol. Soc. Am.* **113,** 924–947, doi: 10.1785/0120220144.

Shen, Z.-K., and P. Bird (2022). Neokinema deformation model for the 2023 update to the U.S. National Seismic Hazard Model, *Seismol. Res. Lett.* **93,** 3037–3052, doi: 10.1785/0220220179.

Thompson Jobe, J., A. E. Hatem, R. Gold, C. DuRoss, N. Reitman, R. Briggs, and C. Collett (2022). Revised earthquake geology inputs for the central and eastern United States and southeast Canada for the 2023 National Seismic Hazard Model, *Seismol. Res. Lett.* **93,** 3100–3120, doi: 10.1785/0220220162.

Tullis, T. E. (2012). Preface to the focused issue on earthquake simulators, *Seismol. Res. Lett.* **83,** 957–958, doi: 10.1785/0220120122.

Valentini, A., C. B. DuRoss, E. H. Field, R. D. Gold, R. W. Briggs, F. Visini, and B. Pace (2020). Relaxing segmentation on the Wasatch fault zone: Impact on seismic hazard, *Bull. Seismol. Soc. Am.* **110,** 83–109, doi: 10.1785/0120190088.

van der Elst, N. J. (2021). B-Positive: A robust estimator of aftershock magnitude distribution in transiently incomplete catalogs, *J. Geophys. Res.* **126,** e2020JB021027, doi: 10.1029/2020JB021027.

Wang, S., M. J. Werner, and R. Yu (2021). How well does Poissonian probabilistic seismic hazard assessment (PSHA) approximate the simulated hazard of epidemic-type earthquake sequences? *Bull. Seismol. Soc. Am.* **112,** 508–526, doi: 10.1785/0120210022.

Wells, D. L., and K. J. Coppersmith (1994). New empirical relationships among magnitude, rupture length, rupture width, rupture area, and surface displacement, *Bull. Seismol. Soc. Am.* **84,** 974–1002, doi: 10.1785/BSSA0840040974.

Wells, D. L., and B. Youngs (2013). Updated empirical relationships among magnitude, rupture area, rupture length, and surface displacement (abstract), *Seismol. Res. Lett.* **84,** 309.

Wong, I., W. Lund, C. DuRoss, P. Thomas, W. Arabasz, A. Crone, M. Hylland, N. Luco, S. Olig, J. Pechmann, *et al.* (2016). Earthquake probabilities for the Wasatch front region in Utah, Idaho, and Wyoming, *Utah Geol. Surv. Misc. Publ. 16-3*, 164 pp., 5 appendices, available at https://quake.utah.edu/publications/reports/earthquake-probabilities-for-the-wasatch-front-region-in-utah-idaho-and-wyoming (last accessed May 2023).

Working Group on California Earthquake Probabilities (WGCEP) (2003). Earthquake probabilities in the San Francisco Bay region: 2031–2002, *U.S. Geol. Surv. Open-File Rept. 2003-214*.

Youngs, R. R., and K. J. Coppersmith (1985). Implications of fault slip rates and earthquake recurrence models to probabilistic hazard estimates, *Bull. Seismol. Soc. Am.* **75,** 939–964, doi: 10.1785/BSSA0750040939.

Zaliapin, I., and Y. Ben-Zion (2020). Earthquake declustering using the nearest-neighbor approach in space-time-magnitude domain, *J. Geophys. Res.* **125,** e2018JB017120, doi: 10.1029/2018JB017120.

Zechar, J. D., D. Schorlemmer, M. J. Werner, M. C. Gerstenberger, D. A. Rhoades, and T. H. Jordan (2013). Regional earthquake likelihood models I: First-order results, *Bull. Seismol. Soc. Am.* **103,** 787–798.

Zeng, Y. (2022a). GPS velocity field of the western United States for the 2023 National Seismic Hazard Model Update, *Seismol. Res. Lett.* **93,** 3121–3134, doi: 10.1785/0220220180.

Zeng, Y. (2022b). A fault-based crustal deformation model with deep driven dislocation sources for the 2023 update to the U.S. National Seismic Hazard Model, *Seismol. Res. Lett.* **93,** 3170–3185, doi: 10.1785/0220220209.

Zeng, Y., and Z.-K. Shen (2017). A fault-based model for crustal deformation in the western United States based on a combined inversion of GPS and geologic inputs, *Bull. Seismol. Soc. Am.* **107,** 2597–2612, doi: 10.1785/0120150362.

Manuscript received 2 June 2023
Published online 22 December 2023